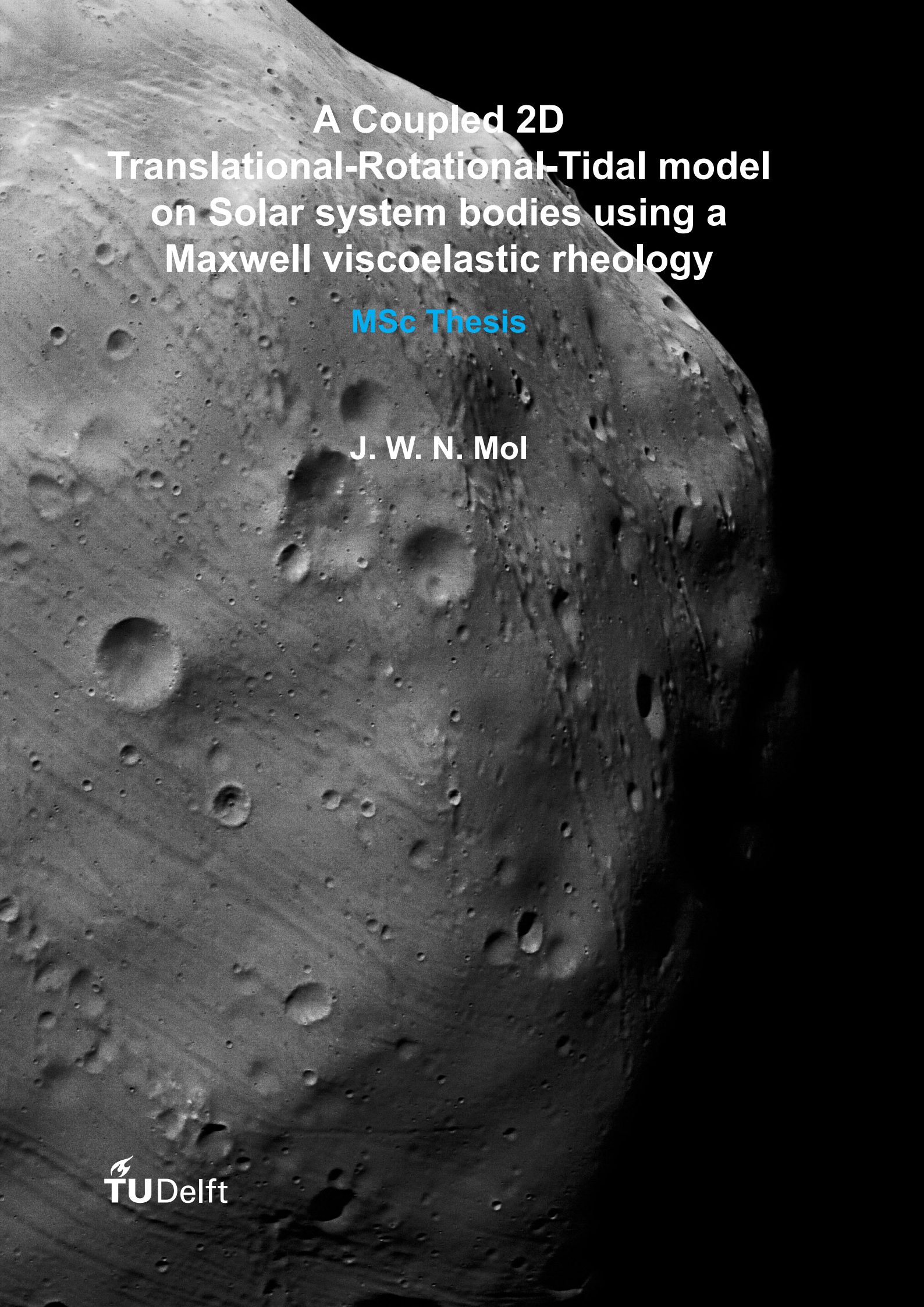

A Coupled 2D Translational-Rotational-Tidal model on Solar system bodies using a Maxwell viscoelastic rheology

MSc Thesis

J. W. N. Mol

TU Delft

A Coupled 2D Translational-Rotational-Tidal model on Solar system bodies using a Maxwell viscoelastic rheology

MSc Thesis

by

J. W. N. Mol

to obtain the degree of Master of Science
at the Delft University of Technology,
to be defended publicly on Monday January 25, 2021 at 10:00 AM.

Student number:	4173708	
Project duration:	December 1, 2019 – January 25, 2021	
Thesis committee:	Prof. dr. L. L. A. Vermeersen,	TU Delft, chair
	Dr. ir. D. Dirkx,	TU Delft, supervisor
	Dr. A. Menicucci,	TU Delft, external

This thesis is confidential and cannot be made public until January 25, 2023.

An electronic version of this thesis is available at `http://repository.tudelft.nl/`.
The cover image is taken by ESA's Mars Express spacecraft and is a photo of Phobos, the moon orbiting Mars.
Image credits: ESA/DLR/FU Berlin

TU Delft Delft University of Technology

Abstract

Planetary observational accuracy increases and the dynamical modeling of tidal behaviour has to follow. In this thesis, a newly developed method (Correia et al. 2014; Boue et al. 2016) to deal with tidal interactions in a 2D two body problem is validated and for the first time applied to Solar system dynamics on a short time-scale. This method uses a Maxwell rheology for the tidally perturbed body, to calculate the instantaneous deformation of the body with a differential equation at the same time as its position, spin vector and orientation. The coupling between the translational, rotational, and tidal dynamics is incorporated in a consistent way, taking into account the frequency dependency of classical tidal parameters. The coupled model is more general and is in contrast to currently used models valid for every eccentricity, spin rate and orientation. The model is applied to the Mars-Phobos and Earth-Moon systems and the tides are determined separately on both the central as the satellite body in various propagations. Several parameters of tidal effects of these systems are obtained and compared with currently available literature approximations and currently used tidal models.

The instantaneous deformation of the tidal body and the evolution of the system's orbit for the tides on the primary compare to the literature approximations and currently used direct tidal force model (Lainey et al. 2007). However, the coupled model displays behaviour of the tidal time lag and angle, which are accompanied with the deformation, that cannot be captured by the classical method. Small differences between final states of the coupled model and the direct tidal force model are obtained that could potentially be important in future space missions and ephemeris determination.

The tides on the locked secondary show a larger difference between the coupled model and the current tidal direct force models (Lainey et al. 2007; Lari 2018) in the case of an existing libration. Phobos has such a libration and huge differences in evolution of the states and orbit are found. The coupled model's evolution values can be partly justified by the theoretical work of Efroimsky (2018) that states the additional dissipation in these bodies with large librations.

Altogether, currently used methods or literature approximations can still be used for inaccurate propagations. However, for more accurate propagations, and for bodies with large physical librations, it rewards to switch to a coupled method. Especially when regarding the tides on the satellite body a coupled model is beneficial.

Preface

So, finally it is finished. It took some years to get to this point, but before you lies the thesis of a soon-to-be-no-longer baby engineer. It is a thesis about tidal stuff, and no, not only those ocean tides. A thesis as part of the Master Aerospace Engineering and track Space Flight. A thesis written during the Corona pandemic of 2020, which means it required some efforts getting finished. Of course I would sincerely like to thank a number of people.

First of all and most sincerely, I would like to thank Dominic. As a supervisor you were there weekly to deal with my work. For over one and a half year you helped me with everything, you endured my stupidity, and guided me towards this final result. Thank you.

Of course I have to thank my fellow students and roommates. Most of them have graduated already, one I could overtake just before the finish line, and one I now see through my liking a bit more often. Thank you very much for all the funny moments, study sessions, and encouraging talks. Those were essential in finally being able to finish this study.

Then I would like to thank my family, my father and sister for always being there for me. Coming home during weekends was never boring and always gave me enough energy to continue the next week again. Thank you for that.

Leaves me to say: enjoy the reading!

J. W. N. Mol
Delft, January 2021

Contents

List of Figures

List of Tables

List of Symbols and Abbreviations

The mathematical notation used in this report is following the International Organization of Standardization (ISO). The international standard ISO 31 uses *italic* notation for all variables, ***bold-italic*** notation for all vector quantities, and roman notation for all units and descriptive terms. The same applies for sub- or superscripts used. A list of used symbols and abbreviations is shown below.

- $\boldsymbol{\nabla}$: The nabla or gradient operator in an inertial frame [-].
- $*$: The convolution product [-].
- $\hat{\boldsymbol{e}}$: A unit vector [-].
- $\boldsymbol{X}^{\mathcal{F}_i}$: The vector $\boldsymbol{X}$ as defined in the frame $\mathcal{F}_i$ [-].

- β: The reduced mass of the system [kg].
- γ: Angle between perturbing position vector and required position vector for the disturbing potential [rad].
- ϵ: The strain or response of a material [-].
- $\delta(t)$: The Dirac-delta function being 0 everywhere except at $t = 0$, where it is ∞ [-].
- $\delta_{(\mathrm{c})}$: The tidal geometric lag angle [rad].
- δ_{ij}: The Kronecker delta function being 0 everywhere except at $i = j$, where it is 1 [-].
- Δt: The time lag of the tidal bulge [s].
- η: Viscosity of material [$\mathrm{kg\,m^{-1}\,s^{-1}}$].
- θ: The colatitude coordinate of a position vector [rad].
- θ_τ: The amplitude of the libration angle [rad].
- μ: The rigidity or stiffness of a material [$\mathrm{N\,m^{-1}}$=$\mathrm{kg\,m\,s^{-2}}$].
- μ_0: The elastic modulus of a spring [$\mathrm{Pa} = \mathrm{kg\,m^{-1}\,s^{-2}}$].
- ν: The angle of the tidal bulge with respect to the rotating x-axis [rad].
- ν_τ: The proper mode [rad].
- ξ: The mean or normalized moment of inertia [-].
- π: The universal constant pi [-].
- ρ: The density of a material [$\mathrm{kg\,m^{-3}}$].
- σ: The stress on a material [$\mathrm{Pa} = \mathrm{kg\,m^{-1}\,s^{-2}}$].
- τ_{e}: The relaxation time of a Maxwell body [s].
- τ_l: A global relaxation time of degree l [s].
- ϕ: The longitude coordinate of a position vector [rad].
- χ: The tidal frequency [$\mathrm{s^{-1}}$].
- ω: Frequency in a Fourier transform function [$\mathrm{s^{-1}}$].
- Ω_0: The spin rate of body 0 [$\mathrm{rad\,s^{-1}}$].
- Ω: The rotation rate [$\mathrm{rad\,s^{-1}}$].
- A: Principal moment in direction of the first axis [$\mathrm{kg\,m^2}$].
- a: Semi-major-axis of an orbit [m].

- B: Principal moment in direction of the second axis [kg m^2].
- C: Principal moment in direction of the third axis [kg m^2].
- $C_{l,m}$: A spherical harmonic coefficient for degree l and order m [m^{l+3} s^{-2}].
- $\Delta C_{l,m}$: Additional spherical harmonic coefficient for degree l and order m due to tides [m^{l+3} s^{-2}].
- $\Delta C^{\nu}_{l,m}$: Different formulation for the additional spherical harmonic coefficient for degree l and order m due to tides [m^{l+3} s^{-2}].
- $\Delta C^{\mathrm{e}}_{l,m}$: Equilibrium additional spherical harmonic coefficient for degree l and order m due to tides [m^{l+3} s^{-2}].
- e: Eccentricity of a orbit [-].
- E: Total energy [J].
- E_{orb}: Orbital energy [J].
- E_{rot}: Rotational energy [J].
- $\boldsymbol{F}$: A force vector [kg m s^{-2}].
- $\boldsymbol{F}_{\mathrm{G}}$: A gravitational force vector [kg m s^{-2}].
- $\mathcal{F}_i$: A reference frame fixed and rotating with body i [-].
- $\mathcal{F}_{\mathrm{I}}$: An inertial reference frame [-].
- $\boldsymbol{F}_{\mathrm{T}}$: The additional force vector due to tidal perturbations [kg m s^{-2}].
- G: The gravitational constant [m^3 kg^{-1} s^{-2}].
- i: The imaginary unit defined as $\mathrm{i}^2 = -1$ [-].
- $\boldsymbol{I}_{(i)}$: The matrix of inertia (of body i) [kg m^2].
- J_l: The degree l zonal harmonic coefficient [m^{l+3} s^{-2}].
- k_l: The static Love number [-].
- k_l^0: The fluid Love number of degree l [-].
- $k_l(t)$: A Love number distribution function dependent on time [-].
- l: The degree of a polynomial expansion [-].
- $\boldsymbol{L}$: The angular momentum vector [kg m^2 s^{-1}].
- $\boldsymbol{L}_{\mathrm{orb}}$: The orbital angular momentum vector [kg m^2 s^{-1}].
- $\boldsymbol{L}_{\mathrm{spin}}$: The spin angular momentum vector [kg m^2 s^{-1}].
- m: The order of a polynomial expansion [-].
- $M_{(i)}$: The mass (of body i) [kg].
- n: The mean motion [rad s^{-1}].
- $\langle P \rangle^{(\mathrm{lib})}_{\mathrm{tide}}$: The power for the additional dissipation due to the tides including the librational dissipation [W].
- $\langle P \rangle^{(\mathrm{main})}_{\mathrm{tide}}$: The power for the dissipation due to the tides excluding the librational dissipation [W].
- P_l: The Legendre polynomial of degree l [-].
- $P_{l,m}$: The associated Legendre polynomial of degree l and order m [-].
- $\boldsymbol{q}$: The quaternion vector [-].
- $\boldsymbol{Q}$: The matrix expressing the change of the quaternion [-].
- Q: The quality factor [-].
- $\boldsymbol{R}$: Position vector of a point on the surface of a body as seen from the center of mass of that body [m].
- R_{E}: The equatorial radius of a body [m].
- $\boldsymbol{r}_{(i)}$: Relative position vector (of body i), i.e. as seen from another body [m].

- $\boldsymbol{R}_i$: Relative position vector of body i, i.e. as seen from another body in a rotating frame [m].
- $\boldsymbol{s}$: The position vector of a mass element inside a body [m].
- $S_{l,m}$: A spherical harmonic coefficient for degree l and order m [$\mathrm{m}^{l+3}\,\mathrm{s}^{-2}$].
- $\Delta S_{l,m}$: Additional spherical harmonic coefficient for degree l and order m due to tides [$\mathrm{m}^{l+3}\,\mathrm{s}^{-2}$].
- $\Delta S^{\nu}_{l,m}$: Different formulation for the additional spherical harmonic coefficient for degree l and order m due to tides [$\mathrm{m}^{l+3}\,\mathrm{s}^{-2}$].
- $\Delta S^{\mathrm{e}}_{l,m}$: Equilibrium additional spherical harmonic coefficient for degree l and order m due to tides [$\mathrm{m}^{l+3}\,\mathrm{s}^{-2}$].
- t: The time variable [s].
- $\boldsymbol{v}$: The velocity vector [$\mathrm{m\,s}^{-1}$].
- $V_{(i)}$: The gravitational potential function (for body i) [$\mathrm{J\,kg}^{-1} = \mathrm{m}^2\,\mathrm{s}^{-2}$].
- V_{T}: The additional gravitational potential function due to tidal perturbations [$\mathrm{J\,kg}^{-1} = \mathrm{m}^2\,\mathrm{s}^{-2}$].
- $V^{\mathrm{e}}_{\mathrm{T},l}$: Equilibrium additional gravitational potential function of degree l due to tidal perturbations [$\mathrm{J\,kg}^{-1} = \mathrm{m}^2\,\mathrm{s}^{-2}$].
- $W_{(l)}$: The perturbing or tide-generating potential function (of degree l) [$\mathrm{J\,kg}^{-1} = \mathrm{m}^2\,\mathrm{s}^{-2}$].
- $\Delta Z_{l,m}$: Additional spherical harmonic coefficient for degree l and order m due to tides [$\mathrm{m}^{l+3}\,\mathrm{s}^{-2}$].
- $\Delta Z^{\nu}_{l,m}$: Different formulation for the additional spherical harmonic coefficient for degree l and order m due to tides [$\mathrm{m}^{l+3}\,\mathrm{s}^{-2}$].
- $\Delta Z^{\mathrm{e}}_{l,m}$: Equilibrium additional spherical harmonic coefficient for degree l and order m due to tides [$\mathrm{m}^{l+3}\,\mathrm{s}^{-2}$].

- EOM: Equations of motion.
- INPOP: Numerical integrator of the Paris Observatory
- JPL: Jet Propulsion Laboratory.
- JUICE: Jupiter Icy Moons Explorer.
- NASA: National Aeronautics and Space Administration.

1 Introduction

Studying the celestial sky and determining the orbits of the solar system objects has been performed for ages: from the first positions of the moons of Jupiter found by Galileo presented in his *Sidereus Nuncius* in 1610 (Galilei and Van Helden 1989), the discovery of elliptical orbits by Kepler described in his *Astronomia Nova* around the same time (Lissauer 2009), and the fundamental laws of motion in the *Principia* by Newton in 1687 (Newton et al. 1729), to the current days and more accurate ephemerides (*e.g.* JPL Development Ephemerides, Folkner et al. 2014 and INPOP, Viswanathan et al. 2017).

An ephemeris, or plural ephemerides, can nowadays be described as a tool of finding the position of celestial bodies at a desired time, even for the future. This is possible because the dynamical modelling has developed enough to propagate orbits ahead into time. A dynamical model is an incorporation of the laws of nature that govern the motion of objects and returns a prediction for the future motion of the objects through an analytical solution or numerical integration. The modelling is still based on some sort of observations. The ephemeris has been made by fitting the observations in some way to the dynamical model, and uses the dynamical model to find new positions at different epochs (Folkner et al. 2014). Whenever the observations acquired become more accurate, the dynamical model should give more accurate estimates as well. Only when the observations become so accurate, that their accuracy surpasses the accuracy of the dynamical model, steps need to be taken: The dynamical model should be updated to include additional physical perturbations that are now large enough to be reckoned with.

For specific solar system dynamics the accuracy of the observations improves to below model standards, as multiple tracking-data types emerge for new missions. As discussed in Dirkx et al. (2019), new methods such as multi-wavelength radiometric range and Doppler measurements (Dehant et al. 2017), same-beam interferometry (Kikuchi et al. 2009), and interplanetary laser ranging (Turyshev et al. 2010) could achieve new standards of accuracy. This requires the current dynamical models to be evolved to an accuracy at least equal to, but ideally well below the accuracy of the observations. If done properly, new and more accurate estimates of properties of the system's bodies can be retrieved, indirectly giving information about the bodies' evolution, and moreover about the formation and evolution of planetary systems in general (Dirkx et al. 2016). An example is Lainey et al. (2020), where suggestions are given on Titan's origin based on a reanalysis of accurate observations.

The improved models should include a realistic approach for frequency-dependent tidal dissipation, a detailed non-conservative force model for small interacting bodies, and figure-figure gravitational interactions (Dirkx et al. 2019), where the last takes into account the full mass distribution of the concerning system. These steps were already taken by Efroimsky (2012), where the frequency dependence of tidal dissipation is discussed in depth, or by numerous authors setting up a figure-figure gravitational interactive model (*e.g.* Borderies 1978; Maciejewski 1995; Ashenberg 2005; Fahnestock and Scheeres 2006; Boue et al. 2016; Dirkx et al. 2019). Aforementioned methods are tested and used for specific solar system dynamics.

The tidal dynamics are as well such a dynamical model that can be improved. The tidal effects have

been studied for ages, and the modelling of tidal dissipation and accompanied effects is described in multiple articles. Already in 1754, Immanual Kant introduced the effects of tidal dissipation by stating that the Earth's rotation would slowly decrease until it would equal the orbital period of the Moon, in fact until Earth days would equal Lunar months (Kant 1754). This suggestion was confirmed by Darwin and Glaisher (1879), Darwin being a son of famous naturalist Charles Darwin. They started modelling the dissipation and used a Fourier expansion for the tidal potential (Darwin 1880). Kaula (1964) then extended this into a general formulation with possible frequency dependence of the tidal lag, which is still being used today (Efroimsky and Williams 2009). This tidal lag modelling is key to understanding the tidal behaviour. The tidal lag can be described as the phase lag between the position of the tidal origin (*i.e.* the perturbing body), and the tidal bulge (*i.e.* the location where the tides are high). Due to the lag, the tides are not aligned with the direction of the perturbing body. It takes time for the body to deform due to the internal dissipation.

To model the tidal lag, others have tried different, less complicated approaches. Macdonald (1964) and Goldreich and Soter (1966) developed and used the constant geometric lag model (*i.e.* keeping the angle between the direction of the perturbing body and the position of the tidal bulge a constant). More recently, this was rejected by Efroimsky and Makarov (2013), stating that the model is contradictory. Singer (1968) and Mignard (1980) then developed the constant time lag model, stating that the tidal bulge position at time t is caused by the perturbing body at time $t - \Delta t$, while at the same time including the frequency dependence of the tidal lag (Boue et al. 2016). Mignard (1980) used a very compact way to describe the tidal force and torque by linearizing the potential function. In fact, the model is still used to incorporate tidal dissipation in current day planetary satellite ephemeris, because of its compact formulation (Lainey et al. 2007, 2009; Lari 2018). More recently, Ferraz-Mello (2013) developed a tidal creep theory, where a different approach is taken. The body tends to 'creep' to its equilibrium position aligned with the perturbing body and the stress applied to the tidal bulge is assumed to be proportional to the distance from equilibrium.

The current dynamical models consist of a translational, a possible rotational and of a possible tidal part. In reality these parts are completely intertwined, depend and act on each other, but are usually not completely coupled in the model. For example in Lainey et al. (2004, 2007), where the ephemerides of both the Jovian and Martian system are determined, the model integrates only the translational part. The rotation is modelled a priori with an analytical solution, and the tides are included as an additional effect to the translational part. In for example Dirkx et al. (2019) the dynamical model includes the integration and coupling of the translational and rotational part, but lacks the effect of the tides. Note however, that their approach is fully warranted by the accuracy of the available data.

All this considered, the tidal lag and thus tidal effect are completely determined by the rheology of the body (*i.e.* the model for the flow of matter of the body). The constant time lag model can be regarded as a first order viscoelastic rheological model. However, when a completely coupled model is implemented, the rheological model determines the deformation of the body at every time step of the numerical propagation through a differential equation, at the same time as the position, velocity and angular momentum are determined.

Correia et al. (2014) tried this approach for two exoplanets, and Boue et al. (2016) extended this with a complex description and a more general formulation for dynamics of similar extrasolar planets. The approach from Boue et al. (2016) is very general and applicable to any kind of orbital configuration, while the earlier Fourier expansion (Darwin 1880) always used the fact that the eccentricity should be small to truncate at a low level. The classical way from Lainey et al. (2007) would be to add a force due to the tidal effect, while a coupled system calculates the mass deformation of the body on the basis of a rheological model at the same time step and then simply includes this additional gravitational effect. It would not be such a problem whenever this tidal effect can be determined very accurately. However, in particular for tides on satellite bodies the tidal effects are not easily determined (Efroimsky 2012).

The full coupled model in recent literature was only tested for dynamical systems outside the solar system and for long-term evolution (*e.g.* Correia et al. 2014 and Boue et al. 2016). The important short-term evolution (*i.e.* days to years) for planetary missions is not discussed.

The research performed in this thesis extends this work and applies this coupled modelling closer to home. The goal of this study is to develop a 2-dimensional coupled model for specific solar system dynamics and to test it by comparing it with current other models. This research investigates whether coupled modelling could be beneficial for short-term ephemeris determination and thus for data analysis of future planetary missions. The relatively simple rheological Maxwell model (Renaud and Henning 2018) is used to model the body's deformation.

Two systems are considered in this research (*i.e.* the Mars-Phobos and the Earth-Moon case), where the Mars-Phobos system is the most interesting of the two. Phobos is the closest moon of Mars and is slowly spiralling inward. It experiences a large tidal force due to its close distance and has a large libration due to its high gravitational triaxiality. Together with the fact that it has a slight eccentric orbit and induced libration it could mean that a coupled system is beneficial for its propagation accuracy. The Earth-Moon system is chosen because it is the best known planet-moon system and thus is more easily validated with literature and earlier observations.

This leads to the following main research question:

What is the benefit of using a fully coupled translational-rotational-tidal model, when comparing with currently used other models and literature approximations, and for what systems could this be beneficial?

Two lower-level research questions and accompanied sub-questions should explain the top-level one and are:

1. What is the benefit of using a fully coupled model, when comparing with currently used other models and literature approximations, for a 2D system with tides on the primary?

   The orbital elements regarded include the semi-major axis and eccentricity. Due to the tidal torque and lag these parameters will see a change. Literature approximations are available to determine these changes up front, and these approximations can be compared with the evolution of the systems as propagated in the coupled model, but also with the evolution as propagated while using the current direct tidal force models. The tides on the primary are a good benchmark case for the later and more difficult to determine tides on the secondary part. The following sub-questions are asked:

   - What is the behaviour of the coupled model for the test-cases Mars-Phobos and Earth-Moon, when regarding the evolution of the tidal geopotential coefficients, accompanied tidal lag angle and time lag?
   - What is the behaviour of the coupled model for the test-cases Mars-Phobos and Earth-Moon, when regarding the evolution of the orbital elements?

2. What is the benefit of using a fully coupled model, when comparing with currently used other models and literature approximations, for a 2D system with tides on the locked secondary?

   The tides on the secondary are usually much harder to determine. Both test-cases have an eccentricity, thus the satellite bodies will have librational as well as radial tides. Their combination and dissipation is difficult to determine and up to this date there are arguments about the correct literature approximations for the semi-major axis evolution. This leads to the following sub-questions:

- What is the behaviour of the coupled model for the test-cases Phobos-Mars and Moon-Earth, when regarding the evolution of the tidal geopotential coefficients?

- What is the behaviour of the coupled model for the test-cases Phobos-Mars and Moon-Earth, when regarding the evolution of the orbital elements and librations?

After this introduction, a stand-alone paper will describe the main research performed. The description of the coupled model as well as methods for validation of this model are included. It discusses the results of the test-cases and draws a conclusion on whether the coupled model can be beneficial, and in what cases. After the paper, the findings are concluded in the report as well, with specific answers to the aforementioned research questions. The recommendations include a short discussion on what possible further research could be done. Appendices are included which state additional derivations, a documentation of the Python code used, and a verification of the Python modelling.

2

Paper

The following stand-alone paper contains the main research performed.

A coupled 2D translational-rotational-tidal model on Solar system bodies using a Maxwell viscoelastic rheology

J. W. N. Mol[a,]

[a] *Delft University of Technology, Kluyverweg 1, 2629HS Delft, The Netherlands*

Abstract

Planetary observational accuracy increases and the dynamical modeling of tidal behaviour has to follow. In this paper, a newly developed method (Correia et al. 2014; Boue et al. 2016) to deal with tidal interactions in a 2D two body problem is validated and for the first time applied to Solar system dynamics on a short time-scale. This method uses a Maxwell rheology for the tidally perturbed body, to calculate the instantaneous deformation of the body with a differential equation at the same time as its position, spin vector and orientation. The coupling between the translational, rotational, and tidal dynamics is incorporated in a consistent way, taking into account the frequency dependency of classical tidal parameters. The coupled model is more general and is in contrast to currently used models valid for every eccentricity, spin rate and orientation. The model is applied to the Mars-Phobos and Earth-Moon systems and the tides are determined separately on both the central as the satellite body in various propagations. Several parameters of tidal effects of these systems are obtained and compared with currently available literature approximations and currently used tidal models.

The instantaneous deformation of the tidal body and the evolution of the system's orbit for the tides on the primary compare to the literature approximations and currently used direct tidal force model (Lainey et al. 2007). However, the coupled model displays behaviour of the tidal time lag and angle, which are accompanied with the deformation, that cannot be captured by the classical method. Small differences between final states of the coupled model and the direct tidal force model are obtained that could potentially be important in future space missions and ephemeris determination.

The tides on the locked secondary show a larger difference between the coupled model and the current tidal direct force models (Lainey et al. 2007; Lari 2018) in the case of an existing libration. Phobos has such a libration and huge differences in evolution of the states and orbit are found. The coupled model's evolution values can be partly justified by the theoretical work of Efroimsky (2018) that states the additional dissipation in these bodies with large librations.

Altogether, currently used methods or literature approximations can still be used for inaccurate propagations. However, for more accurate propagations, and for bodies with large physical librations, it rewards to switch to a coupled method. Especially when regarding the tides on the satellite body a coupled model is beneficial.

Keywords: Tidal dynamics; Maxwell model; Tidal evolution; Libration;

1. Introduction

Studying the celestial sky and determining the orbits of the solar system objects has been performed for ages: from the first positions of the moons of Jupiter found by Galileo presented in his *Sidereus Nuncius* in 1610 (Galilei and Van Helden 1989), the discovery of elliptical orbits by Kepler described in his *Astronomia Nova* around the same time (Lissauer 2009), and the fundamental laws of motion in the *Principia* by Newton in 1687 (Newton et al. 1729), to the current days and more accurate ephemerides (*e.g.* JPL Development Ephemerides, Folkner et al. 2014 and INPOP, Viswanathan et al. 2017).

The accuracy of the observations has increased over the centuries. When the observations become so accurate, that their accuracy surpasses the accuracy of the dynamical model (*i.e.* the physical model of how to predict and calculate the orbits), the dynamical model should be updated to include additional physical effects that are now large enough to be reckoned with.

For specific solar system dynamics the accuracy of the observations improves to below model standards, as multiple tracking-data types emerge for new missions. As discussed in Dirkx et al. (2019), new methods such as multi-wavelength radiometric range and Doppler measurements (Dehant et al. 2017), same-beam interferometry (Kikuchi et al. 2009), and interplanetary laser ranging (Turyshev et al. 2010) could achieve new standards of accuracy. This requires the current dynamical models to be evolved to an accuracy at least equal to, but ideally well below the accuracy of the observations. If done properly, new and more accurate estimates of properties of the system's bod-

Email address: jwn.mol@gmail.com (J. W. N. Mol)

ies can be retrieved, indirectly giving information about the bodies' evolution, and moreover about the formation and evolution of planetary systems in general (Dirkx et al. 2016). An example is Lainey et al. (2020), where suggestions are given on Titan's origin based on a reanalysis of accurate observations.

The improved models should include a realistic approach for frequency-dependent tidal dissipation, a detailed non-conservative force model for small interacting bodies, and figure-figure gravitational interactions (Dirkx et al. 2019), where the last takes into account the full mass distribution of the concerning system. These steps were already taken by Efroimsky (2012), where the frequency dependence of tidal dissipation is discussed in depth, or by numerous authors setting up a figure-figure gravitational interactive model (*e.g.* Borderies 1978; Maciejewski 1995; Ashenberg 2005; Fahnestock and Scheeres 2006; Boue et al. 2016; Dirkx et al. 2019). Aforementioned methods are tested and used for specific solar system dynamics.

The tidal dynamics are as well such a dynamical model that can be improved. The tidal effects have been studied for ages, and the modelling of tidal dissipation and accompanied effects is described in multiple articles. Already in 1754, Immanual Kant introduced the effects of tidal dissipation by stating that the Earth's rotation would slowly decrease until it would equal the orbital period of the Moon, in fact until Earth days would equal Lunar months (Kant 1754). This suggestion was confirmed by Darwin and Glaisher (1879), Darwin being a son of famous naturalist Charles Darwin. They started modelling the dissipation and used a Fourier expansion for the tidal potential (Darwin 1880). Kaula (1964) then extended this into a general formulation with possible frequency dependence of the tidal lag, which is still being used today (Efroimsky and Williams 2009). This tidal lag modelling is key to understanding the tidal behaviour. The tidal lag can be described as the phase lag between the position of the tidal origin (*i.e.* the perturbing body), and the tidal bulge (*i.e.* the location where the tides are high). Due to the lag, the tides are not aligned with the direction of the perturbing body. It takes time for the body to deform due to the internal dissipation.

To model the tidal lag, others have tried different, less complicated approaches. Macdonald (1964) and Goldreich and Soter (1966) developed and used the constant geometric lag model (*i.e.* keeping the angle between the direction of the perturbing body and the position of the tidal bulge a constant). More recently, this was rejected by Efroimsky and Makarov (2013), stating that the model is contradictory. Singer (1968) and Mignard (1980) then developed the constant time lag model, stating that the tidal bulge position at time t is caused by the perturbing body at time $t - \Delta t$, while at the same time including the frequency dependence of the tidal lag (Boue et al. 2016). Mignard (1980) used a very compact way to describe the tidal force and torque by linearizing the potential function. In fact, the model is still used to incorporate tidal dissipation in current day planetary satellite ephemeris, because of its compact formulation (Lainey et al. 2007, 2009; Lari 2018). More recently, Ferraz-Mello (2013) developed a tidal creep theory, where a different approach is taken. The body tends to 'creep' to its equilibrium position aligned with the perturbing body and the stress applied to the tidal bulge is assumed to be proportional to the distance from equilibrium.

The current dynamical models consist of a translational, a possible rotational and of a possible tidal part. In reality these parts are completely intertwined, depend and act on each other, but are usually not completely coupled in the model. For example in Lainey et al. (2004, 2007), where the ephemerides of both the Jovian and Martian system are determined, the model integrates only the translational part. The rotation is modelled a priori with an analytical solution, and the tides are included as an additional effect to the translational part. In for example Dirkx et al. (2019) the dynamical model includes the integration and coupling of the translational and rotational part, but lacks the effect of the tides. Note however, that their approach is fully warranted by the accuracy of the available data.

All this considered, the tidal lag and thus tidal effect are completely determined by the rheology of the body (*i.e.* the model for the flow of matter of the body). The constant time lag model can be regarded as a first order viscoelastic rheological model. However, when a completely coupled model is implemented, the rheological model determines the deformation of the body at every time step of the numerical propagation through a differential equation, at the same time as the position, velocity and angular momentum are determined.

Correia et al. (2014) tried this approach for two exoplanets, and Boue et al. (2016) extended this with a complex description and a more general formulation for dynamics of similar extrasolar planets. The approach from Boue et al. (2016) is very general and applicable to any kind of orbital configuration, while the earlier Fourier expansion (Darwin 1880) always used the fact that the eccentricity should be small to truncate at a low level. The classical way from Lainey et al. (2007) would be to add a force due to the tidal effect, while a coupled system calculates the mass deformation of the body on the basis of a rheological model at the same time step and then simply includes this additional gravitational effect. It would not be such a problem whenever this tidal effect can be determined very accurately. However, in particular for tides on satellite bodies the tidal effects are not easily determined (Efroimsky 2012).

The full coupled model in recent literature was only tested for dynamical systems outside the solar system and for long-term evolution (*e.g.* Correia et al. 2014 and Boue et al. 2016). The important short-term evolution (*i.e.* days to years) for planetary missions is not discussed.

The research performed in this paper extends this work and applies this coupled modelling closer to home. The

goal of this study is to develop a 2-dimensional coupled model for specific solar system dynamics and to test it by comparing it with current other models. This research investigates whether coupled modelling could be beneficial for short-term ephemeris determination and thus for data analysis of future planetary missions. The relatively simple rheological Maxwell model (Renaud and Henning 2018) is used to model the body's deformation.

Two systems are considered in this research (*i.e.* the Mars-Phobos and the Earth-Moon case), where the Mars-Phobos system is the most interesting of the two. Phobos is the closest moon of Mars and is slowly spiralling inward. It experiences a large tidal force due to its close distance and has a large libration due to its high gravitational triaxiality. Together with the fact that it has a slight eccentric orbit and induced libration it could mean that a coupled system is beneficial for its propagation accuracy. The Earth-Moon system is chosen because it is the best known planet-moon system and thus is more easily validated with literature and earlier observations.

After this introduction, the 2-dimensional two-body problem used for this research is described in Section 2. In Section 3, the currently used tidal evolution models are described, for both the tides on the central and on the satellite body. The coupled model is covered in Section 4, describing the full equations of motion for the translational, rotational, and tidal dynamics. Section 5 discusses the methods for validation, comparison, and analysis of the tidal behaviour of the coupled model, and the currently used tidal models. Subsequently, the test-cases will be introduced and results will be shown of the coupled model's behaviour with tides on the central body in Section 6, and tides on the satellite body in Section 7.

2. Extended Two Body Problem

An extended two body problem is considered with a central extended body of mass M_c, and a point mass satellite/secondary body of mass M_s. The central body has a second degree and order gravity field, expressed in the spherical harmonic coefficients J_2, $C_{2,2}$, and $S_{2,2}$. The rotation vector of the central body is aligned with $\hat{\boldsymbol{e}}_C$ from the fixed rotating reference frame $\mathcal{F}_\mathrm{C} = (\hat{\boldsymbol{e}}_A, \hat{\boldsymbol{e}}_B, \hat{\boldsymbol{e}}_C)$, and is also orthogonal to the orbital plane, which thus creates a 2-dimensional problem. The situation is sketched in Figure 1, and is discussed in Correia et al. (2014). The ellipse is added to show that the tidal behaviour on the central body will be of importance.

2.1. The potential function

The gravitational potential of a body is described as

$$V(\boldsymbol{r}) = -\int_\mathrm{C} \frac{G\mathrm{d}M}{|\boldsymbol{r}-\boldsymbol{s}|}\,, \tag{1}$$

where the integral is taken over all mass elements in body C, $\boldsymbol{s}$ is the position vector of the mass element inside the body and $\boldsymbol{r}$ the position vector of the evaluated point outside the body. Conventionally, the integral is expressed in spherical harmonics (*e.g.* Lambeck 1988; Dirkx et al. 2019), which leads to

$$\begin{aligned} V(\boldsymbol{r}) = &-\frac{GM}{R_\mathrm{E}}\sum_{l=0}^{\infty}\left(\frac{R_\mathrm{E}}{|\boldsymbol{r}|}\right)^{l+1} \\ &\times\sum_{m=0}^{l}\left(C_{l,m}\cos(m\phi)+S_{l,m}\sin(m\phi)\right)P_{l,m}(\cos\vartheta)\,. \end{aligned} \tag{2}$$

If reduced to second degree (*i.e.* $l = 2$) the potential for this 2-dimensional situation (sketched in Figure 1) can be described as (*e.g.* Correia and Rodríguez 2013; Correia et al. 2014),

$$\begin{aligned} V(\boldsymbol{r}) = &-\frac{GM_\mathrm{c}}{|\boldsymbol{r}|}-\frac{GM_\mathrm{c}{R_\mathrm{E}}^2 J_2}{2|\boldsymbol{r}|^3} \\ &-\frac{3GM_\mathrm{c}{R_\mathrm{E}}^2}{|\boldsymbol{r}|^3}\left(C_{2,2}\cos 2\gamma - S_{2,2}\sin 2\gamma\right)\,, \end{aligned} \tag{3}$$

where G is the gravitational constant, R_E the equatorial radius of body C used as reference radius, l and m the degree and order of the spherical harmonic, ϕ and ϑ the longitude and colatitude of the position vector $\boldsymbol{r}$ in the rotating frame, and $P_{l,m}$ the unnormalized associated Legendre polynomial (*e.g.* Montenbruck and Gill 2000, Boue et al. 2016). The angle γ denotes the negative of the longitude of the position vector as used in Correia et al. (2014). The periodic functions are then calculated via

$$\begin{aligned} \cos 2\gamma &= \left(\hat{\boldsymbol{e}}_\mathrm{A}\cdot\hat{\boldsymbol{r}}\right)^2-\left(\hat{\boldsymbol{e}}_\mathrm{B}\cdot\hat{\boldsymbol{r}}\right)^2\,, \\ \sin 2\gamma &= -2(\hat{\boldsymbol{e}}_\mathrm{A}\cdot\hat{\boldsymbol{r}})(\hat{\boldsymbol{e}}_\mathrm{B}\cdot\hat{\boldsymbol{r}})\,. \end{aligned} \tag{4}$$

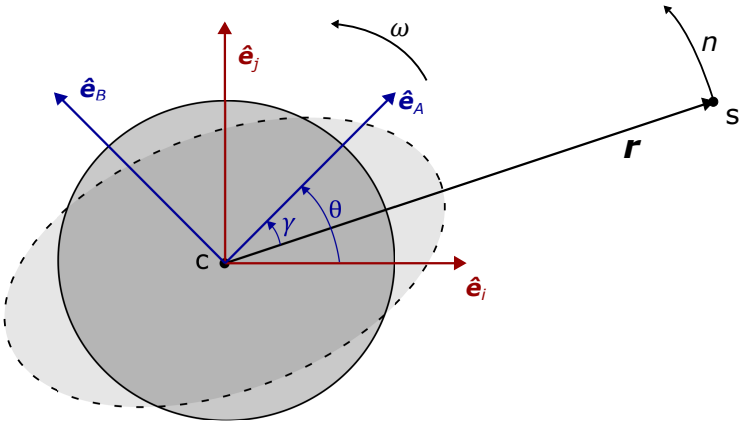

Figure 1: Overview of the extended two body problem of a central body C and satellite body S shown in a 2-dimensional manner. The inertial reference frame $\mathcal{F}_\mathrm{I} = (\hat{\boldsymbol{e}}_i, \hat{\boldsymbol{e}}_j, \hat{\boldsymbol{e}}_k)$ is centered in the central body, and the rotating frame $\mathcal{F}_\mathrm{C} = (\hat{\boldsymbol{e}}_A, \hat{\boldsymbol{e}}_B, \hat{\boldsymbol{e}}_C)$ is fixed with the central body. Note that $\hat{\boldsymbol{e}}_k$ and $\hat{\boldsymbol{e}}_C$ are the same and out-of-plane towards the reader. $\boldsymbol{r}$ is the position vector from body C to S, ω is the rotation velocity of body C and n is the orbital mean motion of body S. γ is the angular direction of the satellite body S as seen from the rotating frame $\mathcal{F}_\mathrm{C}$, and θ is the rotation angle between both frames.

2.2. Equations of motion

The translational evolution of the system is calculated according to Newton's second law,

$$\frac{\mathrm{d}^2\boldsymbol{r}}{\mathrm{d}t^2} = \boldsymbol{F}/\beta\,, \tag{5}$$

with $\beta = M_\mathrm{c}M_\mathrm{s}/(M_\mathrm{c}+M_\mathrm{s})$ the reduced mass of the system and where the force is given by the gradient of the potential function (Equation 6),

$$\boldsymbol{F} = -\boldsymbol{\nabla}V(\boldsymbol{r})\,. \tag{6}$$

The rotation of the central body is expressed in the rotation velocity vector $\boldsymbol{\omega}$, the evolution of which is governed by the conservation of the angular momentum, as

$$\frac{\mathrm{d}\boldsymbol{L}}{\mathrm{d}t} = \boldsymbol{I}\frac{\mathrm{d}\boldsymbol{\omega}}{\mathrm{d}t} + \boldsymbol{\omega}\frac{\mathrm{d}\boldsymbol{I}}{\mathrm{d}t} = -\boldsymbol{r}\times\boldsymbol{F}\,. \tag{7}$$

Here, $\boldsymbol{L}$ is the spin angular momentum and $\boldsymbol{I}$ the matrix of inertia. This matrix is usually constant for planetary bodies because the gravitational deformations and changes in the moments of inertia are small (but exceptions exist, see Section 7) and the evolution of the rotation simplifies to the last term in Equation 8,

$$\frac{\mathrm{d}\boldsymbol{\omega}}{\mathrm{d}t} = -\boldsymbol{I}^{-1}\left(\boldsymbol{\omega}\frac{\mathrm{d}\boldsymbol{I}}{\mathrm{d}t} + \boldsymbol{r}\times\boldsymbol{F}\right) \approx -\boldsymbol{I}^{-1}(\boldsymbol{r}\times\boldsymbol{F})\,. \tag{8}$$

For the 2-dimensional case described in Figure 1, the translational part can be expanded as

$$\begin{aligned}\frac{\mathrm{d}^2\boldsymbol{r}}{\mathrm{d}t^2} = &-\frac{G(M_\mathrm{s}+M_\mathrm{c})}{|\boldsymbol{r}|^3}\boldsymbol{r} - \frac{3G(M_\mathrm{s}+M_\mathrm{c}){R_\mathrm{E}}^2}{2|\boldsymbol{r}|^5}J_2\boldsymbol{r}\\ &+\frac{9G(M_\mathrm{s}+M_\mathrm{c}){R_\mathrm{E}}^2}{|\boldsymbol{r}|^5}\big(C_{2,2}\cos 2\gamma - S_{2,2}\sin 2\gamma\big)\boldsymbol{r}\\ &+\frac{6G(M_\mathrm{s}+M_\mathrm{c}){R_\mathrm{E}}^2}{|\boldsymbol{r}|^4}\big(C_{2,2}\cos 2\gamma + S_{2,2}\sin 2\gamma\big)(\hat{\boldsymbol{e}}_\mathrm{C}\times\boldsymbol{r})\,.\end{aligned} \tag{9}$$

The equations for the rotation are similarly derived in Equation 10,

$$\frac{\mathrm{d}\boldsymbol{\omega}}{\mathrm{d}t} = -\frac{6GM_\mathrm{s}M_\mathrm{c}{R_\mathrm{E}}^2}{C|\boldsymbol{r}|^3}\big(C_{2,2}\cos 2\gamma + S_{2,2}\sin 2\gamma\big)\hat{\boldsymbol{e}}_\mathrm{C}\,, \tag{10}$$

where $C = (2/3J_2 + \xi)\,M_\mathrm{c}{R_\mathrm{E}}^2$ denotes the principal moment of inertia, which is the moment along the principal $\hat{\boldsymbol{e}}_C$ axis. ξ is the mean normalized moment of inertia of the central body.

Because of the possible irregular shape of the central body an orientation of the body has to be recorded during a numerical propagation as well. Multiple methods are available, but the quaternion representation with the quaternion vector $\boldsymbol{q} = (q_0,\, q_1,\, q_2,\, q_3)$ as described by Fukushima (2008) is selected here because it has no singularities, while the Euler angles representation has these possible singularities at the poles. Note that for the 2-dimensional case as in Figure 1, a simplified equation for the rotation angle θ can also be used. To keep the model able to cope with more elaborate situations than this 2-dimensional model, the evolution of the quaternion vector is still calculated (see Equation 11),

$$\begin{aligned}\frac{\mathrm{d}\boldsymbol{q}}{\mathrm{d}t} &= \boldsymbol{Q}(\boldsymbol{q})\boldsymbol{\omega}\,,\\ \boldsymbol{Q}(\boldsymbol{q}) &= \frac{1}{2}\begin{pmatrix}-q_1 & -q_2 & -q_3\\ q_0 & -q_3 & q_2\\ q_3 & q_0 & -q_1\\ -q_2 & q_1 & q_0\end{pmatrix}.\end{aligned} \tag{11}$$

The quaternion vector then relates to the unit axis of the rotating frame $\mathcal{F}_\mathrm{C}$ at every instant (see Appendix A and Fukushima 2008). This completes the base set up of the model, including the evolution of the orbital and spin motion of the system.

3. Tidal Effects

The tides, their behaviour, and effects on the translation and rotation of the system are key in this research. This section discusses the tidal origin and effects, as are used today, to validate the results from the coupled model later in Section 4.

3.1. Perturbing potential

The tides on a body are the time dependent deformations of that body due to a spatial difference in forcing. Figure 2 shows an exaggerated sketch of the tide-generating force field. This force field is the cause of the tidal deformations, it creates a tidal bulge directed towards the perturbing body, with also a high tide on the back of the body. In potential form this perturbing force is commonly denoted as (Efroimsky and Williams 2009),

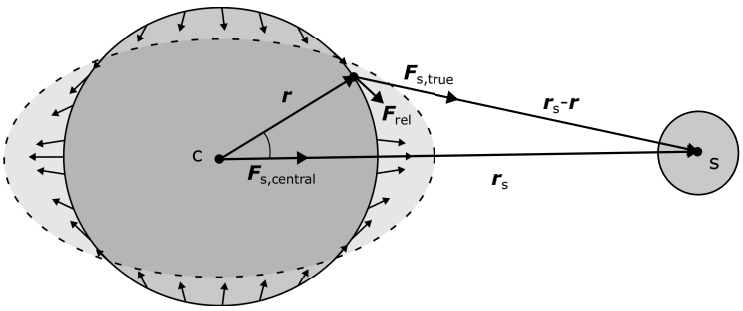

Figure 2: Exaggerated tide-generating force field and origin of the tidal deformation. The force experienced at the surface point $\boldsymbol{r}$ is different from the one experienced at the center of mass of body C caused by the tide-generating body S. It generates an apparent force $\boldsymbol{F}_\mathrm{rel}$ in the direction of the line connecting the two centers of mass.

$$W = -\frac{GM_\mathrm{s}}{|\boldsymbol{r}_\mathrm{s}-\boldsymbol{r}|} + \frac{GM_\mathrm{s}}{|\boldsymbol{r}_\mathrm{s}|^3}(\boldsymbol{r}_\mathrm{s}\cdot\boldsymbol{r})\,, \tag{12}$$

or written in expanded form at a surface point $\boldsymbol{R}$ as

$$W(\boldsymbol{R}, \boldsymbol{r}_\mathrm{s}) = -\frac{GM_\mathrm{s}}{|\boldsymbol{R}|} \sum_{l=2}^{\infty} \left(\frac{|\boldsymbol{R}|}{|\boldsymbol{r}_\mathrm{s}|} \right)^{l+1} P_l(\cos\gamma) \,. \tag{13}$$

Here, $\boldsymbol{R}$ denotes the position vector to the surface point and γ the angular separation between $\boldsymbol{R}$ and $\boldsymbol{r}_\mathrm{s}$. P_l denotes the Legendre Polynomial of degree l (Montenbruck and Gill 2000).

3.2. Tidal lag

The response of the body to the perturbing potential is the actual tidal deformation. This deformation causes a tidal potential in addition to the original static gravitational potential of the perturbed body. The response and deformation is generally not instantaneous, as the body has a viscosity. And because the two body system is often not fully evolved into a state where both orbital and spin rotation are the same, the difference in orbital and spin rate in the system ensures that the tidal bulge as depicted in Figure 2 is not directly aligned along the connecting position vector. A sketch of an exaggerated tidal lag is shown in Figure 3. The tidal geometric lag angle denoted

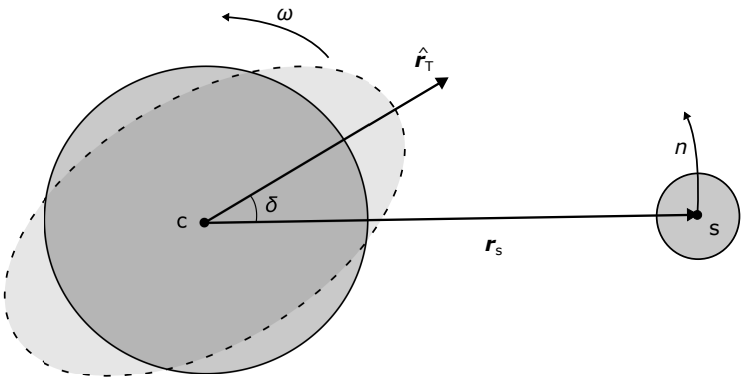

Figure 3: Exaggerated tidal lag of the tidal bulge in a system where the central body's spin rate ω is larger than the orbital rate of the satellite n. δ here is the tidal geometric lag angle and $\hat{\boldsymbol{r}}_\mathrm{T}$ the direction of the tidal bulge.

with δ causes an additional torque on the satellite, in its turn slowing the planet's rotation and raising the orbit of the satellite to a higher semi-major axis. The description of this phase lag or tidal lag is thus key in describing the deformation and tidal potential (Efroimsky and Lainey 2007) and has a major impact on the long term evolution of the system. Without stating anything about the response of the material of the body, only assuming a linear and isotropic tidal behaviour (*i.e.* the deformation magnitude depends linearly on the tidal perturbation and occurs independent of direction in space Remus et al. 2012b), the tidal potential would become dependent on all past perturbations. All past terms of the perturbing potential contribute linearly to the tidal potential at the current time. This means that a convolution product comes into play, and for the additional potential this leads to (Boue et al. 2016)

$$\begin{aligned} V_\mathrm{T}(\boldsymbol{r}) &= \sum_{l=2}^{\infty} \left(\frac{R_\mathrm{E}}{|\boldsymbol{r}|} \right)^{l+1} k_l(t) * W_l(\boldsymbol{R}, \boldsymbol{r}_\mathrm{s}(t)) \\ &= \sum_{l=2}^{\infty} \left(\frac{R_\mathrm{E}}{|\boldsymbol{r}|} \right)^{l+1} \int_{-\infty}^{t} k_l(t-t') W_l(\boldsymbol{R}, \boldsymbol{r}_\mathrm{s}(t')) \mathrm{d}t' \,, \end{aligned} \tag{14}$$

where $*$ denotes the convolution product and $k_l(t)$ a Love distribution as described by Efroimsky (2012). The $k_l(t)$ can be seen as a function that links the perturbing potential at time $t' < t$ to the additional tidal potential at the current time t. Consequently, this function describes the response of the body to the perturbations. W_l represents the lth degree term of the perturbing potential in Equation 13. This leaves a description of the Love distribution to be determined to calculate the tidal potential.

3.3. Constant time lag model

An instantaneous response corresponds to a Love distribution of $k_l(t) = k_l \delta(t)$ with $\delta(t)$ the Dirac-delta function. This function satisfies the identity in Equation 15 and is equal to ∞ only when its input is zero and equal to zero otherwise:

$$\int_{-\infty}^{\infty} \delta(t) \mathrm{d}t = 1 \,. \tag{15}$$

The instantaneous response corresponds to a static tidal bulge directly below the perturber and on the connecting position vector. The static Love number k_l can be described as

$$k_l = k_l^0 \frac{1}{1 + A_l} \,, \quad \text{with} \quad A_l = \frac{3\left(2l^2 + 4l + 3\right)\mu}{4l\pi G \rho^2 {R_\mathrm{E}}^2} \,, \tag{16}$$

where l is the degree of the expansion, μ the rigidity, and ρ the density of the body. The fluid Love number $k_l^0 = 3/2(l-1)$ for a homogeneous incompressible viscous sphere. More generally, the Darwin-Radau equation can be used (*e.g.* Jeffreys 1976; Correia et al. 2014):

$$k_l^0 = 5 \left(1 + \left[\frac{5}{2} - \frac{15C}{4M{R_\mathrm{E}}^2} \right]^2 \right)^{-1} - 1 \,. \tag{17}$$

Incorporating the tidal lag into Equation 14 has been done differently in the past. The constant time lag model was proposed by Singer (1968). It assumes that the tidal bulge at time t is caused by the perturbing body at time $t - \Delta t$, where Δt is set a constant. This means that the Love distribution takes up the form of $k_l(t) = k_l \delta(t - \Delta t)$, and that the tidal potential from Equation 14 reduces to

$$V_\mathrm{T}(\boldsymbol{r}) = \sum_{l=2}^{\infty} \left(\frac{R_\mathrm{E}}{|\boldsymbol{r}|} \right)^{l+1} k_l W_l(\boldsymbol{R}, \boldsymbol{r}_\mathrm{s}(t - \Delta t)) \,. \tag{18}$$

When Δt is small enough and consequently $\boldsymbol{r}_\mathrm{s}(t - \Delta t)$ lies close to $\boldsymbol{r}_\mathrm{s}(t)$, the tidal potential from Equation 18 can

be linearized around $\boldsymbol{r}_\mathrm{s}(t)$. Consequently, the gradient of this potential can be retrieved to get the additional force due to the tides (see Equation 19 and Appendix B for a derivation),

$$\begin{aligned}\boldsymbol{F}_\mathrm{T} = -G{M_\mathrm{s}}^2 \sum_{l=2}^{\infty} \Bigg[(l+1) \frac{k_l {R_\mathrm{E}}^{2l+1}}{|\boldsymbol{r}|^{2l+4}} \\ \cdot \left(\boldsymbol{r} + \Delta t \left\{ \frac{l}{2}(\boldsymbol{r}\times\boldsymbol{\omega}+\boldsymbol{v}) + \frac{l+2}{2}\frac{(\boldsymbol{r}\cdot\boldsymbol{v})\boldsymbol{r}}{|\boldsymbol{r}|^2} \right\} \right) \Bigg] ,\end{aligned} \tag{19}$$

where $\boldsymbol{v}$ denotes the velocity vector of the satellite body. The time lag Δt is related to the quality factor and tidal frequency as in Equation 20,

$$\Delta t = \frac{1}{\chi} \arcsin\left(\frac{1}{Q}\right) = \frac{2\delta}{\chi} , \tag{20}$$

where χ is the main tidal frequency and Q the quality factor. The sine relation as in Murray and Dermott (1999); Makarov and Efroimsky (2014); Correia et al. (2014) is used instead of the tangent one used in Goldreich (1963); Efroimsky and Lainey (2007); Lainey et al. (2012). Efroimsky (2012) discusses the correctness of Equation 20 in his Appendix. The main tidal frequency differs per situation. For the tides on the central body, the frequency is given as $\chi = 2|\boldsymbol{\omega} - \boldsymbol{n}|$. Tides on a locked satellite body have a frequency equal to the mean motion $\chi = |\boldsymbol{n}|$.

Note that the angular lag is only equal to the geometric lag angle between bulge and perturbing body (see δ in Figure 3) if the system is in a circular equatorial state. If not, which is usually the case, the total lag should include the lag caused by variations in the radial tides (Efroimsky and Lainey 2007).

For the direct tidal force (Equation 19), the Δt is calculated via the relation with the quality factor, from which multiple estimations are available for different systems. The direct tidal force is truncated to second degree ($l = 2$), which reduces to (*e.g.* Lainey et al. 2007; Lari 2018),

$$\begin{aligned}\boldsymbol{F}_\mathrm{T} = -\frac{3G{M_\mathrm{s}}^2 k_2 {R_\mathrm{E}}^5}{|\boldsymbol{r}|^8} \\ \cdot \left(\boldsymbol{r} + \Delta t \left\{ (\boldsymbol{r}\times\boldsymbol{\omega}+\boldsymbol{v}) + 2\frac{(\boldsymbol{r}\cdot\boldsymbol{v})\boldsymbol{r}}{|\boldsymbol{r}|^2} \right\} \right) .\end{aligned} \tag{21}$$

This equation is used by many and in current day ephemeris determination due to its simplicity and intuitive physical interpretation (Boue et al. 2016). To deal with the tides in the propagation, this force scaled by the reduced mass of the system $\boldsymbol{F}_\mathrm{T}/\beta$ is simply added to the translational EOM in Equation 9.

The rotational evolution is governed by the torque and the total angular momentum conservation. The torque or cross product of the position vector with this force $\boldsymbol{r} \times \boldsymbol{F}_\mathrm{T}$ can be written as

$$\begin{aligned}\boldsymbol{r} \times \boldsymbol{F}_\mathrm{T} &= -\frac{3G{M_\mathrm{s}}^2 k_2 {R_\mathrm{E}}^5}{|\boldsymbol{r}|^8} \Delta t \left(\boldsymbol{r} \times (\boldsymbol{r}\times\boldsymbol{\omega}+\boldsymbol{v})\right) , \\ &= -\frac{3G{M_\mathrm{s}}^2 k_2 {R_\mathrm{E}}^5}{|\boldsymbol{r}|^8} \Delta t \left(\boldsymbol{r}(\boldsymbol{r}\cdot\boldsymbol{\omega}) - \boldsymbol{\omega}|\boldsymbol{r}|^2 + \boldsymbol{r}\times\boldsymbol{v}\right) .\end{aligned} \tag{22}$$

The classical result cited by many (*e.g.* Goldreich and Peale 1966; Mignard 1979; Murray and Dermott 1999) is retrieved for an equatorial and circular orbit, and by noting that $(|\boldsymbol{\omega}| - |\boldsymbol{n}|)\Delta t = \delta$:

$$\boldsymbol{r} \times \boldsymbol{F}_\mathrm{T} = \frac{3G{M_\mathrm{s}}^2 k_2 {R_\mathrm{E}}^5}{2|\boldsymbol{r}|^6} \sin 2\delta . \tag{23}$$

Subsequently, the torque subtracted from the rotational part in Equation 10 gives the tidal contribution to the rotational evolution.

3.4. Satellite tides

All previous assumptions and derivations are made by considering a more massive central body without spin-orbit resonance. All equations can similarly be used regarding a locked less massive body that rotates around a more massive body. The satellite is in a corotant or spin-orbit synchronous state (*i.e.* its mean orbital velocity equals its mean spin rotation velocity). For the case without torques, the same side always faces the more massive body, or more precisely, the empty focus of the system (in Figure 4 denoted with E). The tides are now caused by the more massive body and determined for the less massive one (*i.e.* tides on the satellite body). All above equations can be used when keeping the reference frame at the same point (*i.e.* the body with the tides holds the inertial and rotating frame's center). A sketch of the situation for the tides on a less massive body is shown in Figure 4.

The clear difference with the tides on the primary/central body is shown in the figure. Due to the eccentricity of the orbit, the instantaneous orbital motion varies in time. Because the spin rate remains roughly constant, the tidal bulge will oscillate over the surface of the satellite around the empty focus direction. The caused lag by the dissipation in this oscillating deformation is the reason for a torque on the body. Therefore, the rotation rate of the satellite will see a periodical evolution, which are denoted librations and librational tides.

The radial tides are the variations of the amplitude of the tidal bulge. They are easily explained by the difference in the radial distance between the perturbing and tidal body due to the eccentric orbit. Both the librational and radial tides add up to the tidal dissipation inside the body and to additional tidal forces on the central body. However, it is difficult to deal with these tides in a dynamical system. According to Murray and Dermott (1999) the librational tides dissipate exactly 4/3 times as much energy as the radial tides. In current day satellite ephemeris

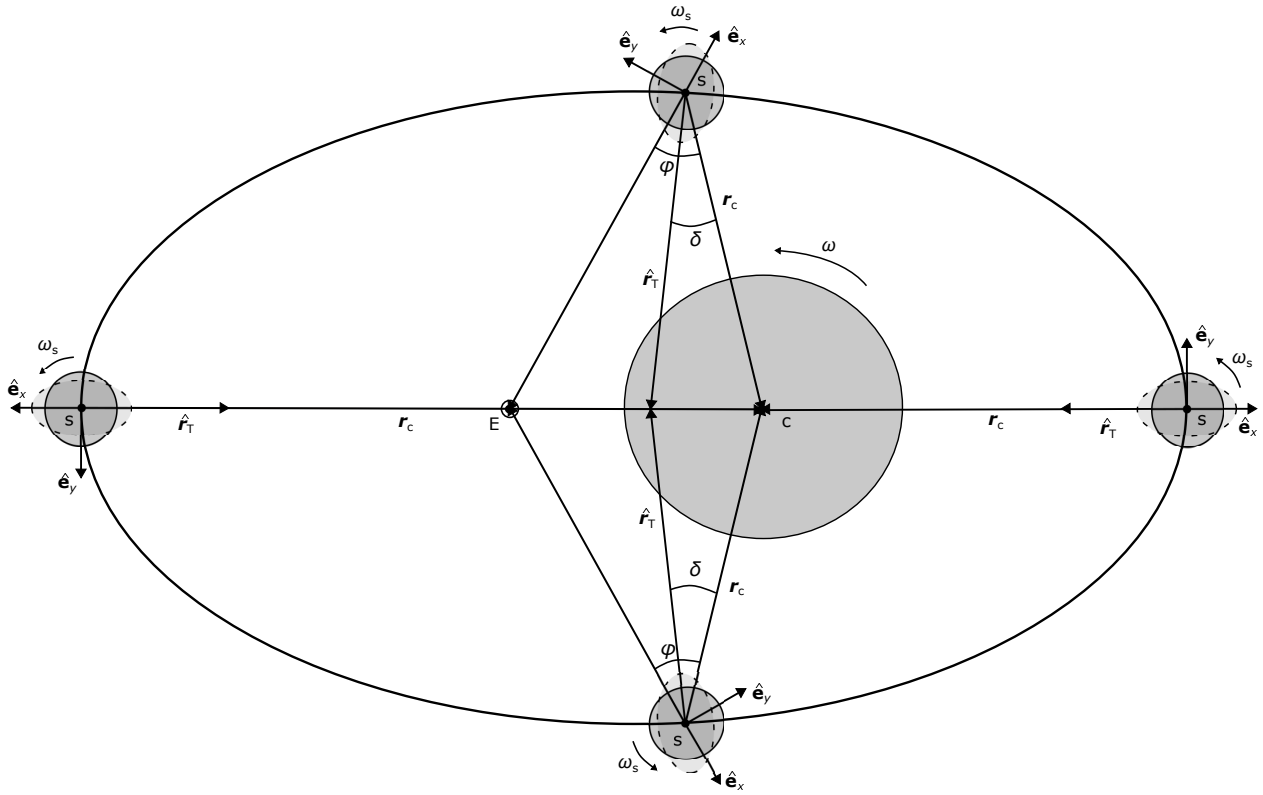

Figure 4: Tidal lag of the tidal bulge on a locked satellite with an eccentric orbit. δ is here the tidal geometric lag angle and $\hat{\boldsymbol{r}}_\mathrm{T}$ the direction of the tidal bulge. ϕ is the angular separation between the main body direction and the empty focus of the system, denoted with E.

determination (*e.g.* Lainey et al. 2009; Lari 2018) this detail is used to simplify the resulting tidal force on the central body due to the tides on the satellite. The tidal force given by Equation 21 is used to calculate an average radial tidal force by employing the orbital angular velocity $\boldsymbol{\omega} = \boldsymbol{r} \times \boldsymbol{v}/|\boldsymbol{r}|^2$, instead of the spin rate of the body, and thereafter 4/3 of this force is added to get a total tidal force:

$$\begin{aligned}\boldsymbol{F}_{\mathrm{T,rad}} &= -\frac{3GM_\mathrm{c}{}^2 k_2 R_\mathrm{E}{}^5}{|\boldsymbol{r}|^8}\Delta t\left(\boldsymbol{r}\times\frac{\boldsymbol{r}\times\boldsymbol{v}}{|\boldsymbol{r}|^2}+\boldsymbol{v}+2\frac{(\boldsymbol{r}\cdot\boldsymbol{v})\boldsymbol{r}}{|\boldsymbol{r}|^2}\right)\\ &= -\frac{3GM_\mathrm{c}{}^2 k_2 R_\mathrm{E}{}^5}{|\boldsymbol{r}|^8}\Delta t\left(\frac{\boldsymbol{r}(\boldsymbol{r}\cdot\boldsymbol{v})-\boldsymbol{v}(\boldsymbol{r}\cdot\boldsymbol{r})}{|\boldsymbol{r}|^2}+\boldsymbol{v}+2\frac{(\boldsymbol{r}\cdot\boldsymbol{v})\boldsymbol{r}}{|\boldsymbol{r}|^2}\right)\\ &= -\frac{3GM_\mathrm{c}{}^2 k_2 R_\mathrm{E}{}^5}{|\boldsymbol{r}|^8}\Delta t\left(3\frac{(\boldsymbol{r}\cdot\boldsymbol{v})\boldsymbol{r}}{|\boldsymbol{r}|^2}\right)\ ,\end{aligned} \tag{24}$$

$$\boldsymbol{F}_\mathrm{T} = -\frac{3GM_\mathrm{c}{}^2 k_2 R_\mathrm{E}{}^5}{|\boldsymbol{r}|^8}\Delta t\left(7\frac{(\boldsymbol{r}\cdot\boldsymbol{v})\boldsymbol{r}}{|\boldsymbol{r}|^2}\right)\ . \tag{25}$$

The term independent of Δt in Equation 21 is left by Lari (2018). This is justified in Lainey et al. (2012) by stating that it is only a small drift and that it generates no secular acceleration because it causes no torque.

Overall, Equation 25 may be a good approximation, it is however only valid when assuming the satellite's quality factor to be independent of amplitude and frequency (Murray and Dermott 1999). The constant quality factor is not able to describe the long term evolution of the secular effects. The same holds for short term translational and rotational evolution in the case of sufficiently high accuracy requirements. Moreover, the two different tides have a phase difference of $\pi/2$ (Murray and Dermott 1999). This effect has to be taken into account, and the simple adding of the two would be generally incorrect.

4. Coupled Model

The direct tidal force has been introduced and described (Equation 21 and Equation 25 in Section 3). In this section, the coupled way of incorporating the tidal behaviour is discussed. This new approach is the main topic of this research. Instead of adding a direct tidal force to the equations of motion, the tidal deformation of the body is now determined through a differential equation for the spherical harmonic gravitational coefficients. This change in mass distribution, which corresponds to what these coefficients truly represent, modify the potential gravitational field. Hence, the translational and rotational motion are directly influenced through these changes in the coefficients.

4.1. Maxwell Rheology

To get these changes in the gravitational potential coefficients, the structure and deformation of the tidal body have to be modelled. A rheology is the model of the body's structure and material when a stress or thus force is applied. It determines its response due to a receiving stress. In terms of the tidal potential in Equation 14, it gives a description of the Love distribution and defines the deformation under a perturbing force. A realistic rheological approach would be to assume the body viscoelastic (Correia et al. 2014). This body would have viscous, (*i.e.* the deformation is resisted linearly over time when a stress is applied), but also elastic properties (*i.e.* the body deforms instantly under a stress and returns directly back to its initial form when the stress is removed).

One of the simplest form, and more easily incorporated in this coupled model, is the Maxwell model (Correia et al. 2014). It is used by numerous authors for describing the response of a body (*e.g.* Remus et al. 2012a; Correia et al. 2014; Ferraz-Mello 2015; Boue et al. 2016). The model describes the material's response as a simple elastic spring with modulus μ_0 followed by a viscous damper with viscosity η in series (Turcotte et al. 2002), see Equation 26,

$$\frac{\mathrm{d}\epsilon}{\mathrm{d}t} = \frac{1}{\mu_0}\frac{\mathrm{d}\sigma}{\mathrm{d}t} + \frac{\sigma}{\eta}\,, \tag{26}$$

where ϵ denotes the strain and σ the stress at a point on the body. If a stress is applied to the material, the elastic spring makes it instantly deform and the viscous damper would ensure a constant deformation rate. When the stress is again removed, the elastic spring returns to its original position while the viscous damper's deformation is held in place. This relation between stress and strain or deformation is used to derive a differential equation for the tidal potential, which results into Equation 27 for the lth term of the additional tidal potential from Equation 14 (see the appendix of Correia et al. 2014):

$$V_{\mathrm{T},l} + \tau_l \frac{\mathrm{d}V_{\mathrm{T},l}}{\mathrm{d}t} = V^{\mathrm{e}}_{\mathrm{T},l} + \tau_{\mathrm{e}} \frac{\mathrm{d}V^{\mathrm{e}}_{\mathrm{T},l}}{\mathrm{d}t}\,, \tag{27}$$

where $V^{\mathrm{e}}_{\mathrm{T},l}$ is the equilibrium tidal potential, when the perturbations would be static or the response instantaneous. The $\tau_{\mathrm{e}} = \eta/\mu_0$ is a Maxwell relaxation time and $\tau_l = \tau_{\mathrm{e}}\,(1 + A_l)$ denotes a global relaxation time. If these are zero, the additional tidal potential reduces to the equilibrium potential. If they are surpassed in time during the simulation, the transient in the derivatives damps out. These relaxation times are related (for $l = 2$) to the direct tidal force model through their relation with the k_2 and Q (Correia et al. 2014),

$$k_2 = k_2^0 \sqrt{\frac{1 + \tau_{\mathrm{e}}^2 \chi^2}{1 + \tau_2^2 \chi^2}}\,, \tag{28}$$

$$\tan\left(\arcsin\frac{1}{Q}\right) = \tan\delta = \frac{(\tau_2 - \tau_{\mathrm{e}})\chi}{1 + \tau_2 \tau_{\mathrm{e}} \chi^2}\,, \tag{29}$$

$$\frac{k_2}{Q} = k_2^0 \frac{(\tau_2 - \tau_{\mathrm{e}})\chi}{1 + (\tau_2 \chi)^2}\,. \tag{30}$$

These equations are key in comparing the coupled model with the direct tidal force model from Section 3, as the different input constants are hereby linked.

4.2. The tidal coefficients

To govern the deformation, an equation for the varying spherical harmonic coefficients is needed. Similarly to the differential equation for the additional potential in Equation 27, an equation for the coefficients can be derived (Correia et al. 2014; Boue et al. 2016). For $\Delta C_{l,m}$ or $\Delta S_{l,m}$ for convenience expressed as a single $\Delta Z_{l,m}$, it holds that

$$\Delta Z_{l,m} + \tau_l \frac{\mathrm{d}\Delta Z_{l,m}}{\mathrm{d}t} = \Delta Z^{\mathrm{e}}_{l,m} + \tau_{\mathrm{e}} \frac{\mathrm{d}\Delta Z^{\mathrm{e}}_{l,m}}{\mathrm{d}t}\,, \tag{31}$$

where $\Delta Z^{\mathrm{e}}_{l,m}$ is the coefficient at equilibrium. Following Ferraz-Mello (2015) and Boue et al. (2016), the additional coefficients can be substituted with

$$\Delta Z_{l,m} = \left(1 - \frac{\tau_{\mathrm{e}}}{\tau_l}\right) \Delta Z^{\nu}_{l,m} + \frac{\tau_{\mathrm{e}}}{\tau_l} \Delta Z^{\mathrm{e}}_{l,m}\,, \tag{32}$$

where $Z^{\nu}_{l,m}$ is the new variable to be used in the differential equation. This removes the equilibrium coefficient derivative:

$$\tau_{\mathrm{l}} \frac{\mathrm{d}\Delta Z^{\nu}_{l,m}}{\mathrm{d}t} = \Delta Z^{\mathrm{e}}_{l,m} - \Delta Z^{\nu}_{l,m}\,. \tag{33}$$

At a surface position $\boldsymbol{R}$ the equilibrium potential is defined to be equal to the perturbing potential times the fluid Love number:

$$V^{\mathrm{e}}_{T,l}(\boldsymbol{R}) = k^0_{\mathrm{l}} W_l(\boldsymbol{R})\,. \tag{34}$$

Substituting Equation 2 and Equation 13 in Equation 34 leads to the equilibrium coefficients of degree l and order m:

$$\begin{aligned}\Delta C^{\mathrm{e}}_{l,m} =& k^0_l \frac{M_{\mathrm{s}}}{M_{\mathrm{c}}} \left(\frac{|\boldsymbol{R}|}{|\boldsymbol{r}_{\mathrm{s}}|}\right)^{l+1} (2 - \delta_{0m}) \\ &\cdot \frac{(l-m)!}{(l+m)!} \cos\!\big(m\phi_{\boldsymbol{r}_{\mathrm{s}}}\big) P_{l,m}\big(\cos\vartheta_{\boldsymbol{r}_{\mathrm{s}}}\big)\,,\end{aligned} \tag{35}$$

$$\begin{aligned}\Delta S^{\mathrm{e}}_{l,m} =& k^0_l \frac{M_{\mathrm{s}}}{M_{\mathrm{c}}} \left(\frac{|\boldsymbol{R}|}{|\boldsymbol{r}_{\mathrm{s}}|}\right)^{l+1} (2 - \delta_{0m}) \\ &\cdot \frac{(l-m)!}{(l+m)!} \sin\!\big(m\phi_{\boldsymbol{r}_{\mathrm{s}}}\big) P_{l,m}\big(\cos\vartheta_{\boldsymbol{r}_{\mathrm{s}}}\big)\,,\end{aligned} \tag{36}$$

where δ_{0m} is the Kronecker delta and equal to one if $m = 0$ and zero otherwise.

4.3. Equations of motion for the coupled model

The full equations of motion can now be specified for the 2-dimensional system portrayed in Figure 1. The varying spherical harmonic coefficients are described with $Z_{l,m}(t) = Z^0_{l,m} + \Delta Z_{l,m}(t)$, leading to the following set of first order differential equations (Equations 37 to 41):

$$\frac{\mathrm{d}\boldsymbol{r}}{\mathrm{d}t} = \boldsymbol{v}\,, \tag{37}$$

$$\begin{aligned}\frac{\mathrm{d}\boldsymbol{v}}{\mathrm{d}t} =& -\frac{G(M_\mathrm{s}+M_\mathrm{c})}{|\boldsymbol{r}|^3}\boldsymbol{r} - \frac{3G(M_\mathrm{s}+M_\mathrm{c}){R_\mathrm{E}}^2}{2|\boldsymbol{r}|^5}J_2(t)\boldsymbol{r} \\ &+\frac{9G(M_\mathrm{s}+M_\mathrm{c}){R_\mathrm{E}}^2}{|\boldsymbol{r}|^5}\big(C_{2,2}(t)\cos 2\gamma - S_{2,2}(t)\sin 2\gamma\big)\boldsymbol{r} \\ &+\frac{6G(M_\mathrm{s}+M_\mathrm{c}){R_\mathrm{E}}^2}{|\boldsymbol{r}|^4}\big(C_{2,2}(t)\cos 2\gamma + S_{2,2}(t)\sin 2\gamma\big)(\hat{\boldsymbol{e}}_\mathrm{C}\times\boldsymbol{r})\,,\end{aligned} \tag{38}$$

$$\frac{\mathrm{d}\boldsymbol{\omega}}{\mathrm{d}t} = -\frac{6GM_\mathrm{s}M_\mathrm{c}{R_\mathrm{E}}^2}{C|\boldsymbol{r}|^3}\left(C_{2,2}(t)\cos 2\gamma + S_{2,2}(t)\sin 2\gamma\right)\hat{\boldsymbol{e}}_\mathrm{C}\,, \tag{39}$$

$$\frac{\mathrm{d}\boldsymbol{q}}{\mathrm{d}t} = \boldsymbol{Q}(\boldsymbol{q})\boldsymbol{\omega}\,, \tag{40}$$

$$\frac{\mathrm{d}\Delta Z^\nu_{l,m}}{\mathrm{d}t} = \frac{1}{\tau_l}\left(\Delta Z^\mathrm{e}_{l,m} - \Delta Z^\nu_{l,m}\right),\ l,m = (2,0) \text{ or } (2,2)\,. \tag{41}$$

The $\Delta Z_{l,m}(t)$ are determined via their relation in Equation 32, and the equilibrium coefficients for degree 2 are given by

$$\Delta J^\mathrm{e}_2 = \frac{k^0_2}{2}\frac{M_\mathrm{s}}{M_\mathrm{c}}\left(\frac{R_\mathrm{E}}{|\boldsymbol{r}|}\right)^3\,, \tag{42}$$

$$\Delta C^\mathrm{e}_{2,2} = \frac{k^0_2}{4}\frac{M_\mathrm{s}}{M_\mathrm{c}}\left(\frac{R_\mathrm{E}}{|\boldsymbol{r}|}\right)^3\cos 2\gamma\,, \tag{43}$$

$$\Delta S^\mathrm{e}_{2,2} = -\frac{k^0_2}{4}\frac{M_\mathrm{s}}{M_\mathrm{c}}\left(\frac{R_\mathrm{E}}{|\boldsymbol{r}|}\right)^3\sin 2\gamma\,, \tag{44}$$

where k^0_2 is given by Equation 17, and the trigonometric functions by Equation 4. The principal moment of inertia C is related to the spherical harmonic coefficient $J_2(t)$ through

$$C(t) = \left(2/3 J_2(t) + \xi\right) M_\mathrm{c}{R_\mathrm{E}}^2\,, \tag{45}$$

and is now time dependent. The quaternion operator $\boldsymbol{Q}(\boldsymbol{q})$ is defined by Equation 11, and the unit axis of the rotating frame by their relation to the quaternion vector (described clearly in Equation A24 of Fukushima 2008, see Appendix A). The dependency of ΔJ^e_2 on the rotation vector as discussed in Correia et al. (2014) is left out. This parameter is assumed to be almost constant and thus the static coefficient can account for it. It does not have an additional effect on the secular evolution, because it causes no torque.

To summarize, the coupled model consists of a state vector $[\boldsymbol{r},\ \boldsymbol{v},\ \boldsymbol{\omega},\ \boldsymbol{q},\ \Delta J^\nu_2,\ \Delta C^\nu_{2,2},\ \Delta S^\nu_{2,2}]$. The $\boldsymbol{r}$ and $\boldsymbol{v}$ vectors denote respectively the position and the velocity of the perturbing body as seen from the inertial reference frame centered in the opposite body. $\boldsymbol{\omega}$ and $\boldsymbol{q}$ denote the rotation and orientation vector of the tidal body (*i.e.* the body with the tides). The tidal coefficients relate to the spherical harmonics on the tidal body. Body properties set in the model are the mass M_s of the perturbing body, the mass M_c and equatorial reference radius R_E of the tidal body, the static spherical harmonic coefficients J^0_2, $C^0_{2,2}$ and $S^0_{2,2}$ related to the tidal body and the mean moment of inertia ξ of that body. The relaxation times τ_e and τ_2 are also specified for the tidal body, via their relation with the k_2 and Q (in Equation 28-30).

5. Validation/Comparison methods

To be able to compare the coupled model's behaviour, literature approximations of the secular effects are described. These include the semi-major axis and eccentricity evolution of the system. Furthermore, the comparison method for the tidal geopotential coefficients is stated. The determination of the tidal lag angle from these coefficients is explained. Then, the periodical effects of the librations and their contribution on the tidal dissipation in the system are discussed. In Section 6 and 7, these comparison methods will be used to describe and quantify the behaviour of the coupled model. This means that the current section is key to be able to state the usefulness of the coupled model.

5.1. Secular effects

In Section 3 already, the secular effect of the semi-major axis has been quickly described. Due to the lagging tidal bulge, a torque is generated on the tidal body, causing the tidal body's spin vector to change, and due to the angular momentum conservation, this is accompanied by a rise or fall of the semi-major axis. Note the rise or fall in this matter, as this is entirely dependent on whether the tidal bulge is lagging the position of the perturbing body, or preceding. To incorporate this phenomenon in the direct equation for the secular effects a sign function is used. Because it is of importance whether the tidal bulge lags or precedes the position of the perturber, it consequently also means that a difference exists between tides on the primary and tides on the secondary body, as the tides oscillate between a lagging and preceding position on a locked secondary. For the tides on the primary, the change in semi-major axis is commonly described as (*e.g.* Souchay et al. 2013; Boué 2019),

$$\frac{\mathrm{d}a}{\mathrm{d}t} = \mathrm{sign}(\Omega - n)3\frac{k_2}{Q}\frac{M_\mathrm{s}}{M_\mathrm{c}}\left(\frac{R_\mathrm{E}}{a}\right)^5 na\,, \tag{46}$$

where the $\mathrm{sign}(x)$ function is positive for positive x and negative otherwise. Furthermore, a denotes the semi-major axis, Ω the angular longitudinal velocity, and n the mean motion of the system. Equation 46 is derived by making use of the total angular momentum conservation and by taking the following assumptions on the orbit. The orbit is

assumed to be equatorial, prograde, and circular, the tidal lag to be constant and independent of the tidal frequency, the moment of inertia of the central body to be constant, the spin vector of the central body to be aligned with its polar axis and the mass of the central body to be much larger than the mass of the satellite (for a derivation see Souchay et al. 2013 Section 5.3).

The tides cause an eccentricity change as well, however, it is harder to grasp. Whenever a non-zero eccentricity, the tidal torque will cause a secular effect in the eccentricity. Expanding the tidal potential in Fourier series and converting to orbital elements gives the change in eccentricity for tides on the primary as (*e.g.* Jeffreys 1976; Souchay et al. 2013),

$$\frac{\mathrm{d}e}{\mathrm{d}t} = \mathrm{sign}(3\Omega - 2n)\frac{57}{8}\frac{k_2}{Q}\frac{M_\mathrm{s}}{M_\mathrm{c}}\left(\frac{R_\mathrm{E}}{a}\right)^5 ne\,, \tag{47}$$

with e here the eccentricity of the system. The same assumptions are made as for the derivative of the semi-major axis, except that the orbit is no longer circular. The different sign function originates from the fact that the eccentricity is affected by other tidal components than the diurnal bulge (Goldreich and Soter 1966).

For the tides on a locked satellite body (*i.e.* a secondary body of less mass than the primary and a mean rotation period equal to the mean orbital period), the secular effects are different. The tidal angular lag cannot be assumed roughly constant as it librates across the surface. This fact makes it more difficult to calculate the secular effects correctly, which is demonstrated by the fact that still a discussion is held in recent literature papers about the approximation of the semi-major axis evolution caused by the satellite tides (Souchay et al. 2013; Boué 2019). They differ with a factor 57/21, see Equation 48 and 49, that display the semi-major axis evolution of the system caused by the tides on the satellite body.

$$\frac{\mathrm{d}a}{\mathrm{d}t} = -21\frac{k_2}{Q}\frac{M_\mathrm{c}}{M_\mathrm{s}}\left(\frac{R_\mathrm{E}}{a}\right)^5 nae^2\,, \tag{48}$$

$$\frac{\mathrm{d}a}{\mathrm{d}t} = -57\frac{k_2}{Q}\frac{M_\mathrm{c}}{M_\mathrm{s}}\left(\frac{R_\mathrm{E}}{a}\right)^5 nae^2\,. \tag{49}$$

The k_2, Q, and R_E are now denoting the satellite's body Love number, Quality factor, and equatorial radius. Equation 48 is more commonly accepted and used. Both approximations are considered in this research, and it will be interesting to see if the coupled model can state more on the matter.

The eccentricity evolution of the system caused by the tides on the satellite body are given in Equation 50 (Boué 2019),

$$\frac{\mathrm{d}e}{\mathrm{d}t} = -\frac{21}{2}\frac{k_2}{Q}\frac{M_\mathrm{c}}{M_\mathrm{s}}\left(\frac{R_\mathrm{E}}{a}\right)^5 ne\,. \tag{50}$$

The literature approximations of Equation 48-50 are derived for the case that $n = \Omega$, the mean motion is equal to the spin rate of the satellite (*i.e.* it is in a 1:1 spin-orbit locked state).

5.2. The tidal coefficients

The tidal coefficients are retrieved from the state variable according to Equation 32. In current coefficients determination this is done with a complex Love number to take account for the lag, see Equation 51 (Petit and Luzum 2010).

$$\begin{aligned}
\Delta J_2 &= \frac{1}{2}\frac{M_\mathrm{s}}{M_\mathrm{c}}\left(\frac{R_\mathrm{E}}{|\boldsymbol{r}|}\right)^3 \mathrm{Re}(k_2)\,,\\
\Delta C_{2,2} &= \frac{1}{4}\frac{M_\mathrm{s}}{M_\mathrm{c}}\left(\frac{R_\mathrm{E}}{|\boldsymbol{r}|}\right)^3 \left(\mathrm{Re}(k_2)\cos 2\gamma - \mathrm{Im}(k_2)\sin 2\gamma\right)\,,\\
\Delta S_{2,2} &= -\frac{1}{4}\frac{M_\mathrm{s}}{M_\mathrm{c}}\left(\frac{R_\mathrm{E}}{|\boldsymbol{r}|}\right)^3 \left(\mathrm{Re}(k_2)\sin 2\gamma + \mathrm{Re}(k_2)\cos 2\gamma\right)\,.
\end{aligned} \tag{51}$$

Here denote $\mathrm{Re}(k_2)$ and $\mathrm{Im}(k_2)$ the real and imaginary part of the Love number, respectively, and are stated in Equation 52.

$$\begin{aligned}
k_2 &= |k_2|\exp(-i\cdot 2\delta) = \mathrm{Re}(k_2) + i\,\mathrm{Im}(k_2)\,,\\
\mathrm{Re}(k_2) &= |k_2|\cos 2\delta \approx |k_2|\,,\\
\mathrm{Im}(k_2) &= -|k_2|\sin 2\delta = -|k_2|/Q\,.
\end{aligned} \tag{52}$$

The last equality in Equation 52 follows from the definition of the quality factor (Equation 20). The real part is assumed equal to the literature value of the Love number.

The tidal coefficients state the gravitational shape of the body, and thus contain the bulge's position and geometric lag angle with respect to the perturber. The geometric lag angle is determined via Equation 53.

$$\begin{aligned}
\nu &= \frac{1}{2}\mathrm{arctan2}\left(\frac{\Delta S_{2,2}}{\Delta C_{2,2}}\right)\\
\gamma &= (\mathrm{sign}(\hat{\boldsymbol{e}}_\mathrm{A}\cdot(\hat{\boldsymbol{r}}\times\hat{\boldsymbol{e}}_\mathrm{C}))\cdot\arccos(\hat{\boldsymbol{e}}_\mathrm{A}\cdot\hat{\boldsymbol{r}})) \mod 2\pi\\
\delta &= (\nu-\gamma) \mod \pi
\end{aligned} \tag{53}$$

The geometric tidal lag angle is denoted by δ, ν is the angle of the tidal bulge with respect to the rotating x-axis ($\hat{\boldsymbol{e}}_\mathrm{A}$), and γ is the angle of the satellite with respect to the rotating x-axis. The geometric tidal lag angle is compared to the literature value defined by the quality factor from Equation 20. The current models (see Equation 21 in Section 3) use indirectly a constant geometric tidal lag angle. The coupled model should be able to show a difference and a periodical variation of this tidal lag angle.

The time lag of the tidal bulge's position is directly related to the tidal geometric lag angle. The coupled model should state a per-period variation of this time lag, which cannot be done with the currently used direct tidal force model (Equation 21). The time lag Δt is determined via Equation 54

$$\Delta t = \frac{\delta|\boldsymbol{r}|}{|\boldsymbol{\omega}\times\boldsymbol{r}-\boldsymbol{v}|}\,, \tag{54}$$

which is in fact a distance between the bulge's position and the perturber's position divided by the relative rotational velocity.

5.3. Librations

The periodic effects do not directly influence the long term evolution, but can indirectly still have a huge impact due to their caused dissipation. Librations are a periodic wagging or wavering of the apparent face of a satellite as seen from an observer on the central body. The optical libration described already, denotes the fact that the same face always points towards the empty focus. The libration angle is thus the angular distance between the empty focus and the perturbing central body (in Figure 4 denoted with ϕ). This angle is in literature given as

$$\phi \approx 2e \sin M \,, \tag{55}$$

with M the mean anomaly (Dirkx et al. 2016).

Apart from this optical libration, improper initial conditions and torques acting on the satellite cause an additional libration around this empty focus point. These are the physical librations, consisting of free or proper librations and forced librations. The free librations usually damp out and are only a phenomenon from a numerical analysis and caused by imperfect initial conditions. Their main frequency is a function of the relative moment of inertia $(B-A)/C$ with $A \leq B \leq C$ the moment of inertia in the three axis directions, and is given by Equation 56 (Le Maistre et al. 2013),

$$\nu_\tau = n\sqrt{\frac{B-A}{C}} \,. \tag{56}$$

The normalized moment of inertia are related to the geopotential coefficients through Equation 57,

$$\begin{aligned} A &= -2C_{2,2} - \frac{1}{3}J_2 + \xi \,, \\ B &= 2C_{2,2} - \frac{1}{3}J_2 + \xi \,, \\ C &= \frac{2}{3}J_2 + \xi \,, \end{aligned} \tag{57}$$

where ξ is again the mean normalized moment of inertia.

The forced librations are different because they do not damp out as long as the torque is acting on the body. Usually a 1:1 orbit-libration period coupling has the largest influence. Its amplitude is given in Equation 58 (Willner et al. 2010),

$$\theta_\tau = \frac{2e}{1 - \frac{C}{3(B-A)}} \,. \tag{58}$$

or in Equation 59 (Efroimsky 2018),

$$\theta_\tau = -6e\frac{B-A}{C} + \mathcal{O}(e^3) \,. \tag{59}$$

Efroimsky (2018) uses a different amplitude approximation, but Equation 58 is more commonly used and will also be used for the validation.

The true physical librations per epoch are determined via the variation in the rotation angle. The rotation angle (in Figure 1 displayed as θ) denotes the angle between the fixed rotating and inertial frame, which includes here a single angle as it is a 2-dimensional problem. The rotation angle is calculated via its relation with the unit axis (see Equation 60),

$$\theta = \arctan2(\hat{\boldsymbol{e}}_\mathrm{A}(y)/\hat{\boldsymbol{e}}_\mathrm{A}(x)) \,. \tag{60}$$

Subsequently, the rotation angle is unwrapped and a linear least-squares fit is subtracted leaving the variations in the rotation angle (*i.e.* the physical librations).

These librations, free and forced, both could have an influence on the dissipation inside the body. The librations cause a possible friction due to the deformation of the body, which causes the dissipation of energy. Recently, Efroimsky (2018) stated in a theoretical work the relative power of this additional dissipation with respect to the tidally induced power as if there were no forced or free librations. The coupled model should be able to automatically incorporate this and thus it is interesting to see the behaviour of the tides on a locked body with large librations ($\approx 1.0°$). Phobos is assumed to show this librational motion, with values of 1.1° for the librational amplitude (Willner et al. 2010).

Equation 61 shows this time averaged power for the principal 1:1 spin-orbit resonance,

$$\frac{\langle P \rangle_\mathrm{tide}^{(\mathrm{lib})}}{\langle P \rangle_\mathrm{tide}^{(\mathrm{main})}} = 1 - \frac{4}{7}\frac{\theta_\tau}{e} + \frac{1}{7}\frac{{\theta_\tau}^2}{e^2} + \frac{1}{7}\frac{{\theta_\mathrm{f}}^2}{e^2} \,, \tag{61}$$

where the (lib) and (main) superscripts denote the total average tidal power including the forced and free librations, and the main average tidal power as if there were no librations. The free libration amplitude is expressed with θ_f. Assumptions taken here are a zero obliquity, a limit of a free libration amplitude of under 12°, and a satellite body which is near-spherical and follows a Maxwell rheology.

Because the changes in the orbital elements are ultimately dependent on the amount of energy dissipated, a different evolution of these elements is expected. From Correia et al. (2014) it is given that the energy dissipation is as

$$\frac{\mathrm{d}E}{\mathrm{d}t} = -\left(\frac{\mathrm{d}E_\mathrm{orb}}{\mathrm{d}t} + \frac{\mathrm{d}E_\mathrm{rot}}{\mathrm{d}t}\right) , \tag{62}$$

with E_orb and E_rot the respective orbital and rotational energy change. Those have a relation with the orbital evolution as in Equation 63,

$$\begin{aligned} \frac{\mathrm{d}a}{\mathrm{d}t} &= \frac{2}{\beta a n^2}\frac{\mathrm{d}E_\mathrm{orb}}{\mathrm{d}t} \,, \\ \frac{\mathrm{d}e}{\mathrm{d}t} &= \frac{1-e^2}{\beta a^2 n e}\left(\frac{1}{n}\frac{\mathrm{d}E_\mathrm{orb}}{\mathrm{d}t} + \frac{1}{\Omega\sqrt{1-e^2}}\frac{\mathrm{d}E_\mathrm{rot}}{\mathrm{d}t}\right) . \end{aligned} \tag{63}$$

Here denotes β again the reduced mass of the system and Ω the angular longitudinal velocity of the spin vector. As

the energy change alters because of the additional dissipation due to the librations, the orbital elements will see a different derivative as well. Assuming a domination of the orbital energy, which is usually the case, the change in total energy will result in an effect on the orbital energy mostly. Then, the evolution of the orbital elements approximation is modified according to Equation 64,

$$\begin{aligned} \frac{\mathrm{d}a}{\mathrm{d}t} &= \frac{\langle P \rangle_{\text{tide}}^{(\text{lib})}}{\langle P \rangle_{\text{tide}}^{(\text{main})}} \left.\frac{\mathrm{d}a}{\mathrm{d}t}\right|_{\text{Literature}} , \\ \frac{\mathrm{d}e}{\mathrm{d}t} &= \frac{\langle P \rangle_{\text{tide}}^{(\text{lib})}}{\langle P \rangle_{\text{tide}}^{(\text{main})}} \left.\frac{\mathrm{d}e}{\mathrm{d}t}\right|_{\text{Literature}} . \end{aligned} \tag{64}$$

The literature approximations in Equation 48-49 and Equation 50 will have to be adjusted for this additional tidal dissipation.

6. Application: Tides on the primary

The coupled model needs to be applied to be able to check the relevance of the model for future ephemeris determination. Two systems regarded here are the Mars-Phobos and the Earth-Moon system. The full initial state and constants for the propagation are stated and the results are compared using the behaviour analysis methods described in Section 5. The current section deals with the tides on a primary body.

6.1. Setup and input parameters

The simulations were performed for two systems, the Mars-Phobos and the Earth-Moon system. In these simulations, the more massive central bodies have an extended spherical body of degree 2 and thus experience tides. The reference frame is centered in these bodies. The satellite bodies are regarded as point masses (see for the problem details again Figure 1). Constants used are summarised in Table 1. The global relaxation time τ_2 and Maxwell relaxation time τ_{e} can be determined from their relation with k_2 and Q prior to the simulations, and are also stated in Table 1.

The initial state vector (position and velocity) is based on current values of semi-major axis and eccentricity, but put in a equatorial orbit to mimic a 2D case. The runs performed are thus not mimicking the real case. The inertial and rotating frame are assumed to coincide at the start of the propagation. This leads to the initial state in Table 2, based on the orbital elements and rotation parameters provided in Table 3.

The propagations were performed using the *solve_ivp* routine from the scipy.integrate module in Python. It solves a system of first order differential equations with a given initial value and propagates until a specified time. The method of integration used was an explicit Runge-Kutta method of order 8 named DOP853[1] based on a method by Dormand and Prince (Hairer et al. 2009) that uses a variable step size in the numerical propagation. Per step tolerances can be set and a relative tolerance of 2.3×10^{-14} and an absolute tolerance of 1.0×10^{-19} are used. The relative tolerance is here set at the software's minimum. The solver then keeps the local error estimates below $\text{atol} + \text{rtol} \cdot \text{abs}(y)$.

The propagations ran are given in Table 4. The Mars-Phobos propagations are run for 180 Martian days. In this time span 30000 equidistant states have been collected. The duration is chosen to be way beyond the Martian relaxation time of 19.8 Martian days. In this way, the transient should be damped. The Earth-Moon propagations (with a global relaxation time of only 2.1 days) are run for 480 Earth days and 40000 equidistant states have been collected. A longer propagation period is chosen for the Earth-Moon run, because the orbital period of the Moon is larger than the small orbital period of Phobos (*i.e.* 27.4 Earth days to 0.3 Martian days, respectively).

No static gravity field coefficients are set, because they come with large once-per-orbit variations. This would make it too difficult to retrieve the change in semi-major axis and eccentricity for the short time scales used.

The comparison between the current direct tidal force model and the coupled model is performed after the transient converges. New comparison runs are based on final state variables from converged coupled model propagations. That will be discussed in Section 6.3.

6.2. Tidal coefficients

The unnormalized tidal coefficients of the undamped coupled simulation (MPhCd1) are displayed in Figure 5. The other state variables are not plotted here, as their information is primarily used for the verification, and not for the validation of the coupled model. If plotted, the figures would show non-interesting behaviour, as expected from a nearly spherical 2-dimensional orbit.

The convergence of the tidal coefficients can be seen in Figure 5. This plot clearly shows that the coefficients converge towards an equilibrium value. The J_2-coefficient converges towards a positive value, while the other two coefficients follow a periodic function around zero. This is expected, as the coefficients should resemble the equilibrium coefficients after the global relaxation time is exceeded. The time until the convergence can be seen as the time the body (*i.e.* Mars) needs to adjust to the suddenly exposed stress. In reality, Mars would already be in this equilibrium state of tidal behaviour, as it has already experienced these stresses for a long time. The Martian global relaxation time of 19.8 Martian days results into a damping of the transient of over $\exp(-180/19.8)$ after the 180 Martian days propagation.

[1] `https://docs.scipy.org/doc/scipy/reference/generated/scipy.integrate.solve_ivp.html#id5`

Constant	Mars-Phobos	Source	Earth-Moon	Source
G [$m^3\,kg^{-1}\,s^{-2}$]	$6.674\,08 \times 10^{-11}$	CODATA 2014	$6.674\,08 \times 10^{-11}$	CODATA 2014
M_c [kg]	6.4171×10^{23}	Wiki	$5.972\,364\,730\,419 \times 10^{24}$	IAU 2015 Resolution B 3
M_s [kg]	1.0659×10^{16}	Wiki	7.342×10^{22}	Wiki
R_E [m]	3396.0×10^{3}	Genova et al. (2016)	6378.1×10^{3}	IAU 2015 Resolution B 3
ξ [-]	0.3662	Wiki (Folkner 1997)	0.3307	Wiki
k_2 [-]	0.152	Lainey et al. (2007)	0.299	Murray and Dermott (1999)
Q [-]	79.91	Lainey et al. (2007)	12	Murray and Dermott (1999)
τ_e [s]	222 223		57 722	
τ_2 [s]	1 759 047		181 249	

Table 1: Constants used for the 2D cases for the primary body tides.

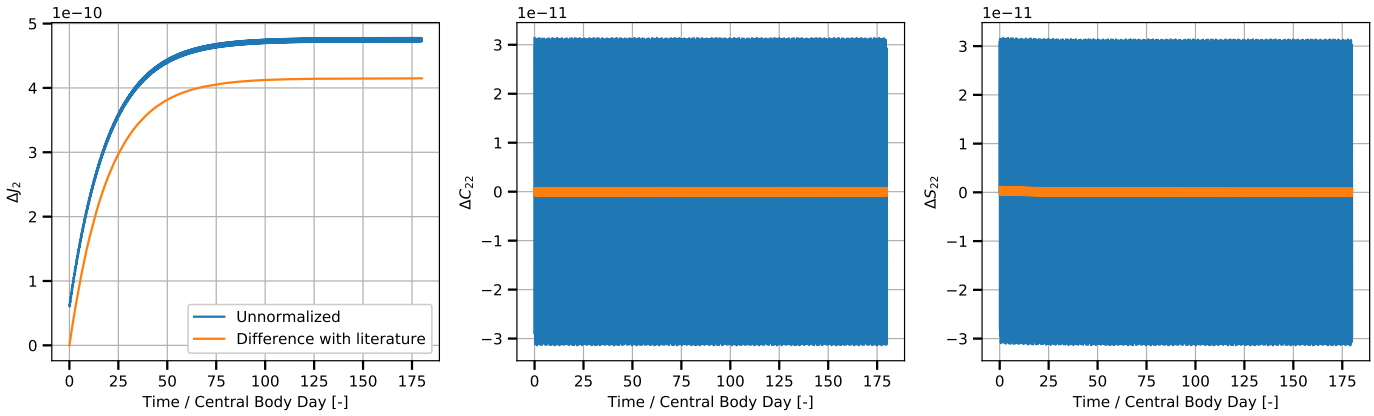

Figure 5: Tidal geopotential coefficients ΔJ_2 (left), $\Delta C_{2,2}$ (middle), and $\Delta S_{2,2}$ (right) of a coupled run of a static-gravity-field-free Mars in the Mars-Phobos system (MPhCd1). The unnormalized coefficients are compared with the values as given in literature (see Equation 51).

Variable	Mars-Phobos	Earth-Moon
r_x [m]	$9.234\,380\,91 \times 10^{6}$	$3.632\,938\,70 \times 10^{8}$
r_y [m]	$2.770\,322\,59 \times 10^{4}$	$1.089\,884\,88 \times 10^{6}$
r_z [m]	0.0	0.0
v_x [$m\,s^{-1}$]	$-6.477\,038\,45$	$-3.190\,936\,87$
v_y [$m\,s^{-1}$]	$2.169\,765\,10 \times 10^{3}$	$1.082\,419\,944\,49 \times 10^{3}$
v_z [$m\,s^{-1}$]	0.0	0.0
ω_x [$rad\,s^{-1}$]	0.0	0.0
ω_y [$rad\,s^{-1}$]	0.0	0.0
ω_z [$rad\,s^{-1}$]	$7.088\,271\,14 \times 10^{-5}$	$7.292\,123\,52 \times 10^{-5}$
q_0 [-]	1.0	1.0
q_1 [-]	0.0	0.0
q_2 [-]	0.0	0.0
q_3 [-]	0.0	0.0
ΔJ_2^{ν} [-]	0.0	0.0
$\Delta C_{2,2}^{\nu}$ [-]	0.0	0.0
$\Delta S_{2,2}^{\nu}$ [-]	0.0	0.0

Table 2: Initial conditions for both the Mars-Phobos and Earth-Moon system, where the last three lines are added for the coupled model.

The literature values for the unnormalized coefficients are obtained through Equation 51 and differences with the coupled model's coefficients are displayed in Figure 5. Only a small difference for the $\Delta C_{2,2}$ and $\Delta S_{2,2}$ is

Variable	Mars-Phobos	Earth-Moon
Semi-major axis [m]	9.376×10^{6}	$3.843\,99 \times 10^{8}$
Eccentricity [-]	0.0151	0.0549
Inclination [rad]	0.0	0.0
RAAN [rad]	0.001	0.001
Arg of perigee [rad]	0.001	0.001
True anomaly [rad]	0.001	0.001
Spin period primary [s]	88 642	86 164

Table 3: Orbital elements on which the initial state vector is based.

seen. The difference between the literature and the coupled model for the ΔJ_2 coefficient is larger, but this can be explained by the fact that the ΔJ_2^e in Equation 42 is assumed to be independent of the rotational evolution. The ΔJ_2 coefficient does not have an effect on the secular evolution of the orbit, because it causes no torque. Thus, it will not influence the results of the comparative and behavioural analysis of the coupled model.

The Earth-Moon propagation (EMoCd1), shows similar behaviour. It is damped way before the end of the propagation time, because of its short relaxation time. It exhibits a larger periodical variation after the transient damps out, because the Moon's relative mass is larger than for Phobos. The comparison with the literature coefficients from Equation 51 shows again similar results: the

	Identifier	Initial value	Damped
Mars-Phobos: Duration 0-180 Martian days, No static gravity field			
Coupled model	MPhCd1	Table 2	No
Coupled model	MPhCd2	Final state MPhCd1	Yes
Direct tidal force model (Eq 21)	MPhLy1	Final state MPhCd1	Yes
Earth-Moon: Duration 0-480 Earth days, No static gravity field			
Coupled model	EMoCd1	Table 2	No
Coupled model	EMoCd2	Final state EMoCd1	Yes
Direct tidal force model (Eq 21)	EMoLy1	Final state EMoCd1	Yes

Table 4: The simulations performed with their identifiers and input settings.

$\Delta C_{2,2}$ and $\Delta S_{2,2}$ are similar, and the ΔJ_2 coefficient shows a difference.

This proves the functionality of the coupled model for two entirely different systems. The Mars-Phobos system has a relatively small orbiting satellite which orbits faster than the rotation of the primary, while the Earth-Moon system is characterized by a relatively large satellite orbiting in a slower rate than the primary rotates.

The tidal coefficients contain information about the tidal bulge position and thus its lag, as they are describing the gravitational shape of the tidal body. The lag angle is determined through the tidal geopotential coefficients with Equation 53, while the time lag is determined with Equation 54. Figure 6 shows the variation of the tidal geometric lag angle and time lag.

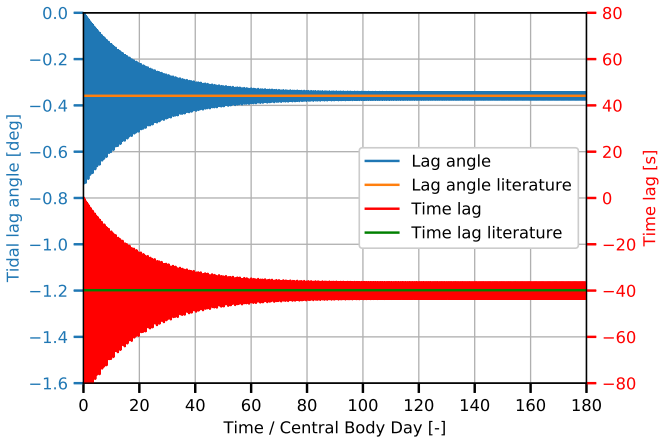

Figure 6: Tidal lag angle and time lag of a coupled run (MPhCd1) of a static-gravity-field-free Mars in the Mars-Phobos system (see Equation 53-54). Both the tidal lag angle and the time lag are compared with values obtained through literature (see Equation 20).

In Figure 6, it is clearly visible that a lag is present. It takes some time to converge to a periodically stable value. This is caused by the relaxation time settings and the behaviour of the Maxwell model. The lag's mean value is $-0.3588°$, where the negative sign shows that it really lags the position of the satellite, as expected. The lag as calculated via the Q value (see the literature approximation from Equation 20) is determined to be $-0.3585°$, which gives a difference of less than $-0.1\,\%$. The time lag's mean value of $-39.9\,\mathrm{s}$ also compares to the literature approximation ($-39.8\,\mathrm{s}$). A negative time lag follows directly from the negative lag angle and shows that the bulge in fact lags the perturber (as seen from an inertial frame).

The tidal lag angle (2.39°) and time lag (593.7 s) for the Earth correspond similarly to the literature approximations. The values are positive as the bulge's position lies now ahead of the satellite as seen in an inertial frame. An overview of the results is displayed in Table 5 in Section 6.3.

Figure 6 highlights the difference of the coupled model with the currently used direct tidal force model. The coupled model is able to reproduce variations in both the lag angle, and the time lag. In the direct tidal force model, the lag angle and time lag are assumed to be constant, through their definition from the constant quality factor in Equation 20. The figure thus displays the dynamical behaviour that cannot be fully captured by the classical direct tidal force model.

It should be noted that the literature approximation from Equation 20 and the coupled model's lag from Equation 53-54 are not completely equal. The phase lag determined by the quality factor should contain the entire phase lag: not only the angular lag of the bulge, but also the phase lag with respect to the radial tides. Efroimsky (2006) describes this phenomenon in more detail. This is not really problematic for the tides on the primary body in this section, but only becomes a factor for the tides on the locked secondary discussed in Section 7.

6.3. Orbital elements evolution

The secular changes in the semi-major axis and eccentricity seen by the coupled model are obtained as a next step. The secular changes are compared with the direct tidal force model (Eq 21) and with literature approximations (Eq 46-47). Before a comparison between the models can be made, the coupled model should be damped. To perform a meaningful comparison, the final states of the undamped coupled runs (MPhCd1, EMoCd1) are used as initial condition for the propagation of both the damped coupled model runs (MPhCd2, EMoCd2) and the direct tidal force model propagations (MPhLy1, EMoLy1).

The position and velocity state is transformed to the osculating elements at every epoch, resulting in the be-

haviour for a and e for a coupled run of the Mars-Phobos damped propagation (MPhCd2) shown in Figure 7.

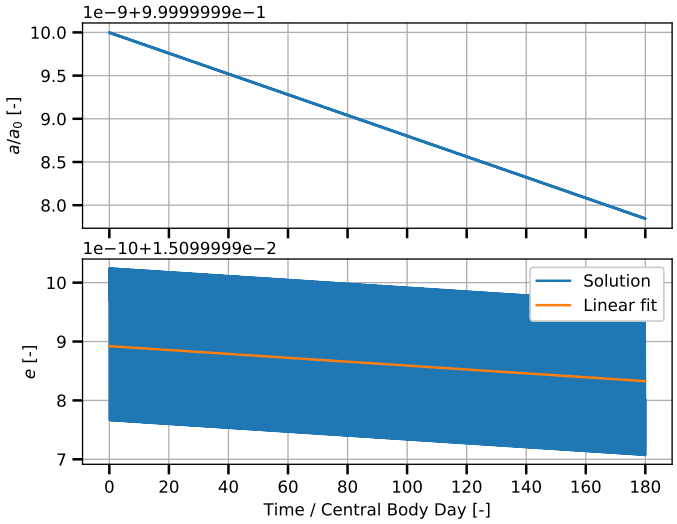

Figure 7: Main osculating elements of a damped coupled run of a static-gravity-field-free Mars in the Mars-Phobos system (MPhCd2). Both the semi-major axis (top) and eccentricity (bottom) derivative are determined by a linear fit.

The semi-major axis presents a very distinguishable slope and it does not have relatively large once-per-orbit variations. This results in a more accurately obtained secular change of $-1.265\,\mathrm{nm\,s^{-1}}$, which is only a difference of 0.2 % with the literature approximation.

The derivative is more difficult to obtain for the eccentricity as only a minor secular change is present, and it is superimposed upon large per-orbit variations. Still, a secular change can be estimated in the slowly decreasing eccentricity and a value of -1.184×10^{-10} /yr is found, which represents a difference of -22.8 % with the literature approximation. Table 5 presents an overview of the results.

The results portrayed in Table 5 show two main points. Firstly, the eccentricity evolution is difficult to determine and no clear conclusion can be drawn. This can be explained by a combination of the fact that the change in eccentricity is small, the propagation time short, and large once-per-orbit variations exist.

Secondly, the semi-major axis evolution is in accordance with the literature approximation (Equation 46), for both the direct tidal force modelling and the coupled model. The coupled model runs show a slightly lower difference with the literature. The fact that the difference with the literature is larger for the Earth-Moon case than for the Mars-Phobos case could be due to the larger eccentricity of the Moon's orbit (0.0549 for the Moon and 0.0151 for Phobos, respectively). The literature approximation in Equation 46 assumes a circular orbit for its derivation.

The semi-major axis evolution is similar for both the current direct tidal force model and the coupled model. The linear position differences must be analysed as well, to assess whether the coupled modeling could make a difference in short-time propagations for ephemeris determination. This is done by comparing the coupled runs (MPhCd2, EMoCd2) with the direct tidal force model simulations (MPhLy1, EMoLy1). After 1 central body day, the difference between the position vectors is 3 cm for the Mars-Phobos system, and only 1.5 mm for the Earth-Moon system. These values are small, but might be important for future space missions as data ranging observations become more accurate. Assuming the coupled model to lie closer to the truth, it will be beneficial to use the coupled model for these high-accurate observation missions. It will indeed provide more accurate approximations of the body's characteristics and tidal parameters. However, the direct tidal force model can still be used for the current level of accuracy.

For longer time-scales, in the order of thousands to billions of years, it would also be beneficial to switch to the coupled model. The classical direct tidal force model assumes a constant, or only a frequency dependent quality factor that averages the tidal dissipation. The coupled model is not dependent on the quality factor and time variations in the tidal dissipation are more easily captured. The input tidal parameters used in the coupled model (τ_e and τ_2), however, have to be estimated more accurately by using real data.

6.4. Varying the tidal input parameters

The runs of previous sections in Table 4 have been performed with the same constants and tidal parameters. To validate the model's scope of operation, as well as to assess its robustness, testing a wide range of input variables is necessary. The tidal input parameters for the coupled model are the Maxwell relaxation time and the global relaxation time. The Love number and the quality factor are the input for the direct tidal force model. These are linked through Equation 28 to 30. This means that varying the global relaxation time while keeping the Maxwell relaxation time constant ensures a varying k_2 over Q ratio, such that different tidal behaviour is expected.

The global relaxation times are chosen in a domain ranging from the Maxwell relaxation time to three times the true global relaxation time, as determined via the body's in literature assumed k_2 over Q ratio. More points were allocated at the beginning as the slope of the acceleration there seemed larger. The comparison is done by taking damped propagations, meaning that for every different global relaxation time, the propagation was first performed to reach a damped state. The final damped state was then used as initial condition in the damped propagation.

In Figure 8 the orbital elements changes for different global relaxation times are displayed. In Figure 9 the orbital elements changes versus the k_2 over Q ratio are shown. Figure 8 and Figure 9 show results similar to the single run comparisons. The semi-major axis evolution compares to the literature approximation from Equa-

	$\frac{da}{dt}$ [nm s^{-1}]	Diff $\frac{da}{dt}$ [%]	$\frac{de}{dt}$ [/yr]	Diff $\frac{de}{dt}$ [%]	δ [°]	Δt [s]
Mars-Phobos						
Literature (Eq 46-47 and Eq 20)	−1.263	-	-1.524×10^{-10}	-	−0.3585	−39.8
Coupled model (MPhCd1)	−1.265	0.2	-1.173×10^{-10}	−23.1	−0.3588	−39.9
Coupled model (MPhCd2)	−1.265	0.2	-1.177×10^{-10}	−22.8	−0.3588	−39.9
Direct tidal force model (MPhLy1)	−1.271	0.7	-3.410×10^{-10}	123.7	-	-
Earth-Moon						
Literature (Eq 46-47 and Eq 20)	1.184	-	1.267×10^{-11}	-	2.39	593.8
Coupled model (EMoCd1)	1.206	1.9	-5.313×10^{-12}	−141.9	2.39	593.7
Coupled model (EMoCd2)	1.207	2.0	-4.780×10^{-12}	−137.7	2.39	593.8
Direct tidal force model (EMoLy1)	1.233	4.2	1.484×10^{-11}	17.1	-	-

Table 5: Overview of the comparison of the coupled model, the direct tidal force model (see Equation 21, Lainey et al. 2007), and literature approximations of their secular effects and lag angles (Equations 46-47 and Equation 20). The percentage differences are relative to the literature values.

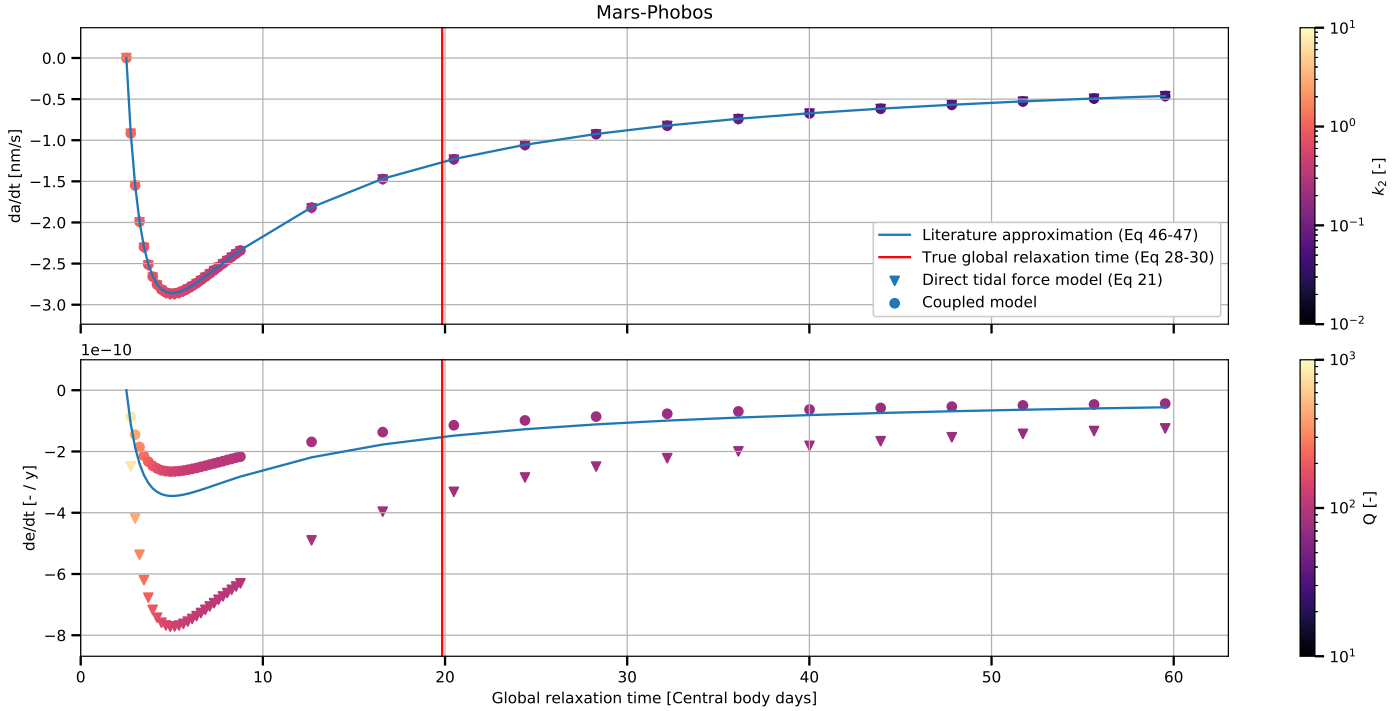

Figure 8: The orbital element changes, for semi-major axis (top) and eccentricity (bottom), for the Mars-Phobos system versus the varying global relaxation time. Models and variations used are a coupled model propagation with a constant Maxwell relaxation time of $\tau_e = 2.4$ Martian days and so varying the k_2 over Q (circle) and a direct tidal force model (Eq 21), where k_2 over Q ratios are determined backwards via Equation 30 (triangle). The literature value of the global relaxation time as in Table 1 is shown (red line), and the literature approximation of the change in orbital element (Eq 46-47) is used for comparison (blue line). The colormaps show the k_2 (top) and Q (bottom) evolution (Eq 28-30).

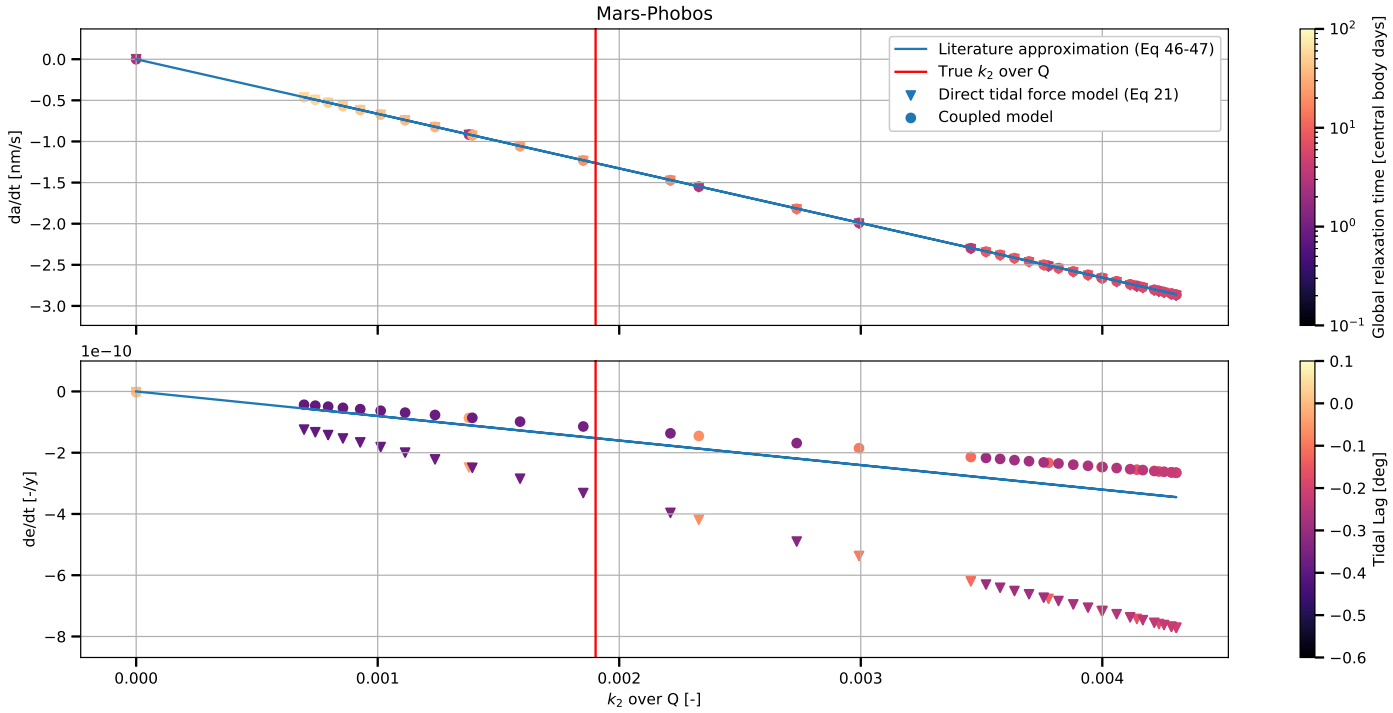

Figure 9: The orbital element changes, for semi-major axis (top) and eccentricity (bottom), for the Mars-Phobos system versus the varying k_2 over Q ratio. Models used are a coupled propagation with a constant Maxwell relaxation time of $\tau_e = 2.4$ Martian days and a varying global relaxation time (circles), and a direct tidal force model (Eq 21), where k_2 over Q ratios are determined backwards via Equation 30 (triangle). The given literature value of the k_2 over Q ratio is specified (red line), and the literature approximation of the change in orbital element (Eq 46-47) is used for comparison (blue line). The colormaps show the accompanied global relaxation time (top), and the tidal lag angle (bottom) as determined via the tidal coefficients (Eq 53) in case of the coupled model, and determined via the Q factor (Eq 20) in case of the direct tidal force model.

tion 46, and the eccentricity evolution lies further away from its approximation (Equation 47). The peculiar thing is that the difference with the literature approximation for the eccentricity evolution is for both models the same factor for all global relaxation times. An offset factor of 0.77 is obtained with the coupled model and the direct tidal force model presents an offset factor of 2.24. This results for both models in a linear evolution when comparing with the k_2 over Q variation (see Figure 9). This linear evolution is expected behaviour, as the k_2 over Q ratio linearly determines the literature approximation of the respective orbital element. Thus, the apparent difference with respect to the literature for the eccentricity change (originating from a short propagation time, large once-per-orbit variations, or small values), still shows this linear trend.

The colormaps in Figure 8 display k_2 and Q. The values for the low global relaxation time propagations (*i.e.* $\tau_2 < 5$ central body days), do not correspond to any real system. The k_2 reaches values of over 1, where the Q gets close to 1000. However, it remains interesting to see that the literature approximation of the semi-major axis evolution is followed.

The colormaps in Figure 9 show the behaviour of the global relaxation time for the varying k_2 over Q ratio, and the tidal lag angle. The lag angle for the coupled model is calculated via the respective tidal geopotential coefficients (Equation 53). For the direct tidal dissipation model it is defined via the quality factor (Equation 20). It becomes clear that both methods result in the same tidal lag angle. This means that the coupled model results in additional tidal geopotential coefficients with the exact same phase as literature predicts via the Q factor, thus partly validating the model.

The same variations in the input tidal parameters are performed for the Earth-Moon system and the orbital evolution is plotted versus the k_2 over Q parameter in Figure 10. The semi-major axis evolution shows the same behaviour as the Mars-Phobos system (*i.e.* it follows quite accurately the literature approximation and scales linearly with the k_2 over Q parameter). This differs from the eccentricity evolution. As already shown in the single runs for the Earth-Moon system (see Table 5), the eccentricity evolution becomes negative, while literature would presume a positive value. In Figure 10, the eccentricity change becomes negative for a higher lag angle, which means for a lower Q value and lower corresponding k_2 value. A lower k_2 means a lower amplitude of the tidal bulge. Therefore, if the lag angle is larger, the dissipation and thus the change in eccentricity should be an approximation to the literature.

The origin of this eccentricity evolution difference between the coupled model and direct tidal force model and literature is not found yet, and is an interesting topic for further research. It could relate to the very small eccentricity change and the resulting difficulty of retrieving this value, as the semi-major axis is comparable to the literature. This is the reason that the semi-major axis change observations are used in approximating the tidal parameters and not the less accurate eccentricity evolution.

7. Application: Tides on the secondary

The second test case discussed is the tides on the less massive and locked secondary body. These can be as important as the tides on the primary, and above that are more difficult to calculate correctly. This is demonstrated by the fact that still a discussion is held in recent literature papers about the approximation of the semi-major axis evolution caused by the satellite tides (see Section 5). They differ with a factor 57/21. Both approximations are considered in this research.

Then, the librational tides as discussed in Section 3 and Section 5 could contribute a larger amount to the tidal dissipation, and dealing with these tides is in current literature proposed in an averaged way and relies on multiple assumptions. The coupled model should automatically incorporate the tidal behaviour accompanied with the librations. This is why the coupled model could benefit most for these secondary body tides, and why testing these systems is more than appropriate.

7.1. Setup and input parameters

The constants used for this part of the research are depicted in Table 6. The classical tidal parameters k_2 and Q of Phobos are not very accurately known. In Le Maistre et al. (2013), a range of possible values is used to determine characteristics of Phobos. Possible values of $k_2 = 0.002$ and $Q = 100.0$ lead to a Maxwell relaxation time (via Equation 28-30) of $\tau_e = 438\,184\,\mathrm{s} = 5.07\,\mathrm{d}$ and a high global relaxation time of $\tau_2 = 3.940\,154\,00 \times 10^8\,\mathrm{s} = 4560.4\,\mathrm{d}$. This means that for the same propagation time of 120 Martian days, the equilibrium value for the coefficients is not reached yet, and no (periodic) convergence should be expected. Furthermore, the k_2 over Q value is smaller than for Mars, so the effect of the tides will be less visible in the results. The above reasons justify the use of different tidal parameters for Phobos, and the k_2 and Q of the Moon are taken.

The initial state vector is based on the same orbital elements as in Table 3 disregarding the slight offset given for the right ascension of the ascending node, argument of perigee and true anomaly. These are set at zero now. Because a locked body is assumed, no need for an additional spin period is necessary, and the initial rotation vector of the tidal body will be put equal or close to the mean motion of the system as determined via the semi-major axis value. To put the system in a reference frame at the less massive body, the negative of the Cartesian state is taken, and the initial position of the x-axis of the rotating reference frame is put in the direction of the more massive body, so in the opposite direction as the inertial frame. The initial ΔJ_2^ν and $\Delta C_{2,2}^\nu$ are given a value close to their

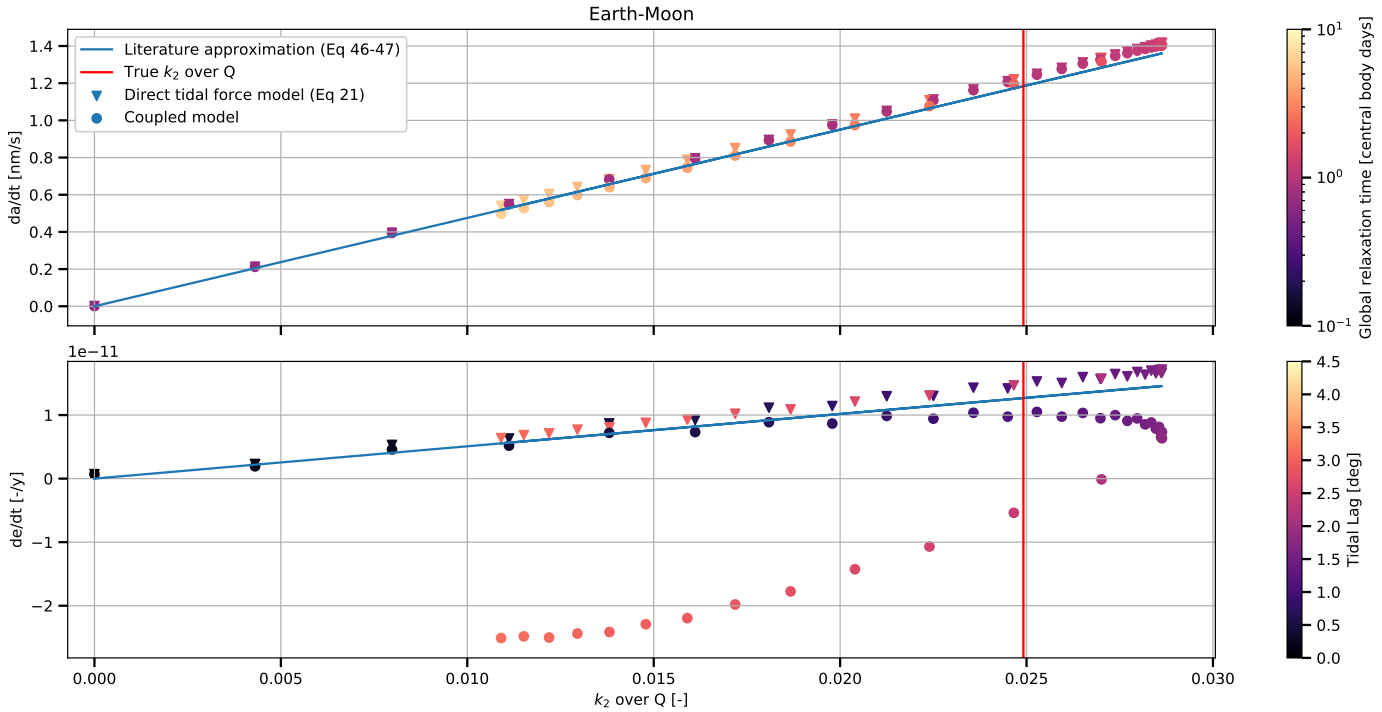

Figure 10: The orbital element changes, for semi-major axis (top) and eccentricity (bottom), for the Earth-Moon system versus the varying k_2 over Q ratio. Models used are a coupled propagation with a constant Maxwell relaxation time of $\tau_e = 0.67$ days and a varying global relaxation time (circles), and a direct tidal force model (Eq 21), where k_2 over Q ratios are determined backwards via Equation 30 (triangle). The given literature value of the k_2 over Q ratio is specified (red line), and the literature approximation of the change in orbital element (Eq 46-47) is used for comparison (blue line). The colormaps show the accompanied global relaxation time (top), and the tidal lag angle (bottom) as determined via the tidal coefficients (Eq 53) in case of the coupled model, and determined via the Q factor (Eq 20) in case of the direct tidal force model.

Constant	**Phobos-Mars**	**Source**	**Moon-Earth**	**Source**
G [$m^3\,kg^{-1}\,s^{-2}$]	$6.674\,08 \times 10^{-11}$	CODATA 2014	$6.674\,08 \times 10^{-11}$	CODATA 2014
M_c [kg]	1.0659×10^{16}	Wiki	7.342×10^{22}	IAU 2015 Resolution B 3
M_s [kg]	6.4171×10^{23}	Wiki	$5.972\,364\,730\,419 \times 10^{24}$	Wiki
R_E [m]	12.22×10^{3}	Le Maistre et al. (2013)	1737.4×10^{3}	Wiki
ξ [-]	0.43013	Willner et al. (2010)	0.394	Wiki
k_2 [-]	0.024 059	-	0.024 059	Lainey (2016)
Q [-]	37.5	-	37.5	Lainey (2016)
τ_e [s]	162 251	-	$1.383\,086\,7 \times 10^{7}$	-
τ_2 [s]	$1.213\,200\,9 \times 10^{7}$	-	$8.306\,058\,05 \times 10^{8}$	-

Table 6: Constants used for the 2D cases for the secondary body tides.

convergence. This leads to the initial state vector stated in Table 7.

Variable	Phobos-Mars	Moon-Earth
r_x [m]	$-9.234\,422\,4 \times 10^6$	$3.632\,954\,949 \times 10^8$
r_y [m]	0.0	0.0
r_z [m]	0.0	0.0
v_x [m s^{-1}]	0.0	0.0
v_y [m s^{-1}]	$-2169.774\,78$	$1082.424\,67$
v_z [m s^{-1}]	0.0	0.0
ω_x [rad s^{-1}]	0.0	0.0
ω_y [rad s^{-1}]	0.0	0.0
ω_z [rad s^{-1}]	$2.279\,495\,36 \times 10^{-4}$	$2.665\,315\,78 \times 10^{-6}$
q_0 [-]	0.0	0.0
q_1 [-]	0.0	0.0
q_2 [-]	0.0	0.0
q_3 [-]	1.0	1.0
ΔJ_2^ν [-]	0.12	0.0
$\Delta C_{2,2}^\nu$ [-]	0.06	0.0
$\Delta S_{2,2}^\nu$ [-]	0.0	0.0

Table 7: Initial conditions for both the Phobos-Mars and Moon-Earth system, where the last three lines are added for the coupled model.

Table 8 states the propagations performed. The duration of the simulations varies per situation. The undamped coupled runs need to converge, and because of the large global relaxation times (*i.e.* $\tau_2 = 440.3$ Phobos days and $\tau_2 = 351.9$ Lunar days) large propagations are necessary. For the Phobos-Mars system a duration of 10000 Phobos days is chosen and for the Moon-Earth system a duration of 8000 Lunar days.

The comparison with the current tidal force models (Equation 21 and Equation 25) is performed again after convergence of the coupled model's transient. Final state variables from the coupled model propagations are used as initial condition for the comparison runs. In this way, the coupled model and direct tidal force models are compared consistently. The comparison will be done in Section 7.3.

7.2. Tidal coefficients

The tidal coefficients for the Phobos-Mars system propagation (PhMCd1) are plotted in Figure 11. The coefficients show convergence as expected, because the relaxation times are surpassed. In comparison with the tides on the primary, now also the $\Delta C_{2,2}$ displays a non-zero mean value, and a proper comparison with the literature approximation (Equation 51) becomes inept. The $\Delta S_{2,2}$ coefficient compares to the literature approximation.

Because the coefficients are relatively large, see the difference with Figure 5, the change in the coefficients starts to have an effect on the moment of inertia of Phobos. The moment of inertia show extreme values according to Equation 57 (*i.e.* $A = 0.271$, $B = 0.509$, $C = 0.510$) . This immediately shows that the current modelling does not represent the true Phobos, because assumed moments of inertia in literature ($A = 0.3615$, $B = 0.4265$, and $C = 0.5024$ Willner et al. 2010) do not correspond. However, that does not matter for the analysis of the coupled model. It does mean, however, that the principal moment of inertia C will change, and the middle term in Equation 8 of the rotational evolution had to be used.

The tidal coefficients for the Moon are similar qua behaviour, but not qua size. Also the ΔJ_2 converges, but only towards a value of 5.5×10^{-6}. $\Delta C_{2,2}$ converges towards 2.8×10^{-6}. $\Delta S_{2,2}$ oscillates around zero and compares to the theoretical approximation.

The tidal lag for both Phobos and the Moon show variations around a zero mean value, because the angle between the bulge's position and the perturber now varies along the orbit. The variations state the librational tides.

7.3. Librations and the evolution of the orbital elements

Until now, the longitudinal librations as discussed in Section 5.3 have not been determined. The librations for the primary body are practically non-existent. The librations on the locked secondary, however, could be much larger and be a cause for a large additional dissipation inside the body.

The librations for a propagation with a short (PhMCd2) and longer (PhMCd3) duration are displayed in Figure 12. The libration angle for the short time-scale propagation (in the bottom plot of Figure 12) varies with a constant rate around a zero mean value. The amplitude takes a value of 6.1°, which is confirmed by a theoretical value of 6.0° as determined via Equation 58. Note that these values do not compare with the true libration amplitude for Phobos (1.1° Willner et al. 2010). That is caused by the fact that the moment of inertia for Phobos portray different values as well.

The libration angle for the long time-scale propagation in the top plot of Figure 12 displays an amplitude of 6.2°, but the libration also seems to be oscillating with another large period. This is the effect of the long term variation of the rotation angle, which is confirmed by literature in for example Rambaux et al. (2012).

The librations shown are truly damped and only consist of a forced variant. A Fourier transform of the libration angle of both the undamped (PhMCd1) and damped (PhMCd2) propagation are displayed in Figure 13 to confirm this. The Fourier transform of the undamped propagation displays many free librations with varying periods. The free libration with the highest amplitude is found at a period of 0.84 of the orbiting period of Phobos, which corresponds to the literature approximation of Equation 56.

The damped propagation in Figure 13 does not have a peak at that period, and instead only shows peaks at Phobos' orbiting period and its main harmonics. The peak at the orbiting period displays a value of 6.1° which confirms the previously obtained libration amplitude.

The libration amplitude for the Moon is considerably smaller than for Phobos. A value of 0.0005° is obtained.

	Identifier	Initial value	Damped	Duration
Phobos-Mars				
Coupled model	PhMCd1	Table 7	No	10000 Phobos days
Coupled model	PhMCd2	Final state PhMCd1	Yes	360 Phobos days
Coupled model	PhMCd3	Final state PhMCd1	Yes	90000 Phobos days
Direct tidal force model (Eq 21)	PhMLy1	Final state PhMCd1	Yes	360 Phobos days
Averaged direct tidal force model (Eq 25)	PhMLa1	Final state PhMCd1	Yes	360 Phobos days
Moon-Earth				
Coupled model	MoECd1	Table 7	No	8000 Lunar days
Coupled model	MoECd2	Final state MoECd1	Yes	360 Lunar days
Direct tidal force model (Eq 21)	MoELy1	Final state MoECd1	Yes	360 Lunar days
Averaged direct tidal force model (Eq 21)	MoELa1	Final state MoECd1	Yes	360 Lunar days

Table 8: The simulations performed with their identifiers and input settings for the propagations with tides on the secondary.

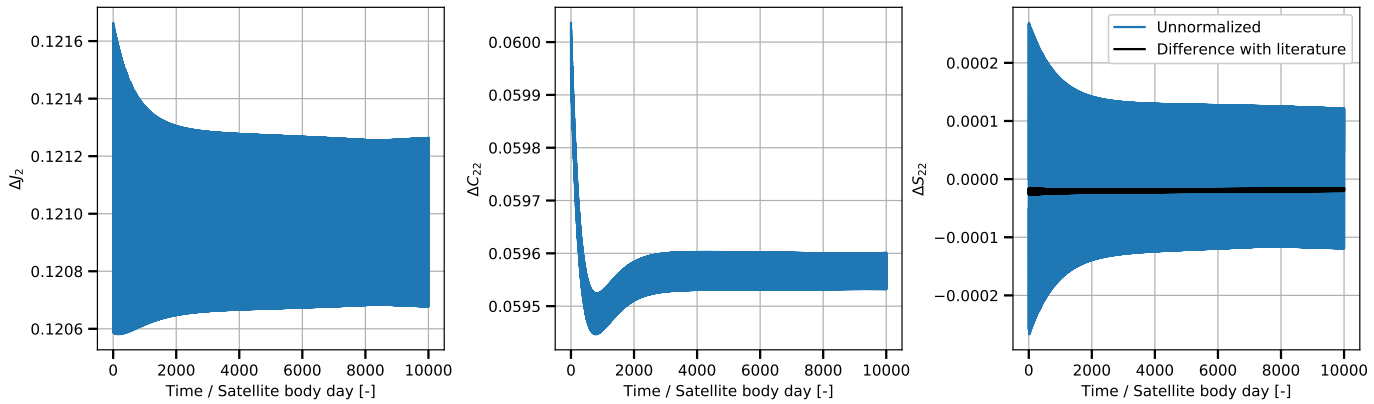

Figure 11: Tidal geopotential coefficients ΔJ_2 (left), $\Delta C_{2,2}$ (middle), and $\Delta S_{2,2}$ (right) of a coupled run of a static-gravity-field-free Phobos in the Phobos-Mars system (MPhCd1). The unnormalized coefficients are compared with the values as given in literature (see Equation 51).

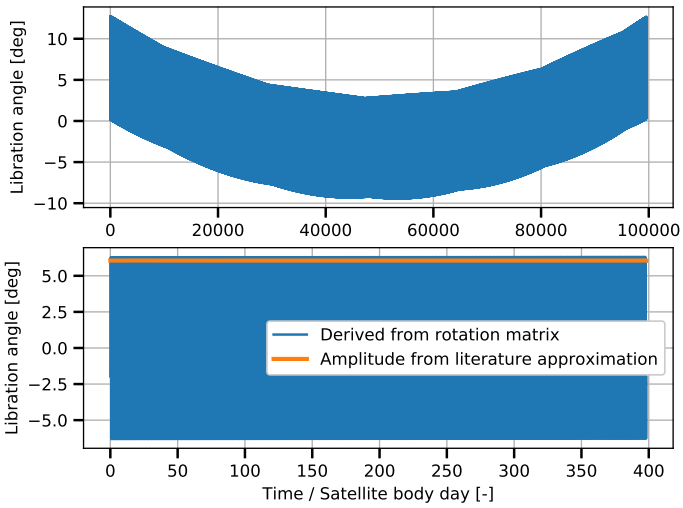

Figure 12: Libration angle for a longer (top) and shorter (bottom) time-scale of coupled model's propagations of the Phobos-Mars system (PhMCd3 and PhMCd2 respectively). The libration amplitudes are compared with a literature approximation (Eq 58).

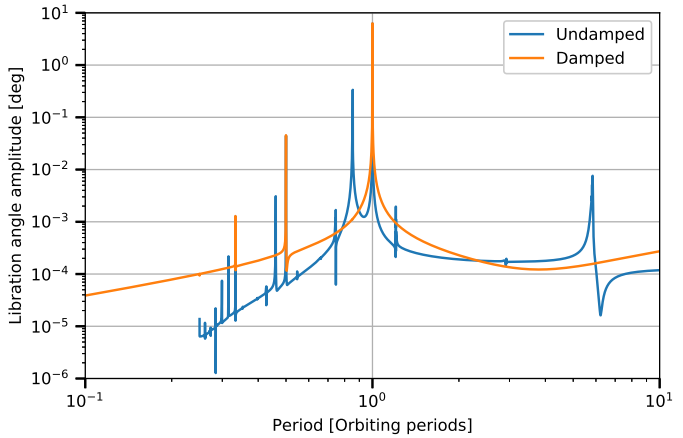

Figure 13: Fourier transform of the libration angle of Phobos for the undamped (PhMCd1) and damped (PhMCd2) propagations of the Phobos-Mars system.

Also this value is completely damped and compares to the literature approximation of Equation 58.

These librations cause additional dissipation due to the friction inside the body. As discussed in Section 5.3, Efroimsky (2018) stated the difference in tidal dissipation when also regarding these physical librational tides. Via Equation 61 an increase factor of 11.3 is obtained (corresponding to the libration angle of 6.1°) . This results in increased semi-major axis and eccentricity evolution with the same factor, under assumption of an orbital energy change that is much larger than the rotational energy change.

The orbital elements are determined for the propagations of the damped coupled model run (PhMCd2), the direct tidal force model run from Equation 21 (PhMLy1), and the averaged direct tidal force model propagation from Equation 25 (PhMLa1). The overview of the evolution of the orbital elements is shown in Table 9.

The coupled model displays a large offset with the literature for the Phobos-Mars system (PhMCd2). This can be fully described by the librations, as the factor for the additional dissipation (11.7) is larger than the relative difference with the literature. When no librations are present (MoECd2), the coupled model follows roughly the literature. The difference is probably relatively high (8.5 %), because the secular evolution values become small for the Moon-Earth system.

The libration amplitudes are determined for the coupled model and they correspond with the approximations from Willner et al. (2010) as stated in Equation 58. For smaller moment of inertia, and smaller libration amplitudes, the literature approximation from Efroimsky (2018) as in Equation 59, becomes similar to Equation 58.

The direct tidal force model (PhMLy1, MoELy1) does not follow the original literature approximation for the semi-major axis evolution. In the Phobos-Mars case, it seems to explode to a value which is too large. This could be because the model has no static field, while the coupled model is converged towards a variation around a static tidal coefficient. Thus the initial condition for the direct tidal force model could be off. The propagation for the Moon-Earth (MoELy1) corresponds more closely to the literature approximation 2, as stated in Boué (2019).

The averaged direct tidal dissipation simulations (PhMLa1, MoELa1) correspond to the original literature approximation.

7.4. Varying the tidal input parameters

To further investigate the meaning of the single runs, the tidal input parameters τ_e, τ_2 (and thus k_2 and Q) are varied again and multiple propagations are performed. The global relaxation times are chosen in a domain ranging from the Maxwell relaxation time to two times the true global relaxation time, as determined via the body's in literature assumed k_2 and Q. The comparison is done by taking damped propagations, meaning that for every different global relaxation time, the propagation was first performed to reach a damped state. The final damped state was then used as initial condition in the damped propagation.

The three propagations performed include a propagation of the coupled model, a propagation of the direct tidal force model from (Equation 21), and a propagation of the averaged direct tidal force model (Equation 25). All are run without a static field. The change in semi-major axis and eccentricity versus the global relaxation time for the Phobos-Mars system are displayed in Figure 14.

The figure displays several orders of difference in both the semi-major axis and the eccentricity change between the coupled run and the other propagations. This could very well be explained by the additional dissipation caused

	$\frac{da}{dt}$ [nm s^{-1}]	Diff $\frac{da}{dt}$ [%]	$\frac{de}{dt}$ [/yr]	Diff $\frac{de}{dt}$ [%]	θ_τ [°]	$\frac{\langle P\rangle^{(\mathrm{lib})}_{\mathrm{tide}}}{\langle P\rangle^{(\mathrm{main})}_{\mathrm{tide}}}$ [-]
Phobos-Mars						
Literature 1	−1.486	-	-1.656×10^{-7}	-	−6.0	11.0
Literature 2	−4.032	-	-1.656×10^{-7}	-	−2.4	2.7
(PhMCd1)	−6.050	307	-7.298×10^{-7}	341	−6.1	11.3
(PhMCd2)	−5.802	291	-7.358×10^{-7}	344	−6.3	11.7
(PhMCd3)	−6.023	307	-7.280×10^{-7}	340	−6.2	11.4
(PhMLy1)	102.7	−7015	-1.514×10^{-7}	−8.6	-	-
(PhMLa1)	−1.490	0.3	-1.661×10^{-7}	0.3	-	-
Moon-Earth						
Literature 1	−0.006 38	-	-4.773×10^{-12}	-	-4.9×10^{-4}	9.0×10^{-5}
Literature 2	−0.0173	-	-4.773×10^{-12}	-	-4.9×10^{-4}	9.0×10^{-5}
(MoECd1)	−0.006 95	8.9	-4.854×10^{-12}	1.7	-4.0×10^{-4}	8.2×10^{-5}
(MoECd2)	−0.006 93	8.5	-4.854×10^{-12}	1.7	-5.0×10^{-4}	9.0×10^{-5}
(MoELy1)	−0.0184	188	-5.0691×10^{-12}	6.2	-	-
(MoELa1)	−0.007 038	10.3	-4.9834×10^{-12}	4.4	-	-

Table 9: Overview of the comparison of simulations with tides on the secondary for the coupled model, the direct tidal force model (Eq 21, Lainey et al. 2007), the averaged direct tidal force model (Eq 25, Lari 2018), and literature approximations of their secular effects (Eq 48-50) and libration amplitude (Eq 58-59). Literature approximation 1 are from (Eq 48, Eq 50 and Eq 58), and literature approximation 2 are from (Eq 49, Eq 50 and Eq 59). The percentage differences are relative to the upper literature approximations 1. The last column denotes the additional tidal dissipation factor due to the libration.

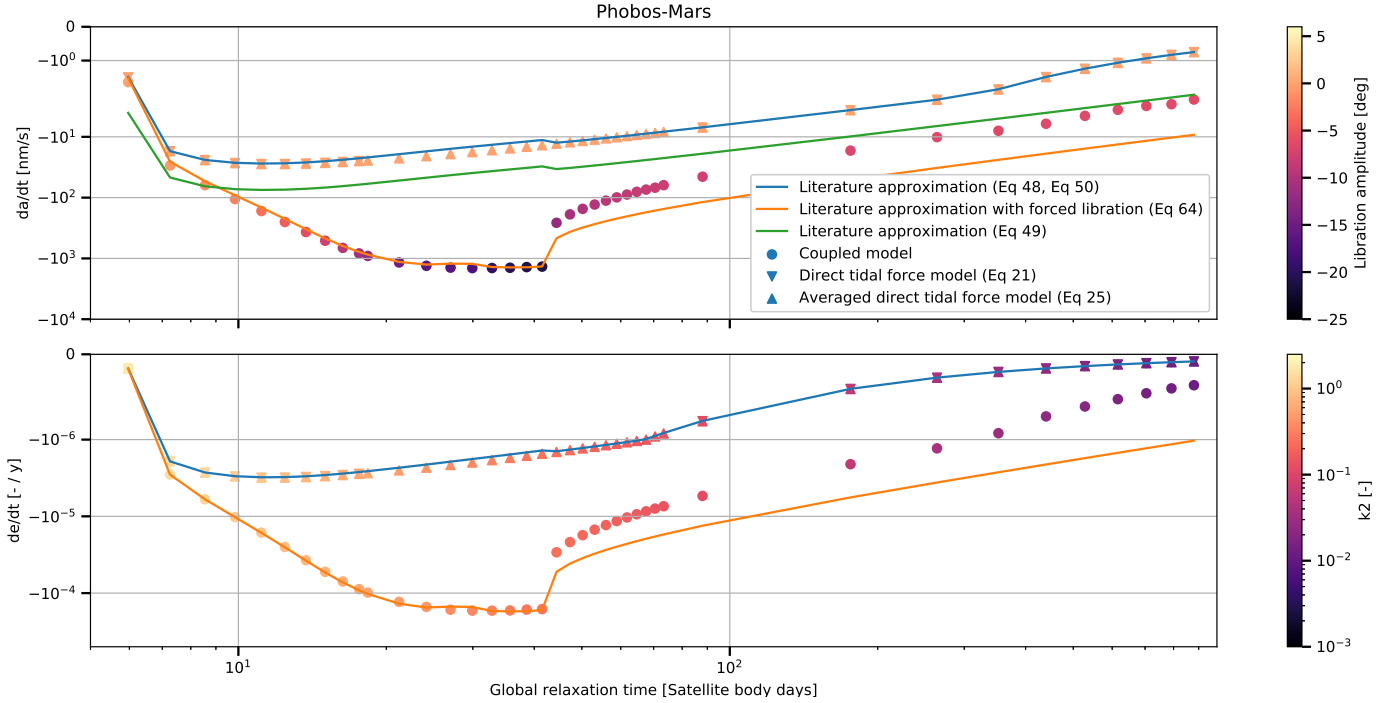

Figure 14: The orbital element changes, for semi-major axis (top), and eccentricity (bottom), of the Phobos-Mars system versus the varying global relaxation time. Models and variations used are a coupled propagation with a constant Maxwell relaxation time of $\tau_e = 58.9$ Phobos days (circle), a direct tidal force model (Eq 21, Lainey et al. 2007) (triangle down), and an averaged direct tidal force model (Eq 25, Lari 2018) (triangle up). The accompanied value of the k_2 over Q ratio results in a literature value as presented in Souchay et al. (2013) (Eq 48) (blue line), or as determined in Boué (2019) (Eq 49) (green line). The literature approximation including the librational dissipation is shown (Eq 64) (orange line). The colormaps show the libration angle as determined via the rotation angle and k_2.

by the physical libration (Equation 64), as that literature value corresponds for lower global relaxation times very well with the coupled model. The fact that for higher global relaxation times the coupled model and the literature value with libration start to differ, can be caused by the incorrect libration amplitude estimation for those relaxation times. Using the libration amplitude from the literature value of Efroimsky (2018), Equation 59, to calculate the additional dissipation due to the librations, better estimates for the semi-major axis and eccentricity derivative are retrieved.

Figure 15 displays the secular effects for the Moon-Earth case. The Maxwell relaxation time is set at 13 830 267 s and the global relaxation times are varied. The propagations are run for 180 rotation periods of the secondary, and as the Moon rotates in 27 days, this remains a large period.

The Moon does not have a large libration (see Table 9) and the relatively large secular effects for the Phobos-Mars system are not displayed. The coupled model follows the literature approximation for both the semi-major axis and the eccentricity evolution.

The other main observation is the difference between the direct tidal force methods. The averaged direct tidal force model (Equation 25) follows the literature approximation for the evolution of the semi-major axis as given by Souchay et al. (2013) (Equation 48), but the direct tidal force model stated in Lainey et al. (2007) (Equation 21), clearly stays with the literature approximation as stated in Boué (2019) (Equation 49). This is a remarkable effect as both models relate to each other, and are in fact used by both authors. The only difference between the models is the averaging of the spin rate, and the fact that the averaged direct tidal force generates no torque. It only has a radial part. The exact cause of the difference remains unknown.

It is difficult to state which literature approximation stays closest to the truth. Assuming the coupled model to be generally better and more consistent, the semi-major axis evolution of Equation 48 is regarded to lie closer to reality. The coupled model follows that original literature approximation in the Moon-Earth case perfectly. On top of that, that literature approximation with additional libration dissipation factor (Equation 64) stays close to the coupled model for a certain range of global relaxation times in the Phobos-Mars system.

Overall, the librational effect is easily incorporated. The coupled model shows an effect whenever a large libration is present, and can also be easily incorporated for no libration. This all has been shown for relatively short term propagations, which are important for future space missions and accurate ephemeris determination. The only negative part of the coupled model is that a damped initial condition has to be found before real situations can be portrayed. With the possible high relaxation times, this search can become quite cumbersome. However, the coupled model displays better behaviour. The current day models show more varying behaviour and do not deal with these librations automatically and do so differently. Thus, it would be beneficial to use the coupled model in ephemeris determination of satellites with librations.

8. Conclusion

From the research a couple conclusions can be drawn. First, the systems with tides on the more massive body are regarded (Section 6). The results show a clear picture: The evolution of the semi-major axis determined by the coupled model is similar to the current methods for tidal effects and similar to the literature approximation of this evolution. For a range of input parameters varying the relaxation times of the coupled model, and in so on varying the currently used tidal parameters k_2 and Q, all changes in semi-major axis seem to correspond to literature and current direct tidal force modeling methods (Figure 8-10).

The eccentricity change is more difficult to determine, as it is in order of magnitude closer to the step error of the propagation, and shows a difference with the literature approximation (Figure 10). However, this occurs for both the current models and the newly tested coupled model, and so on can be valued with less importance. The exact reason for this discrepancy is yet to be determined, but it could be because only a minor secular change is present, and it is superimposed upon large per-orbit variations.

The tidal coefficients determined in the coupled model lead to a lag angle and time lag that correspond to the theory for every case (Table 5), and the amplitude of the tidal coefficients that govern the lag angle seems to resemble literature values. In these varying lag angle and time lag, the coupled model displays behaviour which is by definition not captured by the classical direct tidal force models.

The linear position differences between the current direct tidal force model and the coupled model are small (3 cm for the Phobos-Mars system, and 1.5 mm for the Earth-Moon system after one day of propagation). However, they might become important for future space missions as data ranging observations become more accurate.

The second part of the research is performed on a system with the tides on the locked secondary. Especially for the system Phobos-Mars, with the tides on Phobos, a coupled model behaves differently than all current models. Phobos exhibits a large physical libration, which causes an additional dissipation that can become the largest factor in the overall tidal dissipation. The additional dissipation results in a faster evolution of both the semi-major axis as the eccentricity. This effect is only captured by the coupled model, and not by the currently used models.

The Moon-Earth case, with the tides on the Moon, does not have these librations, and evolution values lie closer. The coupled model follows the literature approximation (Equation 48). The scientific community is not sure which is the correct literature approximation, and as

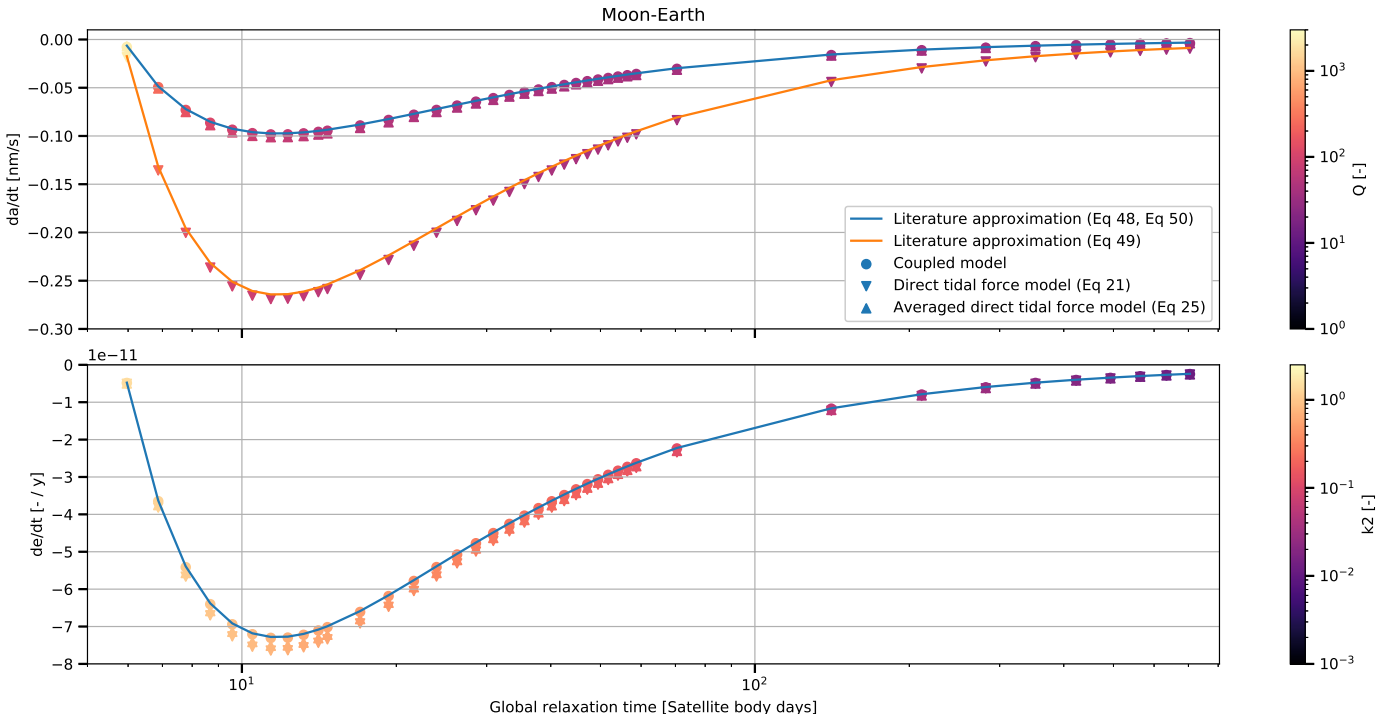

Figure 15: The orbital element changes, for semi-major axis (top), and eccentricity (bottom), of the Moon-Earth system versus the varying global relaxation time. Models and variations used are a coupled propagation with a constant Maxwell relaxation time of $\tau_e = 5.42$ Lunar days (circle), a direct tidal force model (Eq 21, Lainey et al. 2007) (triangle down), and an averaged direct tidal force model (Eq 25, Lari 2018) (triangle up). The accompanied value of the k_2 over Q ratio results in a literature value as presented in Souchay et al. (2013) (Eq 48) (blue line), or as determined in Boué (2019) (Eq 49) (green line). The colormaps display the k_2 and Q values.

well the classical direct tidal force models show different behaviour for the change in semi-major axis. Following the coupled model's behaviour, only a single literature approximation should be assumed correct (Souchay et al. 2013).

Overall, the coupled model behaves exactly as it should for a variation of tidal input parameters. These input parameters have yet to be determined accurately for most solar system bodies, which could be done in further studies involving real position data. For short timescales, currently used methods or literature approximations can still be used whenever data requirements are not high. However, when dealing with high accuracy observations, and for bodies with larger physical librations, it rewards to switch to a coupled method. It takes properly into account the frequency dependency and possible variation of classical tidal parameters are caught. The method is also valid for larger eccentricities and inclinations, and remains valid for any orientation and spin rate. Furthermore, it is able to capture the behaviour of secondary bodies with large physical librations.

References

Ashenberg, J. (2005). Proposed method for modeling the gravitational interaction between finite bodies. *Journal of Guidance, Control, and Dynamics*, 28(4):768–774.

Borderies, N. (1978). Mutual gravitational potential of n solid bodies. *Celestial Mechanics*, 18(3):295–307.

Boue, G., Correia, A. C. M., and Laskar, J. (2016). Complete spin and orbital evolution of close-in bodies using a maxwell viscoelastic rheology. *Celestial Mechanics & Dynamical Astronomy*, 126(1-3):31–60.

Boué, G. (2019). Tidal evolution of the keplerian elements. *Celestial Mechanics and Dynamical Astronomy*, 131(7).

Correia, A. C. M., Boue, G., Laskar, J., and Rodriguez, A. (2014). Deformation and tidal evolution of close-in planets and satellites using a maxwell viscoelastic rheology. *Astronomy & Astrophysics*, 571.

Correia, A. C. M. and Rodríguez, A. (2013). On the equilibrium figure of close-in planets and satellites. *The Astrophysical Journal*, 767(2):128.

Darwin, G. H. (1880). On the Secular Changes in the Elements of the Orbit of a Satellite Revolving about a Tidally Distorted Planet. *Philosophical Transactions of the Royal Society of London Series I*, 171:713–891.

Darwin, G. H. and Glaisher, J. W. L. (1879). Xiii. on the precession of a viscous spheroid, and on the remote history of the earth. *Philosophical Transactions of the Royal Society of London*, 170:447–538.

Dehant, V., Park, R., Dirkx, D., Iess, L., Neumann, G., Turyshev, S., and Van Hoolst, T. (2017). Survey of capabilities and applications of accurate clocks: Directions for planetary science. *Space Science Reviews*, 212(3-4):1433–1451.

Dirkx, D., Lainey, V., Gurvits, L. I., and Visser, P. N. A. M. (2016). Dynamical modelling of the galilean moons for the juice mission. *Planetary and Space Science*, 134:82–95.

Dirkx, D., Mooij, E., and Root, B. (2019). Propagation and estimation of the dynamical behaviour of gravitationally interacting rigid bodies. *Astrophysics and Space Science*, 364(2).

Efroimsky, M. (2006). The theory of bodily tides. the models and the physics.

Efroimsky, M. (2012). Bodily tides near spin-orbit resonances. *Celestial Mechanics & Dynamical Astronomy*, 112(3):283–330.

Efroimsky, M. (2018). Dissipation in a tidally perturbed body librating in longitude. *Icarus*, 306:328–354.

Efroimsky, M. and Lainey, V. (2007). Physics of bodily tides in terrestrial planets and the appropriate scales of dynamical evolution. *Journal of Geophysical Research*, 112(E12).

Efroimsky, M. and Makarov, V. V. (2013). Tidal friction and tidal lagging. applicability limitations of a popular formula for the tidal torque. *The Astrophysical Journal*, 764(1).

Efroimsky, M. and Williams, J. G. (2009). Tidal torques: a critical review of some techniques. *Celestial Mechanics & Dynamical Astronomy*, 104(3):257–289.

Fahnestock, E. G. and Scheeres, D. J. (2006). Simulation of the full two rigid body problem using polyhedral mutual potential and potential derivatives approach. *Celestial Mechanics & Dynamical Astronomy*, 96(3-4):317–339.

Ferraz-Mello, S. (2013). Tidal synchronization of close-in satellites and exoplanets. a rheophysical approach. *Celestial Mechanics & Dynamical Astronomy*, 116(2):109–140.

Ferraz-Mello, S. (2015). The small and large lags of the elastic and anelastic tides the virtual identity of two rheophysical theories. *Astronomy & Astrophysics*, 579.

Folkner, W., Williams, J., Boggs, D., Park, R., and Kuchynka, P. (2014). The planetary and lunar ephemerides de430 and de431. *Interplanetary Network Progress Report*, 196.

Fukushima, T. (2008). Simple, regular, and efficient numerical integration of rotational motion. *Astronomical Journal*, 135(6):2298–2322.

Galilei, G. and Van Helden, A. (1989). *Sidereus nuncius, or, The Sidereal messenger*. University of Chicago Press, Chicago.

Genova, A., Goossens, S., Lemoine, F. G., Mazarico, E., Neumann, G. A., Smith, D. E., and Zuber, M. T. (2016). Seasonal and static gravity field of mars from mgs, mars odyssey and mro radio science. *Icarus*, 272:228–245.

Goldreich, P. (1963). On the eccentricity of satellite orbits in the solar system. *Monthly Notices of the Royal Astronomical Society*, 126(3):257–268.

Goldreich, P. and Peale, S. (1966). Spin-orbit coupling in solar system. *Astronomical Journal*, 71(6):425.

Goldreich, P. and Soter, S. (1966). Q in solar system. *Icarus*, 5(4):375.

Hairer, E., Nørsett, S. P., and Wanner, G. (2009). *Solving ordinary differential equations I : nonstiff problems*. Springer series in computational mathematics,. Springer, Heidelberg ; London, 2nd rev. edition.

Jeffreys, H. (1976). *The earth : its origin, history, and physical constitution*. Cambridge University Press, Cambridge Eng. ; New York, 6th edition.

Kant, I. (1754). *Kant's Cosmonogy: as in his Essay on the Retardation of the Rotation of the Earth, and his Natural History and Theory of the Heavens.*

Kaula, W. M. (1964). Tidal dissipation by solid friction and the resulting orbital evolution. *Reviews of Geophysics*, 2(4):661–685.

Kikuchi, F., Liu, Q., Hanada, H., Kawano, N., Matsumoto, K., Iwata, T., Goossens, S., Asari, K., Ishihara, Y., Tsuruta, S., Ishikawa, T., Noda, H., Namiki, N., Petrova, N., Harada, Y., Ping, J., and Sasaki, S. (2009). Picosecond accuracy vlbi of the two subsatellites of selene (kaguya) using multifrequency and same beam methods. *Radio Science*, 44(2).

Lainey, V. (2016). Quantification of tidal parameters from solar system data. *Celestial Mechanics & Dynamical Astronomy*, 126(1-3):145–156.

Lainey, V., Arlot, J. E., Karatekin, O., and Van Hoolst, T. (2009). Strong tidal dissipation in io and jupiter from astrometric observations. *Nature*, 459(7249):957–959.

Lainey, V., Casajus, L. G., Fuller, J., Zannoni, M., Tortora, P., Cooper, N., Murray, C., Modenini, D., Park, R. S., Robert, V., et al. (2020). Resonance locking in giant planets indicated by the rapid orbital expansion of titan. *Nature Astronomy*, pages 1–6.

Lainey, V., Dehant, V., and Pätzold, M. (2007). First numerical ephemerides of the martian moons. *Astronomy & Astrophysics*, 465(3):1075–1084.

Lainey, V., Duriez, L., and Vienne, A. (2004). New accurate ephemerides for the galilean satellites of jupiter. *Astronomy & Astrophysics*, 420(3):1171–1183.

Lainey, V., Karatekin, O., Desmars, J., Charnoz, S., Arlot, J. E., Emelyanov, N., Le Poncin-Lafitte, C., Mathis, S., Remus, F., Tobie, G., and Zahn, J. P. (2012). Strong tidal dissipation in saturn and constraints on enceladus' thermal state from astrometry. *Astrophysical Journal*, 752(1).

Lambeck, K. (1988). *Geophysical geodesy : the slow deformations of the earth*. Oxford science publications. Clarendon Press ; Oxford University Press, Oxford England New York.

Lari, G. (2018). A semi-analytical model of the galilean satellites' dynamics. *Celestial Mechanics and Dynamical Astronomy*, 130(8).

Le Maistre, S., Rosenblatt, P., Rambaux, N., Castillo-Rogez, J. C., Dehant, V., and Marty, J.-C. (2013). Phobos interior from librations determination using doppler and star tracker measurements. *Planetary and Space Science*, 85:106–122.

Lissauer, J. J. (2009). Astronomia nova. *Nature*, 462(7274):725–725.

Macdonald, G. J. F. (1964). Tidal friction. *Reviews of Geophysics*, 2(3):467–541.

Maciejewski, A. J. (1995). Reduction, relative equilibria and potential in the two rigid bodies problem. *Celestial Mechanics & Dynamical Astronomy*, 63(1):1–28.

Makarov, V. V. and Efroimsky, M. (2014). Tidal dissipation in a homogeneous spherical body. ii. three examples: Mercury, io, and kepler-10 b. *The Astrophysical Journal*, 795(1).

Mignard, F. (1979). Evolution of the lunar orbit revisited .1. *Moon and the Planets*, 20(3):301–315.

Mignard, F. (1980). The evolution of the lunar orbit revisited .2. *Moon and the Planets*, 23(2):185–201.

Montenbruck, O. and Gill, E. (2000). *Satellite orbits : models, methods, and applications*. Springer, Berlin New York.

Murray, C. D. and Dermott, S. F. (1999). *Solar system dynamics*. Cambridge University Press, Cambridge ; New York.

Newton, I., Motte, A., and Machin, J. (1729). *The mathematical principles of natural philosophy*. Printed for B. Motte, London,.

Petit, G. and Luzum, B. (2010). Iers conventions (2010), technical note 36. Report 1019-4568, International Earth Rotation and Reference Systems Service (IERS).

Rambaux, N., Castillo-Rogez, J. C., Le Maistre, S., and Rosenblatt, P. (2012). Rotational motion of phobos. *Astronomy & Astrophysics*, 548.

Remus, F., Mathis, S., and Zahn, J. P. (2012a). The equilibrium tide in stars and giant planets i. the coplanar case. *Astronomy & Astrophysics*, 544.

Remus, F., Mathis, S., Zahn, J. P., and Lainey, V. (2012b). Anelastic tidal dissipation in multi-layer planets. *Astronomy & Astrophysics*, 541.

Renaud, J. P. and Henning, W. G. (2018). Increased tidal dissipation using advanced rheological models: Implications for io and tidally active exoplanets. *Astrophysical Journal*, 857(2).

Singer, S. F. (1968). Origin of moon and geophysical consequences. *Geophysical Journal of the Royal Astronomical Society*, 15(1-2):205–.

Souchay, J., Mathis, S., and Tokieda, T. (2013). *Tides in astronomy and astrophysics*. Lecture notes in physices,. Springer, Heidelberg ; New York.

Turcotte, D. L., Schubert, G., and Turcotte, D. L. (2002). *Geodynamics*. Cambridge University Press, Cambridge ; New York, 2nd edition.

Turyshev, S. G., Farr, W., Folkner, W. M., Girerd, A. R., Hemmati, H., Murphy, T. W., Williams, J. G., and Degnan, J. J. (2010). Advancing tests of relativistic gravity via laser ranging to phobos. *Experimental Astronomy*, 28(2):209–249.

Viswanathan, V., Fienga, A., Gastineau, M., and Laskar, J. (2017). Inpop17a planetary ephemerides.

Willner, K., Oberst, J., Hussmann, H., Giese, B., Hoffmann, H., Matz, K. D., Roatsch, T., and Duxbury, T. (2010). Phobos control point network, rotation, and shape. *Earth and Planetary Science Letters*, 294(3):541–546.

Appendices

A. Quaternions

The quaternion vector defined as $\boldsymbol{q} = (q_0,\, q_1,\, q_2,\, q_3)$ satisfies the normalization condition stating that the sum of its squared variables is equal to 1. Furthermore, it relates to the unit axes of the rotating frame ($\hat{\boldsymbol{e}}_\mathrm{A}$, $\hat{\boldsymbol{e}}_\mathrm{B}$, $\hat{\boldsymbol{e}}_\mathrm{C}$) as (Fukushima 2008)

$$\begin{aligned}
\hat{\boldsymbol{e}}_\mathrm{A} &= \begin{pmatrix} {q_0}^2 + {q_1}^2 - {q_2}^2 - {q_3}^2 \\ 2(q_0 q_3 + q_1 q_2) \\ 2(q_1 q_3 - q_0 q_2) \end{pmatrix}, \\
\hat{\boldsymbol{e}}_\mathrm{B} &= \begin{pmatrix} 2(q_1 q_2 - q_0 q_3) \\ {q_0}^2 - {q_1}^2 + {q_2}^2 - {q_3}^2 \\ 2(q_0 q_1 + q_2 q_3) \end{pmatrix}, \\
\hat{\boldsymbol{e}}_\mathrm{C} &= \begin{pmatrix} 2(q_0 q_2 + q_1 q_3) \\ 2(q_2 q_3 - q_0 q_1) \\ {q_0}^2 - {q_1}^2 - {q_2}^2 + {q_3}^2 \end{pmatrix}.
\end{aligned} \tag{A.1}$$

The reverse transformation is given as

$$\begin{aligned}
q_0 &= \frac{1}{2}\sqrt{1 + (\hat{\boldsymbol{e}}_\mathrm{A})_X + (\hat{\boldsymbol{e}}_\mathrm{B})_Y + (\hat{\boldsymbol{e}}_\mathrm{C})_Z}\,, \\
q_1 &= \frac{(\hat{\boldsymbol{e}}_\mathrm{B})_Z - (\hat{\boldsymbol{e}}_\mathrm{C})_Y}{4q_0}\,, \\
q_2 &= \frac{(\hat{\boldsymbol{e}}_\mathrm{C})_X - (\hat{\boldsymbol{e}}_\mathrm{A})_Z}{4q_0}\,, \\
q_3 &= \frac{(\hat{\boldsymbol{e}}_\mathrm{A})_Y - (\hat{\boldsymbol{e}}_\mathrm{B})_X}{4q_0}\,,
\end{aligned} \tag{A.2}$$

with the single condition that q_0 is nonzero. Other transformations can be used whenever this is the case (Fukushima 2008).

B. The tidal potential linearized

Starting from the tidal potential generated by a body at time $t - \Delta t$ and position $\boldsymbol{r}_\mathrm{s}(t - \Delta t)$, it can be assumed that (Mignard 1979)

$$V_\mathrm{T}(\boldsymbol{r}) = \sum_{l=2}^{\infty} \left(\frac{R_\mathrm{E}}{|\boldsymbol{r}|}\right)^{l+1} k_l W_l(\boldsymbol{R}, \boldsymbol{r}_\mathrm{s}(t - \Delta t))\,, \tag{B.1}$$

with $\boldsymbol{r}$ the position of the calculated potential, R_E the equatorial radius of the perturbed body, k_l the static Love number and $W_l(\boldsymbol{R}, \boldsymbol{r}_\mathrm{s}(t - \Delta t))$ the perturbing potential at the surface point $\boldsymbol{R}$ below the position $\boldsymbol{r}$ caused by the perturbing body at position $\boldsymbol{r}_\mathrm{s}(t - \Delta t)$. From now on for clarity the tidal potential will also be expressed with a second variable denoting the position of the perturbing body, which means in this case that $V_\mathrm{T}(\boldsymbol{r}) = V_\mathrm{T}(\boldsymbol{r}, \boldsymbol{r}_\mathrm{s}(t - \Delta t))$. The time lag Δt can usually be regarded to be small (Mignard 1980). This means that the position can be linearized with

$$\boldsymbol{r}_\mathrm{s}(t - \Delta t) = \boldsymbol{r}_\mathrm{s}(t) - \boldsymbol{v}_\mathrm{s}(t)\Delta t + \boldsymbol{\omega}_\mathrm{c}\Delta t \times \boldsymbol{r}_\mathrm{s}(t)\,, \tag{B.2}$$

where the $\boldsymbol{\omega}_\mathrm{c}$ denotes the angular velocity of the perturbed body. To simplify the tidal potential at Equation B.1, also this potential is linearized in Equation B.3 as

$$\begin{aligned}
V_\mathrm{T}(\boldsymbol{r}, \boldsymbol{r}_\mathrm{s}(t - \Delta t)) &= V_\mathrm{T}(\boldsymbol{r}, \boldsymbol{r}_\mathrm{s}(t)) \\
&\quad + \boldsymbol{\nabla}_{\boldsymbol{r}_\mathrm{s}} V_\mathrm{T}(\boldsymbol{r}, \boldsymbol{r}_\mathrm{s}(t)) \cdot (\boldsymbol{r}_\mathrm{s}(t - \Delta t) - \boldsymbol{r}_\mathrm{s}(t)) \\
&= \sum_{l=2}^{\infty} \left(\frac{R_\mathrm{E}}{|\boldsymbol{r}|}\right)^{l+1} k_l W_l(\boldsymbol{R}, \boldsymbol{r}_\mathrm{s}(t)) \\
&\quad + \boldsymbol{\nabla}_{\boldsymbol{r}_\mathrm{s}} \left[\sum_{l=2}^{\infty} \left(\frac{R_\mathrm{E}}{|\boldsymbol{r}|}\right)^{l+1} k_l W_l(\boldsymbol{R}, \boldsymbol{r}_\mathrm{s}(t))\right] (\boldsymbol{\omega}_\mathrm{c} \times \boldsymbol{r}_\mathrm{s}(t) - \boldsymbol{v}_\mathrm{s})\Delta t\,.
\end{aligned} \tag{B.3}$$

With the gradient worked out in Equation B.4

$$\begin{aligned}
\boldsymbol{\nabla}_{\boldsymbol{r}_\mathrm{s}} V_\mathrm{T}(\boldsymbol{r}, \boldsymbol{r}_\mathrm{s}(t)) &= \boldsymbol{\nabla}_{\boldsymbol{r}_\mathrm{s}} \left[\sum_{l=2}^{\infty} \left(\frac{R_\mathrm{E}}{|\boldsymbol{r}|}\right)^{l+1} k_l W_l(\boldsymbol{R}, \boldsymbol{r}_\mathrm{s}(t))\right] \\
&= -GM_\mathrm{s} \boldsymbol{\nabla}_{\boldsymbol{r}_\mathrm{s}} \left[\sum_{l=2}^{\infty} \frac{k_l {R_\mathrm{E}}^{2l+1}}{|\boldsymbol{r}|^{l+1} |\boldsymbol{r}_\mathrm{s}(t)|^{l+1}} P_l\left(\frac{\boldsymbol{r} \cdot \boldsymbol{r}_\mathrm{s}(t)}{|\boldsymbol{r}||\boldsymbol{r}_\mathrm{s}(t)|}\right)\right] \\
&= -GM_\mathrm{s} \sum_{l=2}^{\infty} \frac{k_l {R_\mathrm{E}}^{2l+1}}{|\boldsymbol{r}|^{l+1} |\boldsymbol{r}_\mathrm{s}|^{l+1}} \left[-\frac{(l+1)\boldsymbol{r}_\mathrm{s}}{{|\boldsymbol{r}_\mathrm{s}|}^2} P_l(x)\right. \\
&\quad \left. + \left.\frac{\mathrm{d}P_l}{\mathrm{d}x}\right|^x \cdot \left(\frac{\boldsymbol{r}}{|\boldsymbol{r}||\boldsymbol{r}_\mathrm{s}|} - \frac{(\boldsymbol{r} \cdot \boldsymbol{r}_\mathrm{s})\boldsymbol{r}_\mathrm{s}}{|\boldsymbol{r}||\boldsymbol{r}_\mathrm{s}|^3}\right)\right],
\end{aligned} \tag{B.4}$$

the tidal potential becomes

$$\begin{aligned}
V_\mathrm{T}(\boldsymbol{r}, \boldsymbol{r}_\mathrm{s}(t - \Delta t)) &= V_\mathrm{T}(\boldsymbol{r}, \boldsymbol{r}_\mathrm{s}(t)) - GM_\mathrm{s} \sum_{l=2}^{\infty} \frac{k_l {R_\mathrm{E}}^{2l+1}}{|\boldsymbol{r}|^{l+2} |\boldsymbol{r}_\mathrm{s}|^{l+1}} \Delta t \\
&\quad \cdot \left[\frac{(l+1)(\boldsymbol{r}_\mathrm{s} \cdot \boldsymbol{v}_\mathrm{s})}{{|\boldsymbol{r}_\mathrm{s}|}^2} |\boldsymbol{r}| P_l(x) + \left.\frac{\mathrm{d}P_l}{\mathrm{d}x}\right|^x \right. \\
&\quad \left. \cdot \left(\frac{\boldsymbol{r} \cdot (\boldsymbol{\omega}_\mathrm{c} \times \boldsymbol{r}_\mathrm{s})}{|\boldsymbol{r}_\mathrm{s}|} - \frac{\boldsymbol{r} \cdot \boldsymbol{v}_\mathrm{s}}{|\boldsymbol{r}_\mathrm{s}|} + \frac{(\boldsymbol{r} \cdot \boldsymbol{r}_\mathrm{s})(\boldsymbol{r}_\mathrm{s} \cdot \boldsymbol{v}_\mathrm{s})}{{|\boldsymbol{r}_\mathrm{s}|}^3}\right)\right],
\end{aligned} \tag{B.5}$$

where for notation simplicity the position $\boldsymbol{r}_\mathrm{s}(t) = \boldsymbol{r}_\mathrm{s}$ and $x = \left(\frac{\boldsymbol{r} \cdot \boldsymbol{r}_\mathrm{s}}{|\boldsymbol{r}||\boldsymbol{r}_\mathrm{s}|}\right)$.
To find the force and consequently the torque, the gradient with respect to $\boldsymbol{r}$ has to be taken of this potential. This

leads to

$$
\begin{aligned}
&\boldsymbol{\nabla}_{\boldsymbol{r}} V_{\mathrm{T}}(\boldsymbol{r}, \boldsymbol{r}_{\mathrm{s}}(t-\Delta t)) = \boldsymbol{\nabla}_{\boldsymbol{r}} V_{\mathrm{T}}(\boldsymbol{r}, \boldsymbol{r}_{\mathrm{s}}(t)) \\
&\quad - GM_{\mathrm{s}} \sum_{l=2}^{\infty} \Bigg\{ - \frac{(l+2) k_l {R_{\mathrm{E}}}^{2l+1} \boldsymbol{r}}{|\boldsymbol{r}|^{l+4} |\boldsymbol{r}_{\mathrm{s}}|^{l+1}} \Delta t \\
&\quad \cdot \left[\frac{(l+1)(\boldsymbol{r}_{\mathrm{s}} \cdot \boldsymbol{v}_{\mathrm{s}})}{|\boldsymbol{r}_{\mathrm{s}}|^2} |\boldsymbol{r}| P_l(x) \right. \\
&\quad + \left. \frac{\mathrm{d}P_l}{\mathrm{d}x}\Big|^x \cdot \left(\frac{\boldsymbol{r} \cdot (\boldsymbol{\omega}_{\mathrm{c}} \times \boldsymbol{r}_{\mathrm{s}})}{|\boldsymbol{r}_{\mathrm{s}}|} - \frac{\boldsymbol{r} \cdot \boldsymbol{v}_{\mathrm{s}}}{|\boldsymbol{r}_{\mathrm{s}}|} \right. \right. \\
&\quad \left. \left. + \frac{(\boldsymbol{r} \cdot \boldsymbol{r}_{\mathrm{s}})(\boldsymbol{r}_{\mathrm{s}} \cdot \boldsymbol{v}_{\mathrm{s}})}{|\boldsymbol{r}_{\mathrm{s}}|^3} \right) \right] + \frac{k_l {R_{\mathrm{E}}}^{2l+1}}{|\boldsymbol{r}|^{l+2} |\boldsymbol{r}_{\mathrm{s}}|^{l+1}} \Delta t \\
&\quad \cdot \left[\frac{(l+1)(\boldsymbol{r}_{\mathrm{s}} \cdot \boldsymbol{v}_{\mathrm{s}}) \boldsymbol{r}}{|\boldsymbol{r}| |\boldsymbol{r}_{\mathrm{s}}|^2} P_l(x) + \frac{(l+1)(\boldsymbol{r}_{\mathrm{s}} \cdot \boldsymbol{v}_{\mathrm{s}})}{|\boldsymbol{r}_{\mathrm{s}}|^2} |\boldsymbol{r}| \ \frac{\mathrm{d}P_l}{\mathrm{d}x}\Big|^x \right. \\
&\quad \cdot \left(\frac{\boldsymbol{r}_{\mathrm{s}}}{|\boldsymbol{r}||\boldsymbol{r}_{\mathrm{s}}|} - \frac{(\boldsymbol{r} \cdot \boldsymbol{r}_{\mathrm{s}}) \boldsymbol{r}}{|\boldsymbol{r}|^3 |\boldsymbol{r}_{\mathrm{s}}|} \right) + \frac{\mathrm{d}^2 P_l}{\mathrm{d}x^2}\Big|^x \cdot \left(\frac{\boldsymbol{r}_{\mathrm{s}}}{|\boldsymbol{r}||\boldsymbol{r}_{\mathrm{s}}|} - \frac{(\boldsymbol{r} \cdot \boldsymbol{r}_{\mathrm{s}}) \boldsymbol{r}}{|\boldsymbol{r}|^3 |\boldsymbol{r}_{\mathrm{s}}|} \right) \\
&\quad \cdot \left(\frac{\boldsymbol{r} \cdot (\boldsymbol{\omega}_{\mathrm{c}} \times \boldsymbol{r}_{\mathrm{s}})}{|\boldsymbol{r}_{\mathrm{s}}|} - \frac{\boldsymbol{r} \cdot \boldsymbol{v}_{\mathrm{s}}}{|\boldsymbol{r}_{\mathrm{s}}|} + \frac{(\boldsymbol{r} \cdot \boldsymbol{r}_{\mathrm{s}})(\boldsymbol{r}_{\mathrm{s}} \cdot \boldsymbol{v}_{\mathrm{s}})}{|\boldsymbol{r}_{\mathrm{s}}|^3} \right) \\
&\quad \left. + \frac{\mathrm{d}P_l}{\mathrm{d}x}\Big|^x \cdot \left(\frac{\boldsymbol{\omega}_{\mathrm{c}} \times \boldsymbol{r}_{\mathrm{s}}}{|\boldsymbol{r}_{\mathrm{s}}|} - \frac{\boldsymbol{v}_{\mathrm{s}}}{|\boldsymbol{r}_{\mathrm{s}}|} + \frac{\boldsymbol{r}_{\mathrm{s}} (\boldsymbol{r}_{\mathrm{s}} \cdot \boldsymbol{v}_{\mathrm{s}})}{|\boldsymbol{r}_{\mathrm{s}}|^3} \right) \right] \Bigg\} .
\end{aligned} \tag{B.6}
$$

By noting that the force will be evaluated at $\boldsymbol{r} = \boldsymbol{r}_{\mathrm{s}}$, consequently making $x = \left(\frac{\boldsymbol{r} \cdot \boldsymbol{r}_{\mathrm{s}}}{|\boldsymbol{r}||\boldsymbol{r}_{\mathrm{s}}|} \right) = 1$ and stating that $P_l(1) = 1$ and $\frac{\mathrm{d}P_l}{\mathrm{d}x}\Big|^1 = \frac{l(l+1)}{2}$ the force results into

$$
\begin{aligned}
\boldsymbol{F}_{\mathrm{T}} =& - M_{\mathrm{s}} \boldsymbol{\nabla}_{\boldsymbol{r}} V_{\mathrm{T}}(\boldsymbol{r}, \boldsymbol{r}_{\mathrm{s}}(t-\Delta t)) \\
=& GM_{\mathrm{s}}{}^2 \sum_{l=2}^{\infty} \frac{k_l {R_{\mathrm{E}}}^{2l+1}}{|\boldsymbol{r}|^{2l+4}} \cdot \Bigg(- (l+1) \boldsymbol{r} \\
&+ \frac{l(l+1)}{2} (\boldsymbol{r} - \boldsymbol{r}) \Bigg) \\
&+ GM_{\mathrm{s}}{}^2 \sum_{l=2}^{\infty} \Bigg\{ - \frac{(l+2) k_l {R_{\mathrm{E}}}^{2l+1} \boldsymbol{r}}{|\boldsymbol{r}|^{2l+5}} \Delta t \\
&\cdot \left[\frac{(l+1)(\boldsymbol{r} \cdot \boldsymbol{v})}{|\boldsymbol{r}|} + \frac{l(l+1)}{2} \cdot \left(0 - \frac{\boldsymbol{r} \cdot \boldsymbol{v}}{|\boldsymbol{r}|} + \frac{\boldsymbol{r} \cdot \boldsymbol{v}}{|\boldsymbol{r}|} \right) \right] \\
&+ \frac{k_l {R_{\mathrm{E}}}^{2l+1}}{|\boldsymbol{r}|^{2l+4}} \Delta t \cdot \left[\frac{(l+1)(\boldsymbol{r} \cdot \boldsymbol{v}) \boldsymbol{r}}{|\boldsymbol{r}|^2} + (l+1)(\boldsymbol{r} \cdot \boldsymbol{v}) \frac{l(l+1)}{2} \right. \\
&\cdot \left(\frac{\boldsymbol{r}}{|\boldsymbol{r}|^2} - \frac{\boldsymbol{r}}{|\boldsymbol{r}|^2} \right) + \frac{\mathrm{d}^2 P_l}{\mathrm{d}x^2}\Big|^1 \cdot \left(\frac{\boldsymbol{r}}{|\boldsymbol{r}|} - \frac{\boldsymbol{r}}{|\boldsymbol{r}|} \right) \\
&\cdot \left(0 - \frac{\boldsymbol{r} \cdot \boldsymbol{v}}{|\boldsymbol{r}|} + \frac{\boldsymbol{r} \cdot \boldsymbol{v}}{|\boldsymbol{r}|} \right) + \frac{l(l+1)}{2} \\
&\left. \cdot \left(\boldsymbol{\omega}_{\mathrm{c}} \times \boldsymbol{r} - \boldsymbol{v} + \frac{\boldsymbol{r}(\boldsymbol{r} \cdot \boldsymbol{v})}{|\boldsymbol{r}|^2} \right) \right] \Bigg\} \\
=& - GM_{\mathrm{s}}{}^2 \sum_{l=2}^{\infty} \frac{k_l {R_{\mathrm{E}}}^{2l+1}}{|\boldsymbol{r}|^{2l+4}} \cdot (l+1) \boldsymbol{r} \\
&- GM_{\mathrm{s}}{}^2 \sum_{l=2}^{\infty} \Bigg\{ \frac{(l+2) k_l {R_{\mathrm{E}}}^{2l+1} \boldsymbol{r}}{|\boldsymbol{r}|^{2l+4}} \Delta t \cdot \left[\frac{(l+1)(\boldsymbol{r} \cdot \boldsymbol{v})}{|\boldsymbol{r}|^2} \right] \\
&- \frac{k_l {R_{\mathrm{E}}}^{2l+1}}{|\boldsymbol{r}|^{2l+4}} \Delta t \cdot \left[\frac{(l+1)(\boldsymbol{r} \cdot \boldsymbol{v}) \boldsymbol{r}}{|\boldsymbol{r}|^2} + \frac{l(l+1)}{2} \right. \\
&\left. \left. \cdot \left(\boldsymbol{\omega}_{\mathrm{c}} \times \boldsymbol{r} - \boldsymbol{v} + \frac{\boldsymbol{r}(\boldsymbol{r} \cdot \boldsymbol{v})}{|\boldsymbol{r}|^2} \right) \right] \right\} \\
=& - GM_{\mathrm{s}}{}^2 \sum_{l=2}^{\infty} \frac{k_l {R_{\mathrm{E}}}^{2l+1}}{|\boldsymbol{r}|^{2l+4}} (l+1) \Bigg\{ \boldsymbol{r} + \Delta t \left[\frac{(l+2) \boldsymbol{r} (\boldsymbol{r} \cdot \boldsymbol{v})}{|\boldsymbol{r}|^2} \right. \\
&- \frac{\boldsymbol{r}(\boldsymbol{r} \cdot \boldsymbol{v})}{|\boldsymbol{r}|^2} - \frac{l}{2} \frac{\boldsymbol{r}(\boldsymbol{r} \cdot \boldsymbol{v})}{|\boldsymbol{r}|^2} - \frac{l}{2} (-\boldsymbol{r} \times \boldsymbol{\omega}_{\mathrm{c}} - \boldsymbol{v}) \Bigg] \Bigg\} \\
=& - GM_{\mathrm{s}}{}^2 \sum_{l=2}^{\infty} \left[(l+1) \frac{k_l {R_{\mathrm{E}}}^{2l+1}}{|\boldsymbol{r}|^{2l+4}} \Bigg(\boldsymbol{r} \right. \\
&\left. + \Delta t \left\{ \frac{l}{2} (\boldsymbol{r} \times \boldsymbol{\omega}_{\mathrm{c}} + \boldsymbol{v}) + \frac{l+2}{2} \frac{(\boldsymbol{r} \cdot \boldsymbol{v}) \boldsymbol{r}}{|\boldsymbol{r}|^2} \right\} \Bigg) \Bigg] ,
\end{aligned} \tag{B.7}
$$

which is conform the theory (Mignard 1980). Many authors (e.g. Lainey et al. 2007; Lari 2018) use only the second degree potential and force. This results then in

$$
\boldsymbol{F}_{\mathrm{T}} = -3 \frac{GM_{\mathrm{s}}{}^2 k_2 {R_{\mathrm{E}}}^5}{|\boldsymbol{r}|^8} \left[\boldsymbol{r} + \Delta t \left(\boldsymbol{r} \times \boldsymbol{\omega}_{\mathrm{c}} + \boldsymbol{v} + 2 \frac{\boldsymbol{r}(\boldsymbol{r} \cdot \boldsymbol{v})}{|\boldsymbol{r}|^2} \right) \right] . \tag{B.8}
$$

3

Conclusions

This chapter concludes the findings of the research and tries to give an answer to whether the use of a coupled model can be beneficial, as part of answering the complete set of research questions. The research questions are repeated and answers are given below.
The top-level research question is regarded after all lower-level and sub-questions are properly answered. The question is as stated in the introduction:

What is the benefit of using a fully coupled translational-rotational-tidal model, when comparing with currently used other models and literature approximations, and for what systems could this be beneficial?

The two lower-level research questions and accompanied sub-questions should explain the top-level one and are:

1. What is the benefit of using a fully coupled model, when comparing with currently used other models and literature approximations, for a 2D system with tides on the primary?

    - What is the behaviour of the coupled model for the test-cases Mars-Phobos and Earth-Moon, when regarding the evolution of the tidal geopotential coefficients, accompanied tidal lag angle and time lag?

      The evolution of the tidal lag is regarded only for the coupled model, as the direct tidal dissipation force model from Lainey et al. (2007) does not calculate the change in tidal geopotential coefficients and thus also no lag. The mean of the tidal lag angle and time lag for the coupled model show no difference with the classical calculation of the phase lag via the Q factor. After relaxation times are surpassed, the tidal lag angles and time lags converges exactly to a periodical behaviour around this literature value. This holds for both systems, for the preceding tidal bulge of the Earth-Moon system and the lagging bulge of the Mars-Phobos system. In these varying lag angle and time lag, the coupled model displays behaviour which is by definition not captured by the classical direct tidal force models. The amplitude of the tidal coefficients that govern the lag angle seems to resemble literature values. Only the tidal coefficient ΔJ_2 does not resemble theory, but that could be explained by the exclusion of the dependence of ΔJ_2 on the rotation.

    - What is the behaviour of the coupled model for the test-cases Mars-Phobos and Earth-Moon, when regarding the evolution of the orbital elements?

      The evolution of the semi-major axis determined by the coupled model is similar to the literature approximation of this evolution. For a range of input parameters varying the relaxation times of the coupled model, and in so on varying the currently used tidal parameters k_2 and

Q, all changes in semi-major axis seem to correspond to literature.
*The eccentricity change is more difficult to determine, as it is an order of magnitude closer to the step error of the propagation, and shows a difference with the literature approximation. As well a difference is encountered between the different systems regarded. The Mars-Phobos system shows a coupled model that follows the literature approximation, though only with a small constant offset factor. The Earth-Moon system shows peculiar and interesting behaviour for the eccentricity change. Similar k_2 over Q ratios show different eccentricity changes. It follows the literature linear behaviour of a positive acceleration of the eccentricity for higher k_2 and Q variables, but turns completely different for lower values. The exact reason for this discrepancy is yet to be determined, but it could be because only a minor secular change is present, and it is superimposed upon large per-orbit variations. The linear position differences between the current direct tidal force model and the coupled model are small (*3 cm *for the Phobos-Mars system, and* 1.5 mm *for the Earth-Moon system after one day of propagation). However, they might become important for future space missions as data ranging observations become more accurate.*

To answer the first lower-level research question: The evolution of the semi-major axis determined by the coupled model is similar to the current methods for tidal effects and similar to the literature approximation of this evolution. For a range of input parameters varying the relaxation times of the coupled model, and in so on varying the currently used tidal parameters k_2 and Q, all changes in semi-major axis correspond to literature and current direct tidal force modeling methods.
Although similar, the difference between the position vectors after 1 central body day is 3 cm *for the Mars-Phobos system, and only* 1.5 mm *for the Earth-Moon system. These values are small, but might be important for future space missions as data ranging observations become more accurate. Assuming the coupled model to lie closer to the truth, it will be beneficial to use the coupled model for these high-accurate observation missions. It will indeed provide more accurate approximations of the body's characteristics and tidal parameters. However, the direct tidal force model can still be used for the current level of accuracy.*
For longer time-scales, in the order of thousands to billions of years, it would also be beneficial to switch to the coupled model. The classical direct tidal force model assumes a constant, or only a frequency dependent quality factor that averages the tidal dissipation. The coupled model is not dependent on the quality factor and time variations in the tidal dissipation are more easily captured. The input tidal parameters used in the coupled model (τ_e and τ_2), however, have to be estimated more accurately by using real data.

2. What is the benefit of using a fully coupled model, when comparing with currently used other models and literature approximations, for a 2D system with tides on the locked secondary?

   - What is the behaviour of the coupled model for the test-cases Phobos-Mars and Moon-Earth, when regarding the evolution of the tidal geopotential coefficients?

     The tidal coefficients for the locked satellite converge to a periodical function around a static counterpart. The convergence is reached after the relaxation times are exceeded. For the tides on the satellite, these relaxation times can become large (order of years). This fact could potentially form a problem for the coupled model, because the transients in the model should be damped to be able to compare the model with reality. For a propagation to make sense, first a damped state has to be found for every single initial condition, which can be time-consuming. The classical models do not show this behaviour.

   - What is the behaviour of the coupled model for the test-cases Phobos-Mars and Moon-Earth, when regarding the evolution of the orbital elements and librations?

     The evolution of both the semi-major axis and the eccentricity for the Phobos-Mars case do not show resemblance with the literature approximations from Souchay et al. (2013) or from Boué (2019). The changes are much larger for the coupled model. This can be explained

when comparing with a literature approximation which takes account for the large physical librations present on Phobos. In its coupling between the translational, rotational and tidal dynamics, the coupled model takes these physical librations and their caused additional dissipation into account in the propagations. The classical models do not take these librations properly into account.
The coupled model shows different behaviour for the Moon-Earth case. The Moon does not have a large physical libration and in order of magnitude the coupled model displays similar orbital changes as the literature approximations from Souchay et al. (2013). The scientific community is not sure which is the correct literature approximation, and as well the classical direct tidal force models show different behaviour for the change in semi-major axis. Following the coupled model's behaviour, only a single literature approximation can be assumed correct (Souchay et al. 2013).

To answer the second lower-level research question: The second part of the research is performed on a system with the tides on the secondary. Especially for the system Phobos-Mars, with the tides on Phobos, a coupled model behaves differently than all current models. Phobos exhibits a large physical libration, which causes an additional dissipation that can become the largest factor in the overall tidal dissipation. The additional dissipation results in a faster evolution of both the semi-major axis and the eccentricity. This effect is only captured by the coupled model, and not by the currently used models.
The Moon-Earth case, with the tides on the Moon, does not have these librations, and evolution values lie closer. The coupled model shows a different behaviour for the semi-major axis evolution than other currently used models but does follow the literature approximation accurately. The scientific community itself did not decide yet on the correct literature approximation, and as well the classical models show different behaviour for the change in semi-major axis.

Ultimately, the main research question can be answered as follows:

Overall, the coupled model behaves exactly as it should for a variation of tidal input parameters. These input parameters have yet to be determined for most solar system bodies, which could be done in further studies involving real position data. For short timescales, currently used methods or literature approximations can still be used whenever data requirements are not high. However, when dealing with high accuracy observations, and for bodies with larger physical librations, it rewards to switch to a coupled method. It takes properly into account the frequency dependency and possible variation of classical tidal parameters are caught. The method is also valid for larger eccentricities and inclinations, and remains valid for any orientation and spin rate. Furthermore, it is able to capture the behaviour of secondary bodies with large physical librations. With this coupled model, more accurate propagations could be performed that tell us more about the body's material. It could give more information about the origin and long term evolution of the systems regarded, and in that way, it could give more information about the origin of life itself.

4

Recommendations

This chapter states some undone work and recommendations for further research opportunities to use the coupled translational-rotational-tidal model. The following is recommended:

- Validate the coupled model in three dimensions, now including systems with inclined orbiting satellites.

  The coupled model discussed in this thesis is two-dimensional, which is only possible for systems with spin vectors aligned with the orbital angular momentum vector, i.e. have no inclined orbiting satellite. Many systems do not have this alignment, for example the Earth-Moon system. The coupled model should be able to deal with any inclined system, but this has not been tested yet for cases in the Solar system.

- Add additional satellite bodies to the model, which then would be applicable in more complex test-cases with for example the Galilean moons of Jupiter, or in the case with the additional other moon of Mars, Deimos.

  It would be interesting to investigate the tidal behaviour of interacting satellites with the coupled model and compare this with the currently used models. This is interesting as the orbital periods of the separate satellites can cause a resonance within the tidal behaviour that further influences the orbital evolution of the system regarded. The effect of a coupled model herein is not yet investigated.

- Perform a validation of the coupled model for the case where both the primary as the secondary body experience each others tides.

  The current model tests separately the tides on the primary and the secondary. Including these separate tides together has been done before, but not for the coupled model. Tests could be performed to see if literature approximations can be easily add up to acquire the total evolution of the system or whether more difficult evaluations are necessary.

- Test the performed research and all of the above proposed recommendations with real position data.

  Real position data of test-case bodies, for example obtained through the tracking of space vehicles, can be used to fit to the coupled model. The tidal parameters of the model, until now only derived through their relation via classical tidal parameters, could be obtained and a more accurate statement on whether the coupled model gives more accurate short-time propagations than currently used models can be made. It ultimately defines whether the coupled model can be used in later space missions for orbit prediction and determination.

- Perform long-term propagations to see the use of the coupled model for the long term evolution of the system.

  The long term propagations performed in this thesis are by far not long enough to state something about the actual origin of these bodies and systems. Performing longer propagations could eventually state something about the origin or actual end or long-term evolution of bodies and systems.

- See if other rheological models would increase the accuracy of the coupled model.

  The currently used Maxwell model for the rheology of the bodies is relatively simple. Other options that are able to deal with more complex reactions inside the body are available, for example the Andrade rheology. It would be more complex to implement these, both literally and figuratively, but indeed very interesting to see how these different models compare.

Appendices

A. Additional derivations

This appendix contains multiple derivations of equations and phenomena used in the research. Either already stated in the literature study or the paper, or just not yet dictated before.

A.1. Gravitational potential of solid sphere

The gravitational potential around a point mass as seen from an inertial point mass centered reference frame is given by

$$V(\boldsymbol{r}) = -\frac{\mu}{|\boldsymbol{r}|}\,, \tag{1}$$

with $\mu = GM_{\mathrm{p}}$ the gravitational parameter of the point mass of mass M_{p} and $\boldsymbol{r}$ the required position vector. To get to the potential of a solid uniform sphere, first the potential of a ring at a certain distance from the center of the ring is calculated. The set up is sketched in Figure A.1. The potential is now

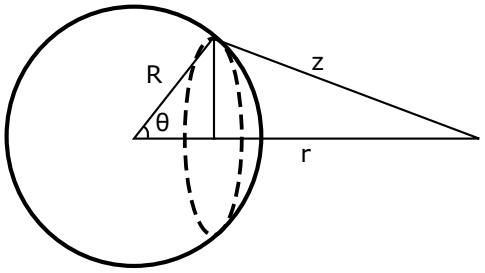

Figure A.1: Solid sphere geometry.

given by the integral of the contribution of all the mass elements of the ring. Because the distance z from the mass element of the ring to the required location of the potential is constant for this geometry, the integral becomes

$$V_{\mathrm{ring}} = -\int \frac{G\mathrm{d}M}{z} = -\frac{G}{z}\int \mathrm{d}M = -\frac{GM_{\mathrm{ring}}}{z}\,. \tag{2}$$

where M_{ring} is in this case the mass of the ring.
Secondly the potential due to a thin spherical shell is calculated. All mass contributions from the different rings should be added, in turn giving the integral

$$V_{\mathrm{shell}} = -\int \frac{GdM_{\mathrm{shell}}}{z}\,.$$

A thin ring element on the shell has mass $\mathrm{d}M_{\mathrm{shell}} = M_{\mathrm{ring}} = \rho 2\pi R\sin\theta R d\theta$, so the integral becomes,

$$V_{\mathrm{shell}} = -\int \frac{G\rho 2\pi R^2\sin\theta\mathrm{d}\theta}{z}\,,$$

with R and ρ respectively the radius and the density of the thin spherical shell. Rewriting z with the cosine law and noting that r and R are constants gives then

$$\begin{aligned} V_{\text{shell}} &= -G\rho R^2 2\pi \int_0^{\pi} \frac{\sin\theta \mathrm{d}\theta}{\sqrt{R^2 + r^2 - 2Rr\cos\theta}}\,, \\ &= -G\rho R^2 2\pi \left[\sqrt{R^2 + r^2 - 2Rr\cos\theta}\,\frac{1}{Rr}\right]_0^{\pi}\,, \\ &= -\frac{2\pi G\rho R}{r}\left(\sqrt{R^2 + r^2 + 2Rr} - \sqrt{R^2 + r^2 - 2Rr}\right)\,, \\ &= -\frac{2\pi G\rho R}{r}\left((r + R) - (r - R)\right)) = -\frac{4\pi G\rho R^2}{r}\,. \end{aligned}$$

The density of the thin shell is the mass divided by the 'volume' of the shell and thus the potential becomes

$$V_{\text{shell}} = -\frac{4\pi R^2 G}{r}\frac{M_{\text{shell}}}{4\pi R^2} = -\frac{GM_{\text{shell}}}{r}\,, \tag{3}$$

where the mass is in this case the thin shell's mass.
Lastly the potential for a solid uniform sphere can be determined by integrating over all the mass elements of the thin shells inside the sphere. Continuing with the potential for the shell gives then

$$V_{\text{sphere}} = -\int \frac{G\mathrm{d}M_{\text{shell}}}{r} = -\frac{G}{r}\int \mathrm{d}M_{\text{shell}} = -\frac{GM_{\text{sphere}}}{r}\,. \tag{4}$$

A.2. The gravitational potential expanded in spherical harmonics

The gravitational potential can be and is conventionally expanded as a series of associated Legendre polynomials. Starting from its definition (e.g. Montenbruck and Gill 2000; Dirkx et al. 2019),

$$V(\boldsymbol{r}) = -\int_{\mathrm{S}} \frac{G\mathrm{d}M}{|\boldsymbol{r} - \boldsymbol{s}|}\,, \tag{5}$$

where $\boldsymbol{r}$ is the position vector of the required potential, S the potential generating body, G the gravitational constant and $\boldsymbol{s}$ the position vector inside the body corresponding to the small dM. See Figure A.2.
Rewriting the vector part using the cosine rule gives

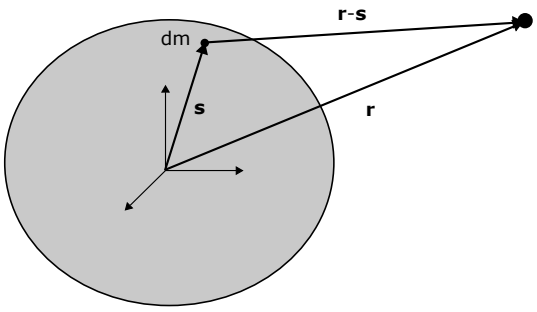

Figure A.2: The potential of a single body at a point r away.

$$|\boldsymbol{r}-\boldsymbol{s}|^{-1} = \left[r^2+s^2-2rs\cos\gamma\right]^{-1/2} = \frac{1}{r}\left[1-2\frac{s}{r}\cos\gamma+\left(\frac{s}{r}\right)^2\right]^{-1/2} = \frac{1}{r}\left[1-z\right]^{-1/2} \quad \text{with} \quad r=|\boldsymbol{r}|\,,\ s=|\boldsymbol{s}| \quad \text{and} \quad z=2ku-k^2\,,\ k=\frac{s}{r}\,,\ u=\cos\gamma\,, \tag{6}$$

where γ obviously denotes the angle between the vectors $\boldsymbol{r}$ and $\boldsymbol{s}$. Using the binomial theorem as stated in Equation 7, here valid for $|z|<1$ which is true in this case,

$$(1-z)^{-n} = \sum_{i=0}^{\infty}\binom{n+i-1}{i}z^i\,, \tag{7}$$

Equation 6 can be expanded as follows

$$\begin{aligned}\frac{1}{r}\left[1-z\right]^{-1/2} &= \frac{1}{r}\left(1+\frac{1}{2}z+\frac{3}{8}z^2+\mathcal{O}\left(z^3\right)\right)\\ &= \frac{1}{r}\left(1+ku-\frac{1}{2}k^2+\frac{3}{8}\left(4k^2u^2+k^4-4k^3u\right)+\mathcal{O}\left(z^3\right)\right)\\ &= \frac{1}{r}\left(1+ku+k^2\left(\frac{3}{2}u^2-\frac{1}{2}\right)+\mathcal{O}\left(k^3\right)\right)\\ &= \frac{1}{r}\left(P_0(u)+kP_1(u)+k^2P_2(u)+\mathcal{O}\left(k^3\right)\right)\\ &= \frac{1}{r}\sum_{l=0}^{\infty}\left(\frac{s}{r}\right)^l P_l(\cos\gamma)\,,\end{aligned} \tag{8}$$

with $P_l(x)=P_{l,0}(x)$ the zero order associated Legendre polynomials given by

$$P_{l,m}(x) = \frac{1}{2^l l!}\left(1-x^2\right)^{m/2}\frac{\mathrm{d}^{l+m}}{\mathrm{d}x^{l+m}}\left(x^2-1\right)^l\,. \tag{9}$$

A special attribute of the Legendre polynomials is the addition theorem, stating that the polynomial of a cosine of an angle between two vectors can be rewritten as a sum of associated Legendre polynomials as (e.g. Montenbruck and Gill 2000),

$$P_l(\cos\gamma) = \sum_{m=0}^{l}(2-\delta_{0m})\frac{(l-m)!}{(l+m)!}P_{lm}(\cos\theta_r)P_{lm}(\cos\theta_s)\cos(m(\phi_r-\phi_s))\,, \tag{10}$$

with θ_r and θ_s the colatitude of respectively the position vector $\boldsymbol{r}$ and $\boldsymbol{s}$, ϕ_r and ϕ_s the longitude of both respective vectors and δ_{0m} the Kronecker delta which equals 1 for $m=0$ and equals 0 otherwise. Rewriting now for the potential function gives

$$\begin{aligned}V(\boldsymbol{r}) &= -\int_{\mathrm{S}}\frac{G\,\mathrm{d}M}{|\boldsymbol{r}-\boldsymbol{s}|} = -G\int_{\mathrm{S}}\frac{1}{r}\sum_{l=0}^{\infty}\left(\frac{s}{r}\right)^l P_l(\cos\gamma)\,\mathrm{d}M\\ &= -G\int_{\mathrm{S}}\frac{1}{r}\sum_{l=0}^{\infty}\left(\frac{s}{r}\right)^l\sum_{m=0}^{l}(2-\delta_{0m})\frac{(l-m)!}{(l+m)!}P_{lm}(\cos\theta_r)P_{lm}(\cos\theta_s)\cos(m(\phi_r-\phi_s))\,\mathrm{d}M\,.\end{aligned} \tag{11}$$

Making use of the angle difference formula for the cosine, interchanging the integral and sum operators and removing the independent variables from the integral results then in

$$\begin{aligned} V(\boldsymbol{r}) &= -\frac{GM}{r}\sum_{l=0}^{\infty}\int_{\mathrm{S}}\frac{1}{M}\left(\frac{s}{r}\right)^{l}\left(\frac{R_{\mathrm{E}}}{R_{\mathrm{E}}}\right)^{l}\sum_{m=0}^{l}(2-\delta_{0m})\frac{(l-m)!}{(l+m)!}P_{lm}(\cos\theta_r)P_{lm}(\cos\theta_s) \\ &\qquad\cdot[\cos(m\phi_r)\cos(m\phi_s)+\sin(m\phi_r)\sin(m\phi_s)]\ \mathrm{d}M \\ &= -\frac{GM}{r}\sum_{l=0}^{\infty}\left(\frac{R_{\mathrm{E}}}{r}\right)^{l}\sum_{m=0}^{l}P_{lm}(\cos\theta_r)\int_{\mathrm{S}}(2-\delta_{0m})\frac{(l-m)!}{(l+m)!}\frac{1}{M}\left(\frac{s}{R_{\mathrm{E}}}\right)^{l}P_{lm}(\cos\theta_s) \\ &\qquad\cdot[\cos(m\phi_r)\cos(m\phi_s)+\sin(m\phi_r)\sin(m\phi_s)]\ \mathrm{d}M \\ &= -\frac{GM}{R_{\mathrm{E}}}\sum_{l=0}^{\infty}\left(\frac{R_{\mathrm{E}}}{|\boldsymbol{r}|}\right)^{l+1}\sum_{m=0}^{l}\left(C_{l,m}\cos(m\phi_r)+S_{l,m}\sin(m\phi_r)\right)P_{l,m}(\cos\theta_r)\,, \end{aligned} \tag{12}$$

where R_{E} denotes the equatorial radius and $C_{l,m}$ and $S_{l,m}$ defined as

$$\begin{aligned} C_{l,m} &= \int_{\mathrm{S}}(2-\delta_{0m})\frac{(l-m)!}{(l+m)!}\frac{1}{M}\left(\frac{s}{R_{\mathrm{E}}}\right)^{l}P_{lm}(\cos\theta_s)\cos(m\phi_s)\,\mathrm{d}M\,, \\ S_{l,m} &= \int_{\mathrm{S}}(2-\delta_{0m})\frac{(l-m)!}{(l+m)!}\frac{1}{M}\left(\frac{s}{R_{\mathrm{E}}}\right)^{l}P_{lm}(\cos\theta_s)\sin(m\phi_s)\,\mathrm{d}M\,. \end{aligned} \tag{13}$$

A similar but different way of describing the potential function is by making use of complex coefficients and the spherical harmonics basis function as

$$V(\boldsymbol{r}) = -\frac{GM}{R_{\mathrm{E}}}\sum_{l=0}^{\infty}\left(\frac{R_{\mathrm{E}}}{|\boldsymbol{r}|}\right)^{l+1}\sum_{m=-l}^{l}Z_{l,m}^{*}Y_{l,m}(\theta,\phi)\,, \tag{14}$$

with $Z_{l,m}^{*}$ denoting the complex conjugate of the complex coefficient $Z_{l,m}$ and $Y_{l,m}(\theta,\phi)$ defined as (Boue et al. 2016)

$$Y_{l,m}(\theta,\phi) = (-1)^{m}\sqrt{\frac{(l-m)!}{(l+m)!}}P_{l,m}(\cos\theta)\mathrm{e}^{im\phi}\,, \tag{15}$$

with the symmetry in m for $m > 0$ as

$$Y_{l,-m}(\theta,\phi) = (-1)^{m}Y_{l,m}^{*}(\theta,\phi)\,. \tag{16}$$

This is also denoted as the Schmidt semi-normalization formulation. In literature there are multiple other definitions of spherical harmonics (Dirkx et al. 2019) and good care should be taken which one is used. When comparing Equation 14 with Equation 12 the complex coefficients can be derived.

$$\begin{aligned} V(\boldsymbol{r}) &= -\frac{GM}{R_{\mathrm{E}}}\sum_{l=0}^{\infty}\left(\frac{R_{\mathrm{E}}}{|\boldsymbol{r}|}\right)^{l+1}\sum_{m=-l}^{l}Z_{l,m}^{*}Y_{l,m}(\theta,\phi)\,, \\ &= -\frac{GM}{R_{\mathrm{E}}}\sum_{l=0}^{\infty}\left(\frac{R_{\mathrm{E}}}{|\boldsymbol{r}|}\right)^{l+1}\left[Z_{l,0}^{*}Y_{l,0}(\theta,\phi)+\sum_{m=1}^{l}Z_{l,m}^{*}Y_{l,m}(\theta,\phi)+\sum_{m=-l}^{-1}Z_{l,m}^{*}Y_{l,m}(\theta,\phi)\right], \end{aligned} \tag{17}$$

Making use of the symmetry relation in Equation 16 and the definition in Equation 15 and changing to positive m values this becomes

$$\begin{aligned}
V(\boldsymbol{r}) &= -\frac{GM}{R_\mathrm{E}}\sum_{l=0}^{\infty}\left(\frac{R_\mathrm{E}}{|\boldsymbol{r}|}\right)^{l+1}\left[Z_{l,0}^{*}Y_{l,0}(\theta,\phi)+\sum_{m=1}^{l}\left(Z_{l,m}^{*}Y_{l,m}(\theta,\phi)+Z_{l,-m}^{*}Y_{l,-m}(\theta,\phi)\right)\right],\\
&= -\frac{GM}{R_\mathrm{E}}\sum_{l=0}^{\infty}\left(\frac{R_\mathrm{E}}{|\boldsymbol{r}|}\right)^{l+1}\left[Z_{l,0}^{*}P_{l,0}(\cos\theta)+\sum_{m=1}^{l}\left(Z_{l,m}^{*}Y_{l,m}(\theta,\phi)+Z_{l,-m}^{*}(-1)^{m}Y_{l,m}^{*}(\theta,\phi)\right)\right],\\
&= -\frac{GM}{R_\mathrm{E}}\sum_{l=0}^{\infty}\left(\frac{R_\mathrm{E}}{|\boldsymbol{r}|}\right)^{l+1}\left[Z_{l,0}^{*}P_{l,0}(\cos\theta)+\sum_{m=1}^{l}\left\{(-1)^{m}\sqrt{\frac{(l-m)!}{(l+m)!}}P_{l,m}(\cos\theta)\right.\right.\\
&\left.\left.\cdot\left(Z_{l,m}^{*}(\cos(m\phi)+i\sin(m\phi))+Z_{l,-m}^{*}(-1)^{m}(\cos(m\phi)-i\sin(m\phi))\right)\right\}\right],\\
&= -\frac{GM}{R_\mathrm{E}}\sum_{l=0}^{\infty}\left(\frac{R_\mathrm{E}}{|\boldsymbol{r}|}\right)^{l+1}\left[Z_{l,0}^{*}P_{l,0}(\cos\theta)+\sum_{m=1}^{l}\left\{(-1)^{m}\sqrt{\frac{(l-m)!}{(l+m)!}}P_{l,m}(\cos\theta)\right.\right.\\
&\left.\left.\cdot\left(\left(Z_{l,m}^{*}+Z_{l,-m}^{*}(-1)^{m}\right)\cos(m\phi)+\left(Z_{l,m}^{*}-Z_{l,-m}^{*}(-1)^{m}\right)i\sin(m\phi)\right)\right\}\right].
\end{aligned} \tag{18}$$

Comparing now again with Equation 12 results for $m \geq 0$ into

$$\begin{aligned}
Z_{l,0}^{*} &= C_{l,0}\,,\\
\left(Z_{l,m}^{*}+Z_{l,-m}^{*}(-1)^{m}\right)(-1)^{m}\sqrt{\frac{(l-m)!}{(l+m)!}} &= C_{l,m}\,,\\
\left(Z_{l,m}^{*}-Z_{l,-m}^{*}(-1)^{m}\right)(-1)^{m}\sqrt{\frac{(l-m)!}{(l+m)!}}i &= S_{l,m}\,.
\end{aligned} \tag{19}$$

Subtracting and adding the two latter equations then gives for $m > 0$

$$\begin{aligned}
Z_{l,m}^{*} &= \frac{1+\delta_{0m}}{2}(-1)^{m}\sqrt{\frac{(l+m)!}{(l-m)!}}\left(C_{l,m}-iS_{l,m}\right),\\
Z_{l,-m}^{*} &= \frac{1+\delta_{0m}}{2}\sqrt{\frac{(l+m)!}{(l-m)!}}\left(C_{l,m}+iS_{l,m}\right).
\end{aligned} \tag{20}$$

Combined this gives for the coefficients

$$\begin{aligned}
Z_{l,m} &= \frac{1+\delta_{0m}}{2}(-1)^{m}\sqrt{\frac{(l+m)!}{(l-m)!}}\left(C_{l,m}+iS_{l,m}\right), && \text{if} \quad m \geq 0\,,\\
Z_{l,m} &= \frac{1+\delta_{0m}}{2}\sqrt{\frac{(l-m)!}{(l+m)!}}\left(C_{l,-m}-iS_{l,-m}\right) = (-1)^{m}Z_{l,-m}^{*}\,, && \text{if} \quad m < 0\,.
\end{aligned} \tag{21}$$

A.3. The total angular momentum conservation

Regarding the two body problem with a central and satellite body, see Figure A.3, the total angular

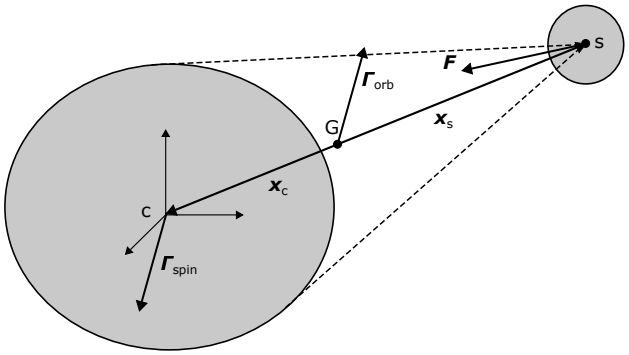

Figure A.3: The torques and angular momentum on a two body problem.

momentum is given by the separate angular momentum of the bodies as (e.g. Correia 2009; Souchay et al. 2013)

$$\boldsymbol{L}_{\mathrm{tot}} = \boldsymbol{L}_{\mathrm{orb,c}} + \boldsymbol{L}_{\mathrm{spin,c}} + \boldsymbol{L}_{\mathrm{orb,s}} + \boldsymbol{L}_{\mathrm{spin,s}} \tag{22}$$

where $\boldsymbol{L}_{\mathrm{orb,i}}$ and $\boldsymbol{L}_{\mathrm{spin,i}}$ denote the orbital and spin angular momentum of body i respectively. Using a true inertial system with origin in the center of mass of the system G, the change of the total angular moment over time can be written as

$$\frac{\mathrm{d}\boldsymbol{L}_{\mathrm{tot}}}{\mathrm{d}t} = \frac{\mathrm{d}\boldsymbol{L}_{\mathrm{spin,c}}}{\mathrm{d}t} + \frac{\mathrm{d}\boldsymbol{L}_{\mathrm{spin,s}}}{\mathrm{d}t} + M_{\mathrm{c}}\boldsymbol{x}_{\mathrm{c}} \times \frac{\mathrm{d}\boldsymbol{v}_{\mathrm{c}}}{\mathrm{d}t} + M_{\mathrm{s}}\boldsymbol{x}_{\mathrm{s}} \times \frac{\mathrm{d}\boldsymbol{v}_{\mathrm{s}}}{\mathrm{d}t} = 0\,, \tag{23}$$

which is zero per definition. The m_i denotes the mass of body i and the $\boldsymbol{x}_i$ and $\boldsymbol{v}_i$ the respective position and velocity vectors, all as seen from the barycenter G of the system. Using the definition of the barycenter, which is

$$\frac{\boldsymbol{x}_{\mathrm{c}}M_{\mathrm{c}} + \boldsymbol{x}_{\mathrm{s}}M_{\mathrm{s}}}{M_{\mathrm{c}} + M_{\mathrm{s}}} = \boldsymbol{0}\,, \tag{24}$$

Equation 23 can be rewritten to

$$\begin{aligned}
\frac{\mathrm{d}\boldsymbol{L}_{\mathrm{tot}}}{\mathrm{d}t} &= \frac{\mathrm{d}\boldsymbol{L}_{\mathrm{spin,c}}}{\mathrm{d}t} + \frac{\mathrm{d}\boldsymbol{L}_{\mathrm{spin,s}}}{\mathrm{d}t} + M_{\mathrm{c}}\left(\boldsymbol{x}_{\mathrm{c}} - \frac{\boldsymbol{x}_{\mathrm{c}}M_{\mathrm{c}} + \boldsymbol{x}_{\mathrm{s}}M_{\mathrm{s}}}{M_{\mathrm{c}} + M_{\mathrm{s}}}\right) \times \frac{\mathrm{d}\boldsymbol{v}_{\mathrm{c}}}{\mathrm{d}t} + M_{\mathrm{s}}\left(\boldsymbol{x}_{\mathrm{s}} - \frac{\boldsymbol{x}_{\mathrm{c}}M_{\mathrm{c}} + \boldsymbol{x}_{\mathrm{s}}M_{\mathrm{s}}}{M_{\mathrm{c}} + M_{\mathrm{s}}}\right) \times \frac{\mathrm{d}\boldsymbol{v}_{\mathrm{s}}}{\mathrm{d}t} \\
&= \frac{\mathrm{d}\boldsymbol{L}_{\mathrm{spin,c}}}{\mathrm{d}t} + \frac{\mathrm{d}\boldsymbol{L}_{\mathrm{spin,s}}}{\mathrm{d}t} + M_{\mathrm{c}}\frac{\boldsymbol{x}_{\mathrm{c}}M_{\mathrm{s}} - \boldsymbol{x}_{\mathrm{s}}M_{\mathrm{s}}}{M_{\mathrm{c}} + M_{\mathrm{s}}} \times \frac{\mathrm{d}\boldsymbol{v}_{\mathrm{c}}}{\mathrm{d}t} + M_{\mathrm{s}}\frac{\boldsymbol{x}_{\mathrm{s}}M_{\mathrm{c}} - \boldsymbol{x}_{\mathrm{c}}M_{\mathrm{c}}}{M_{\mathrm{c}} + M_{\mathrm{s}}} \times \frac{\mathrm{d}\boldsymbol{v}_{\mathrm{s}}}{\mathrm{d}t} \\
&= \frac{\mathrm{d}\boldsymbol{L}_{\mathrm{spin,c}}}{\mathrm{d}t} + \frac{\mathrm{d}\boldsymbol{L}_{\mathrm{spin,s}}}{\mathrm{d}t} - \beta\boldsymbol{r}_{\mathrm{cs}} \times \frac{\mathrm{d}\boldsymbol{v}_{\mathrm{c}}}{\mathrm{d}t} + \beta\boldsymbol{r}_{\mathrm{cs}} \times \frac{\mathrm{d}\boldsymbol{v}_{\mathrm{s}}}{\mathrm{d}t} \\
&= \frac{\mathrm{d}\boldsymbol{L}_{\mathrm{spin,c}}}{\mathrm{d}t} + \frac{\mathrm{d}\boldsymbol{L}_{\mathrm{spin,s}}}{\mathrm{d}t} + \beta\boldsymbol{r}_{\mathrm{cs}} \times \frac{\mathrm{d}\boldsymbol{v}_{\mathrm{cs}}}{\mathrm{d}t} = \frac{\mathrm{d}\boldsymbol{L}_{\mathrm{spin,c}}}{\mathrm{d}t} + \frac{\mathrm{d}\boldsymbol{L}_{\mathrm{spin,s}}}{\mathrm{d}t} + \boldsymbol{r}_{\mathrm{cs}} \times \boldsymbol{F}_{\mathrm{s}} = \boldsymbol{0}\,.
\end{aligned} \tag{25}$$

Here the notation $\boldsymbol{r}_{\mathrm{cs}}$ means the position vector from body c to s, $\beta = \frac{M_{\mathrm{c}}M_{\mathrm{s}}}{M_{\mathrm{c}}+M_{\mathrm{s}}}$ the reduced mass and the last equality follows from the second law of Newton. $\boldsymbol{F}_{\mathrm{s}}$ denotes thus the force on body s. When regarding the extended body of the central body and the point mass of the satellite body, as well as only the force of the first on the second, the spin momentum of the satellite body does not change. It is even not able to exist as it is regarded as a point mass. The resulting equation for the total angular momentum in turn becomes

$$\frac{\mathrm{d}\boldsymbol{L}_{\mathrm{tot}}}{\mathrm{d}t} = \frac{\mathrm{d}\boldsymbol{L}_{\mathrm{spin,c}}}{\mathrm{d}t} + \boldsymbol{r}_{\mathrm{cs}} \times \boldsymbol{F}_{\mathrm{s}} = \boldsymbol{0}\,, \tag{26}$$

giving an equation for the spin angular momentum change of the planet in the aforementioned form:

$$\frac{\mathrm{d}\boldsymbol{L}_{\mathrm{spin,c}}}{\mathrm{d}t} = -\boldsymbol{r}_{\mathrm{cs}} \times \boldsymbol{F}_{\mathrm{s}}\,. \tag{27}$$

A.4. The tidal potential linearized

Starting from the tidal potential generated by a body at time $t - \Delta t$ and position $\boldsymbol{r}_\mathrm{s}(t - \Delta t)$, it can be assumed that (Mignard 1979)

$$V_\mathrm{T}(\boldsymbol{r}) = \sum_{l=2}^{\infty} \left(\frac{R_\mathrm{E}}{|\boldsymbol{r}|}\right)^{l+1} k_l W_l(\boldsymbol{R}, \boldsymbol{r}_\mathrm{s}(t - \Delta t)) \,, \tag{28}$$

with $\boldsymbol{r}$ the position of the calculated potential, R_E the equatorial radius of the perturbed body, k_l the static Love number and $W_l(\boldsymbol{R}, \boldsymbol{r}_\mathrm{s}(t - \Delta t))$ the perturbing potential at the surface point $\boldsymbol{R}$ below the position $\boldsymbol{r}$ caused by the perturbing body at position $\boldsymbol{r}_\mathrm{s}(t - \Delta t)$. From now on for clarity the tidal potential will also be expressed with a second variable denoting the position of the perturbing body, which means in this case that $V_\mathrm{T}(\boldsymbol{r}) = V_\mathrm{T}(\boldsymbol{r}, \boldsymbol{r}_\mathrm{s}(t - \Delta t))$. The time lag Δt can usually be regarded to be small (Mignard 1980). This means that the position can be linearized with

$$\boldsymbol{r}_\mathrm{s}(t - \Delta t) = \boldsymbol{r}_\mathrm{s}(t) - \boldsymbol{v}_\mathrm{s}(t)\Delta t + \boldsymbol{\omega}_\mathrm{c}\Delta t \times \boldsymbol{r}_\mathrm{s}(t) \,, \tag{29}$$

where the $\boldsymbol{\omega}_\mathrm{c}$ denotes the angular velocity of the perturbed body. To simplify the tidal potential at Equation 28, also this potential is linearized in Equation 30 as

$$\begin{aligned} V_\mathrm{T}(\boldsymbol{r}, \boldsymbol{r}_\mathrm{s}(t-\Delta t)) &= V_\mathrm{T}(\boldsymbol{r}, \boldsymbol{r}_\mathrm{s}(t)) + \boldsymbol{\nabla}_{\boldsymbol{r}_\mathrm{s}} V_\mathrm{T}(\boldsymbol{r}, \boldsymbol{r}_\mathrm{s}(t)) \cdot (\boldsymbol{r}_\mathrm{s}(t - \Delta t) - \boldsymbol{r}_\mathrm{s}(t)) \\ &= \sum_{l=2}^{\infty} \left(\frac{R_\mathrm{E}}{|\boldsymbol{r}|}\right)^{l+1} k_l W_l(\boldsymbol{R}, \boldsymbol{r}_\mathrm{s}(t)) + \boldsymbol{\nabla}_{\boldsymbol{r}_\mathrm{s}} \left[\sum_{l=2}^{\infty} \left(\frac{R_\mathrm{E}}{|\boldsymbol{r}|}\right)^{l+1} k_l W_l(\boldsymbol{R}, \boldsymbol{r}_\mathrm{s}(t))\right] (\boldsymbol{\omega}_\mathrm{c} \times \boldsymbol{r}_\mathrm{s}(t) - \boldsymbol{v}_\mathrm{s})\Delta t \,. \end{aligned} \tag{30}$$

With the gradient worked out in Equation 31

$$\begin{aligned} \boldsymbol{\nabla}_{\boldsymbol{r}_\mathrm{s}} V_\mathrm{T}(\boldsymbol{r}, \boldsymbol{r}_\mathrm{s}(t)) &= \boldsymbol{\nabla}_{\boldsymbol{r}_\mathrm{s}} \left[\sum_{l=2}^{\infty} \left(\frac{R_\mathrm{E}}{|\boldsymbol{r}|}\right)^{l+1} k_l W_l(\boldsymbol{R}, \boldsymbol{r}_\mathrm{s}(t))\right] = -GM_\mathrm{s} \boldsymbol{\nabla}_{\boldsymbol{r}_\mathrm{s}} \left[\sum_{l=2}^{\infty} \frac{k_l (R_\mathrm{E})^{2l+1}}{|\boldsymbol{r}|^{l+1} |\boldsymbol{r}_\mathrm{s}(t)|^{l+1}} P_l\left(\frac{\boldsymbol{r} \cdot \boldsymbol{r}_\mathrm{s}(t)}{|\boldsymbol{r}||\boldsymbol{r}_\mathrm{s}(t)|}\right)\right] \\ &= -GM_\mathrm{s} \sum_{l=2}^{\infty} \frac{k_l (R_\mathrm{E})^{2l+1}}{|\boldsymbol{r}|^{l+1} |\boldsymbol{r}_\mathrm{s}|^{l+1}} \left[-\frac{(l+1)\boldsymbol{r}_\mathrm{s}}{|\boldsymbol{r}_\mathrm{s}|^2} P_l(x) + \left.\frac{\mathrm{d}P_l}{\mathrm{d}x}\right|^{x} \cdot \left(\frac{\boldsymbol{r}}{|\boldsymbol{r}||\boldsymbol{r}_\mathrm{s}|} - \frac{(\boldsymbol{r} \cdot \boldsymbol{r}_\mathrm{s})\boldsymbol{r}_\mathrm{s}}{|\boldsymbol{r}||\boldsymbol{r}_\mathrm{s}|^3}\right)\right] , \end{aligned} \tag{31}$$

the tidal potential becomes

$$\begin{aligned} V_\mathrm{T}(\boldsymbol{r}, \boldsymbol{r}_\mathrm{s}(t-\Delta t)) = V_\mathrm{T}(\boldsymbol{r}, \boldsymbol{r}_\mathrm{s}(t)) - GM_\mathrm{s} \sum_{l=2}^{\infty} \frac{k_l (R_\mathrm{E})^{2l+1}}{|\boldsymbol{r}|^{l+2} |\boldsymbol{r}_\mathrm{s}|^{l+1}} \Delta t \\ \cdot \left[\frac{(l+1)(\boldsymbol{r}_\mathrm{s} \cdot \boldsymbol{v}_\mathrm{s})}{|\boldsymbol{r}_\mathrm{s}|^2} |\boldsymbol{r}| P_l(x) + \left.\frac{\mathrm{d}P_l}{\mathrm{d}x}\right|^{x} \cdot \left(\frac{\boldsymbol{r} \cdot (\boldsymbol{\omega}_\mathrm{c} \times \boldsymbol{r}_\mathrm{s})}{|\boldsymbol{r}_\mathrm{s}|} - \frac{\boldsymbol{r} \cdot \boldsymbol{v}_\mathrm{s}}{|\boldsymbol{r}_\mathrm{s}|} + \frac{(\boldsymbol{r} \cdot \boldsymbol{r}_\mathrm{s})(\boldsymbol{r}_\mathrm{s} \cdot \boldsymbol{v}_\mathrm{s})}{|\boldsymbol{r}_\mathrm{s}|^3}\right)\right] , \end{aligned} \tag{32}$$

where for notation simplicity the position $\boldsymbol{r}_\mathrm{s}(t) = \boldsymbol{r}_\mathrm{s}$ and $x = \left(\frac{\boldsymbol{r} \cdot \boldsymbol{r}_\mathrm{s}}{|\boldsymbol{r}||\boldsymbol{r}_\mathrm{s}|}\right)$.

To find the force and consequently the torque, the gradient with respect to $\boldsymbol{r}$ has to be taken of this potential. This leads to

$$\begin{aligned} \boldsymbol{\nabla}_{\boldsymbol{r}} V_\mathrm{T}(\boldsymbol{r}, \boldsymbol{r}_\mathrm{s}(t-\Delta t)) = \boldsymbol{\nabla}_{\boldsymbol{r}} V_\mathrm{T}(\boldsymbol{r}, \boldsymbol{r}_\mathrm{s}(t)) - GM_\mathrm{s} \sum_{l=2}^{\infty} \Bigg\{ &- \frac{(l+2) k_l (R_\mathrm{E})^{2l+1} \boldsymbol{r}}{|\boldsymbol{r}|^{l+4} |\boldsymbol{r}_\mathrm{s}|^{l+1}} \Delta t \cdot \left[\frac{(l+1)(\boldsymbol{r}_\mathrm{s} \cdot \boldsymbol{v}_\mathrm{s})}{|\boldsymbol{r}_\mathrm{s}|^2} |\boldsymbol{r}| P_l(x) \right. \\ &\left. + \left.\frac{\mathrm{d}P_l}{\mathrm{d}x}\right|^{x} \cdot \left(\frac{\boldsymbol{r} \cdot (\boldsymbol{\omega}_\mathrm{c} \times \boldsymbol{r}_\mathrm{s})}{|\boldsymbol{r}_\mathrm{s}|} - \frac{\boldsymbol{r} \cdot \boldsymbol{v}_\mathrm{s}}{|\boldsymbol{r}_\mathrm{s}|} + \frac{(\boldsymbol{r} \cdot \boldsymbol{r}_\mathrm{s})(\boldsymbol{r}_\mathrm{s} \cdot \boldsymbol{v}_\mathrm{s})}{|\boldsymbol{r}_\mathrm{s}|^3}\right)\right] + \frac{k_l (R_\mathrm{E})^{2l+1}}{|\boldsymbol{r}|^{l+2} |\boldsymbol{r}_\mathrm{s}|^{l+1}} \Delta t \\ &\cdot \left[\frac{(l+1)(\boldsymbol{r}_\mathrm{s} \cdot \boldsymbol{v}_\mathrm{s})\boldsymbol{r}}{|\boldsymbol{r}||\boldsymbol{r}_\mathrm{s}|^2} P_l(x) + \frac{(l+1)(\boldsymbol{r}_\mathrm{s} \cdot \boldsymbol{v}_\mathrm{s})}{|\boldsymbol{r}_\mathrm{s}|^2} |\boldsymbol{r}| \left.\frac{\mathrm{d}P_l}{\mathrm{d}x}\right|^{x} \cdot \left(\frac{\boldsymbol{r}_\mathrm{s}}{|\boldsymbol{r}||\boldsymbol{r}_\mathrm{s}|} - \frac{(\boldsymbol{r} \cdot \boldsymbol{r}_\mathrm{s})\boldsymbol{r}}{|\boldsymbol{r}|^3 |\boldsymbol{r}_\mathrm{s}|}\right) \right. \\ &+ \left.\frac{\mathrm{d}^2 P_l}{\mathrm{d}x^2}\right|^{x} \cdot \left(\frac{\boldsymbol{r}_\mathrm{s}}{|\boldsymbol{r}||\boldsymbol{r}_\mathrm{s}|} - \frac{(\boldsymbol{r} \cdot \boldsymbol{r}_\mathrm{s})\boldsymbol{r}}{|\boldsymbol{r}|^3 |\boldsymbol{r}_\mathrm{s}|}\right) \cdot \left(\frac{\boldsymbol{r} \cdot (\boldsymbol{\omega}_\mathrm{c} \times \boldsymbol{r}_\mathrm{s})}{|\boldsymbol{r}_\mathrm{s}|} - \frac{\boldsymbol{r} \cdot \boldsymbol{v}_\mathrm{s}}{|\boldsymbol{r}_\mathrm{s}|} + \frac{(\boldsymbol{r} \cdot \boldsymbol{r}_\mathrm{s})(\boldsymbol{r}_\mathrm{s} \cdot \boldsymbol{v}_\mathrm{s})}{|\boldsymbol{r}_\mathrm{s}|^3}\right) \\ &+ \left.\frac{\mathrm{d}P_l}{\mathrm{d}x}\right|^{x} \cdot \left(\frac{\boldsymbol{\omega}_\mathrm{c} \times \boldsymbol{r}_\mathrm{s}}{|\boldsymbol{r}_\mathrm{s}|} - \frac{\boldsymbol{v}_\mathrm{s}}{|\boldsymbol{r}_\mathrm{s}|} + \frac{\boldsymbol{r}_\mathrm{s}(\boldsymbol{r}_\mathrm{s} \cdot \boldsymbol{v}_\mathrm{s})}{|\boldsymbol{r}_\mathrm{s}|^3}\right)\Bigg]\Bigg\} . \end{aligned} \tag{33}$$

By noting that the force will be evaluated at $\boldsymbol{r} = \boldsymbol{r}_\mathrm{s}$, consequently making $x = \left(\frac{\boldsymbol{r}\cdot\boldsymbol{r}_\mathrm{s}}{|\boldsymbol{r}||\boldsymbol{r}_\mathrm{s}|}\right) = 1$ and stating that $P_l(1) = 1$ and $\left.\frac{\mathrm{d}P_l}{\mathrm{d}x}\right|^1 = \frac{l(l+1)}{2}$ the force results into

$$
\begin{aligned}
\boldsymbol{F}_\mathrm{T} =& -M_\mathrm{s}\nabla_{\boldsymbol{r}} V_\mathrm{T}(\boldsymbol{r}, \boldsymbol{r}_\mathrm{s}(t-\Delta t)) \\
=& G(M_\mathrm{s})^2 \sum_{l=2}^{\infty} \frac{k_l (R_\mathrm{E})^{2l+1}}{|\boldsymbol{r}|^{2l+4}} \cdot \left(-(l+1)\boldsymbol{r} + \frac{l(l+1)}{2}(\boldsymbol{r}-\boldsymbol{r})\right) \\
&+ G(M_\mathrm{s})^2 \sum_{l=2}^{\infty} \left\{ -\frac{(l+2)k_l (R_\mathrm{E})^{2l+1}\boldsymbol{r}}{|\boldsymbol{r}|^{2l+5}} \Delta t \cdot \left[\frac{(l+1)(\boldsymbol{r}\cdot\boldsymbol{v})}{|\boldsymbol{r}|} + \frac{l(l+1)}{2} \cdot \left(0 - \frac{\boldsymbol{r}\cdot\boldsymbol{v}}{|\boldsymbol{r}|} + \frac{\boldsymbol{r}\cdot\boldsymbol{v}}{|\boldsymbol{r}|}\right)\right] \right. \\
&+ \frac{k_l (R_\mathrm{E})^{2l+1}}{|\boldsymbol{r}|^{2l+4}} \Delta t \cdot \left[\frac{(l+1)(\boldsymbol{r}\cdot\boldsymbol{v})\boldsymbol{r}}{|\boldsymbol{r}|^2} + (l+1)(\boldsymbol{r}\cdot\boldsymbol{v})\frac{l(l+1)}{2} \cdot \left(\frac{\boldsymbol{r}}{|\boldsymbol{r}|^2} - \frac{\boldsymbol{r}}{|\boldsymbol{r}|^2}\right)\right. \\
&\left.\left. + \left.\frac{\mathrm{d}^2 P_l}{\mathrm{d}x^2}\right|^1 \cdot \left(\frac{\boldsymbol{r}}{|\boldsymbol{r}|} - \frac{\boldsymbol{r}}{|\boldsymbol{r}|}\right) \cdot \left(0 - \frac{\boldsymbol{r}\cdot\boldsymbol{v}}{|\boldsymbol{r}|} + \frac{\boldsymbol{r}\cdot\boldsymbol{v}}{|\boldsymbol{r}|}\right) + \frac{l(l+1)}{2} \cdot \left(\boldsymbol{\omega}_\mathrm{c} \times \boldsymbol{r} - \boldsymbol{v} + \frac{\boldsymbol{r}(\boldsymbol{r}\cdot\boldsymbol{v})}{|\boldsymbol{r}|^2}\right)\right]\right\} \\
=& -G(M_\mathrm{s})^2 \sum_{l=2}^{\infty} \frac{k_l (R_\mathrm{E})^{2l+1}}{|\boldsymbol{r}|^{2l+4}} \cdot (l+1)\boldsymbol{r} - G(M_\mathrm{s})^2 \sum_{l=2}^{\infty} \left\{ \frac{(l+2)k_l (R_\mathrm{E})^{2l+1}\boldsymbol{r}}{|\boldsymbol{r}|^{2l+4}} \Delta t \cdot \left[\frac{(l+1)(\boldsymbol{r}\cdot\boldsymbol{v})}{|\boldsymbol{r}|^2}\right]\right. \\
&\left. - \frac{k_l (R_\mathrm{E})^{2l+1}}{|\boldsymbol{r}|^{2l+4}} \Delta t \cdot \left[\frac{(l+1)(\boldsymbol{r}\cdot\boldsymbol{v})\boldsymbol{r}}{|\boldsymbol{r}|^2} + \frac{l(l+1)}{2} \cdot \left(\boldsymbol{\omega}_\mathrm{c} \times \boldsymbol{r} - \boldsymbol{v} + \frac{\boldsymbol{r}(\boldsymbol{r}\cdot\boldsymbol{v})}{|\boldsymbol{r}|^2}\right)\right]\right\} \\
=& -G(M_\mathrm{s})^2 \sum_{l=2}^{\infty} \frac{k_l (R_\mathrm{E})^{2l+1}}{|\boldsymbol{r}|^{2l+4}} (l+1)\left\{\boldsymbol{r} + \Delta t\left[\frac{(l+2)\boldsymbol{r}(\boldsymbol{r}\cdot\boldsymbol{v})}{|\boldsymbol{r}|^2} - \frac{\boldsymbol{r}(\boldsymbol{r}\cdot\boldsymbol{v})}{|\boldsymbol{r}|^2} - \frac{l}{2}\frac{\boldsymbol{r}(\boldsymbol{r}\cdot\boldsymbol{v})}{|\boldsymbol{r}|^2}\right.\right. \\
&\left.\left. - \frac{l}{2}(-\boldsymbol{r}\times\boldsymbol{\omega}_\mathrm{c} - \boldsymbol{v})\right]\right\} \\
=& -G(M_\mathrm{s})^2 \sum_{l=2}^{\infty} \left[(l+1)\frac{k_l (R_\mathrm{E})^{2l+1}}{|\boldsymbol{r}|^{2l+4}} \left(\boldsymbol{r} + \Delta t\left\{\frac{l}{2}(\boldsymbol{r}\times\boldsymbol{\omega}_\mathrm{c} + \boldsymbol{v}) + \frac{l+2}{2}\frac{(\boldsymbol{r}\cdot\boldsymbol{v})\boldsymbol{r}}{|\boldsymbol{r}|^2}\right\}\right)\right],
\end{aligned}
\tag{34}
$$

which is conform the theory (Mignard 1980). Many authors (e.g. Lainey et al. 2007; Lari 2018) use only the second degree potential and force. This results then in

$$
\boldsymbol{F}_\mathrm{T} = -3\frac{G(M_\mathrm{s})^2 k_2 (R_\mathrm{E})^5}{|\boldsymbol{r}|^8}\left[\boldsymbol{r} + \Delta t\left(\boldsymbol{r}\times\boldsymbol{\omega}_\mathrm{c} + \boldsymbol{v} + 2\frac{\boldsymbol{r}(\boldsymbol{r}\cdot\boldsymbol{v})}{|\boldsymbol{r}|^2}\right)\right]. \tag{35}
$$

B. Documentation

Both models used, the coupled and the direct force model, are implemented from ground up using Python. This is a manual to use the code in whatever way is required (if functionality is available). The code is uploaded to a github repository: `https://github.com/icetea3/Thesis`.

B.1. User manual

A single propagation is performed with the *main.py* script. In the script the input needed for the propagation is set, the propagation is performed, the outputs are saved to file, the state data is analysed, and the results are summarised in plots and or on screen output.
To begin with the beginning, the input is set under the DEFINE PROBLEM part. The first things set are the boolean values that define whether a specific input file is used to define all inputs, whether gravity field coefficients should be imported from file, and whether the output generated requires saving to file. The outputfilename should be defined if required under outputfile.

```
# Boolean variable, True when inputs from .sol or .pickle are used
setInputsFromFile = False
# Boolean variable, True when gravity field coefficients should be imported from
# specified file
setGFFromFile = False
# Boolean variable, True when output needs saving
saveOutput = False
# If saveOutput, define filename results
if saveOutput:
    outputfile = 'yourFileName'
```

If setInputsFromFile is set **False**, the inputs should be set manually. The entire input for the propagation is contained in a dictionary structure, where the appropriate name of inputdict is used. Within this dictionary, the first main inputs are the used model, which orientation is used, and whether the rotation vector is propagated or kept constant, respectively set in the keys 'whichmodel', 'whichframe', and 'propagaterotation'. Options and defaults are stated in the comments. The key 'whichmodel' defines the entire model and overwrites in that way the perturbationsdict, where specific perturbations can be specified. Only the 'Custom' model allows the perturbations to be completely defined by perturbationsdict. Later in the script, the perturbationsdict is added to the inputdict under the key 'perturbationsdict'.

```
# Set and define inputs
inputdict = {}
# Define the model used - options are now [default = 'Full', 'Correia2014', 'PointMass',
# 'Custom']
inputdict['whichmodel'] = 'Custom'
# Define frame orientation used - options are now [default = 'Inertial', 'Rotating']
inputdict['whichframe'] = 'Inertial'
# Define boolean value whether rotation vector is propagated or not [default = True,
# False]
inputdict['propagaterotation'] = True

# Define perturbations used in dictionary - options are now {'gravity_central':
# [default = None, 'Correia2014'], 'tides_central': [default = None, 'Lainey2007',
# 'Coupled']}
perturbationsdict = {}
perturbationsdict['gravity_central'] = None
perturbationsdict['tides_central'] = 'Lainey2007'
```

The next part of the *main.py* script deals with the gravity coefficients, whether set via input file, or

directly here in the code. For now only up to second degree and order is available. The coefficients are defined in a 2d NumPy array, where the first two columns denote the degree and order, the last two columns the cosine and sine coefficient, respectively. The function setGeoCoeff() is used to read the input file and set the 2d NumPy array in a dictionary, but only for the specific GMM-3 Mars gravity field (Genova et al. 2016). Compatibility for other data files can be updated in the *GeoCoeffReader.py* script. The geoCoeffCentral contains then the coefficients for the gravity field of the central body.

```
GFfilename = 'yourPathName'
maxdegree = 2
geoCoeffdict = setGeoCoeff(GFfilename, maxdegree)
geoCoeffCentral = geoCoeffdict['CentralBody']
```

After defining the gravity field coefficients, the used constants are set in the dictionary constantsdict. Most constants used are specified in the *Constants.py* script, to keep them in a central location and easily adjustable over all other code.

```
# Define constants used and initial conditions
constantsdict = {}
# Specify constants central and satellite body
constantsdict['M_central'] = m_M.value                    # Mass central body [kg]
constantsdict['M_satellite'] = m_Phobos.value             # Mass satellite [kg]
constantsdict['R_central'] = R_M.value                    # Equatorial radius [m]
constantsdict['Cnorm_central'] = Cnorm_M                  # Moment of inertia factor [-]
constantsdict['k2_central'] = k2_M                        # k2 Love number [-]
constantsdict['Q_central'] = Q_M                       # Dissipation/Quality factor Q [-]
constantsdict['T_satellite'] = 7. * 3600. + 39.2 * 60.  # orbital period [s]
constantsdict['GC_central'] = geoCoeffCentral             # unnormalized coefficients [-]
constantsdict['tau_e_central'] = 2.5 * 86400.             # Maxwell relaxation time [s]
```

Having defined the constants, the initial value is set next. Starting from the Keplerian elements of the satellite body, the Cartesian coordinates are retrieved by using the kep2car() function. The rotation vector is defined in omega0 via the rotation period of the central body and points towards the positive z-axis. The orientation of the central body is then defined in terms of its unit axes, from which the quaternion for the central body can be retrieved via formulation in Fukushima (2008).

```
a_sat = 9376e3  # semi major axis Phobos [m]
e_sat = 0.0151  # Eccentricity [-]
i_sat = 0.0 #1.093 / 180. * np.pi  # inclination [rad]
Raan_sat = 0.001  # RAAN [rad]
argper_sat = 0.001  # argument of perigee [rad]
truano_sat = 0.001  # true anomaly [rad]

# Retrieve initial state in cartesian coordinates
state0 = kep2car(a_sat, e_sat, i_sat, Raan_sat, argper_sat, truano_sat,
                 G.value * (constantsdict['M_central'] + constantsdict['M_satellite']))

# Define initial rotation vector central body
rotperiod_central = 24. * 3600. + 37. * 60. + 22.  # sidereal rotation period [s]
omega0 = np.array([0., 0., 2. * np.pi / rotperiod_central])

# Define initial orientation central body, should be based on initial rotation vector
e_rotA0 = np.array([1., 0., 0.])  # Initial unit vector A axis rotating frame
e_rotB0 = np.array([0., 1., 0.])  # Initial unit vector B axis rotating frame
```

```
e_rotC0 = np.array([0., 0., 1.])  # Initial unit vector C axis rotating frame

# Set initial values for the quaternions, based on initial orientation
q00 = 1. / 2. * np.sqrt(1. + e_rotA0[0] + e_rotB0[1] + e_rotC0[2])
q10 = (e_rotB0[2] - e_rotC0[1]) / (4. * q00)
q20 = (e_rotC0[0] - e_rotA0[2]) / (4. * q00)
q30 = (e_rotA0[1] - e_rotB0[0]) / (4. * q00)
qvec0 = np.array([q00, q10, q20, q30])

# Full initial value: position [m], velocity [m/s], rotation vector [rad/s],
# quaternion [-]
y0 = np.concatenate((state0, omega0, qvec0), axis=0)
```

The values filled in here are mimicking a Mars-Phobos system, but using a zero inclination to get a 2-dimenisional system. The y0 denotes the full initial value for the to be propagated variables. For the coupled system the initial state has be extended with the initial values for the tidal geopotential coefficients ΔJ_2^v, $\Delta C_{2,2}^v$ and $\Delta S_{2,2}^v$. These are set in Delta_nu0.

```
# Only add tidal coefficients to initial value if model for tides is coupled
if perturbationsdict['tides_central'] == 'Coupled':
    Delta_nu0J2 = 0.0
    Delta_nu0C22 = 0.0
    Delta_nu0S22 = 0.0
    Delta_nu0 = np.array([Delta_nu0J2, Delta_nu0C22, Delta_nu0S22])

    # Full initial value: position [m], velocity [m/s], rotation vector [rad/s],
    # quaternion [-], tidal param [-]
    y0 = np.concatenate((state0, omega0, qvec0, Delta_nu0), axis=0)
```

By defining the initial state vector, the integrator settings can be specified. All settings are set in the integratordict, which is as well a dictionary structure. The 'timespan' key denotes the start and end point of the integration in seconds. The 'timeeval' key is for the array of points where a solution is required and returned afterwards. The 'method' is defining the built-in method used by the solver. More on these integrator methods can be found in SciPy documentation[1]. The highest order method available is the 'DOP853', which is an 8th order explicit Runge-Kutta method. The 'iv' is short for initial value and the 'rtol' and 'atol' denote the relative and absolute tolerances the solver uses to determine if the next step in the integration is converged so it can stop iterating. Again more on this in the SciPy documentation[1]. The 'func' specifies the function used to calculate the right hand side of the differential equation. This function is key to the integration as it completely covers the calculation of the forces and other necessary parts to determine the change in the state variables. In this case this is RHSfun, other options are for now not available.

```
# Define integrator settings in dictionary
integratordict = {}
# Set timespan of integration - list of begin and end time [s]
integratordict['timespan'] = [0.0, 120.0 * 86400.]
# Set timepoints where solution is requested, must be inside timespan frame
integratordict['timeeval'] = np.linspace(0.0, 120.0 * 86400., 20000)
# Set initial value problem solver method - options are [default = 'RK45', 'LSODA',
# 'Radau', 'BDF', 'RK23']
integratordict['method'] = 'DOP853'
# Set initial value/state vector
```

[1] http://scipy.github.io/devdocs/integrate.html#module-scipy.integrate

```
integratordict['iv'] = y0
# Set function for right hand side of the differential equation
integratordict['func'] = RHSfun
# Set relative tolerance for integrator step error
integratordict['rtol'] = 2.3e-14
# Set absolute tolerance for integrator step error
integratordict['atol'] = 1.0e-19
```

The three separate dictionaries are by itself subsequently added to the main dictionary inputdict.
If setInputsFromFile is set **True**, a previous run which has been saved to file is used for the input. The dirPath and filename should define the directory and name of the previously run file, whereafter the ResultReader() function imports the results including the inputdict. Only the input is then used for the new run, the solution of the state variables is neglected. Some changes can be made to the input if required.

```
else:
    # Path directory
    dirPath = 'yourPath'
    filename = 'yourFileName'
    if filename.split('.')[-1] == 'pickle':
        soltemp, inputdict = ResultReader(dirPath + filename)

    else:
        timestemp, statestemp, inputdict = ResultReader(dirPath + filename)
```

This concludes the problem definition and the setting of the inputs. Below this END OF PROBLEM DEFINITION nothing has to be set or changed for the specific propagation. The remainder will still be explained for clarity of the overall code.
Having set all input, the propagation can be performed. This is done with a single line and the single function Integrator(). It checks the given input in the integratordict for correctness and then starts the built-in solver solve_ivp() from the SciPy package. It returns a solution class object, with different attributes. More on this again in the documentation for the SciPy package.

```
sol = Integrator(inputdict)
```

If the saveOutput is set **True**, the output needs saving. This is done via the OutputWriter() function. It writes to the previously specified path outputfile with an added date-time stamp if datestampbool is **True**, stores the solution of all state variables at all timesteps and as well the input settings. The outputway defines here the way of storing, where both a binary format (.pickle) and a ASCI text format (.sol) are used to store the same solution. Both extension names are newly defined. The pickle package is for storing and retrieving very convenient as it is able to dump entire objects or structures from the Python environment and subsequently read the binary files again and restoring the dumped objects, with a couple lines of code. It is only a very unsafe way of saving and reading. For example a simple change in Python or package version could cause problems rendering the stored object. Moreover, it is a unsecured way of opening a file, so only entirely known dumpfiles should be read. To be sure data remains accessible, also a more elaborate write to text file is used. These .sol files can simply be accessed by a simple text editor as Notepad.

```
# Write inputs and results to dumpfile (binary) and to text file
OutputWriter(outputfile, sol, inputdict, outputway = 'Sol', datestampbool = True)
OutputWriter(outputfile, sol, inputdict, outputway = 'Pickle', datestampbool = True)
```

The analysis is performed next. This includes the transformation of the propagated Cartesian position and velocity back to a form of osculating elements, the analysis of the behaviour of these elements over time, and the determination of the possible tidal geometric lag angle. The results are displayed in the form of mean derivative values determined in different ways, so the mean change in semi-major axis and eccentricity determined via forward difference, backward difference and by making a linear fit of all results. Different variables and or solution characteristics could be determined in this part of the script, but it is recommended to do this in different files after importing the previous solution.
After the analysis, the solution is shown in multiple plots via the plottingfunc() function, which shows the behaviour of the position, velocity, rotation vector, quaternions, and possible tidal geopotential coefficients and tidal lag.

```
if inputdict['perturbationsdict']['tides_central'] == 'Coupled':
    if perturbationsdict['tides_central'] != None:
        Plottingfunc(sol.t, sol.y[0:6, :], kepsol, sol.y[6:9, :], sol.y[9:13, :], \
            sol.y[13:16, :], np.append([a_diffLit], [e_diffLit], axis=0), \
            np.concatenate(([azimuthalAngleBulge], [azimuthalAngleSat], [angleTidalLag])
                , axis=0))
    else:
        Plottingfunc(sol.t, sol.y[0:6, :], kepsol, sol.y[6:9, :], sol.y[9:13, :],
                    sol.y[13:16, :])

else:
    if perturbationsdict['tides_central'] != None:
        Plottingfunc(sol.t, sol.y[0:6, :], kepsol, sol.y[6:9, :], sol.y[9:13, :], \
                     derSVkeplit = np.append([a_diffLit], [e_diffLit], axis = 0))
    else:
        Plottingfunc(sol.t, sol.y[0:6, :], kepsol, sol.y[6:9, :], sol.y[9:13, :])
```

This concludes the script.

C. Verification

This appendix contains the important verification performed for the different dynamical models. It verifies that the propagations performed are correct and that the code is without major errors. As the model is entirely build from ground up in Python, this verification is necessary to state whether the research is valid. Unittest functionality developed with the model has been used during the research to verify the ongoing results. The current verification is divided into three parts, namely the verification of the translational model, the rotational model, and the tidal model.

C.1. The translational dynamical model

First of all, for verification it is easiest to compare the propagation of the state with already verified other tools and software. In this case, this is done with the TU Delft Astrodynamics toolbox (Tudat)[2]. The same initial state is propagated with only a point mass model with both the newly made software and the existing Tudat toolbox. The differences for the position are displayed below in Figure C.4.

The difference between the propagations is small after 1 day. The relative difference is at least in the

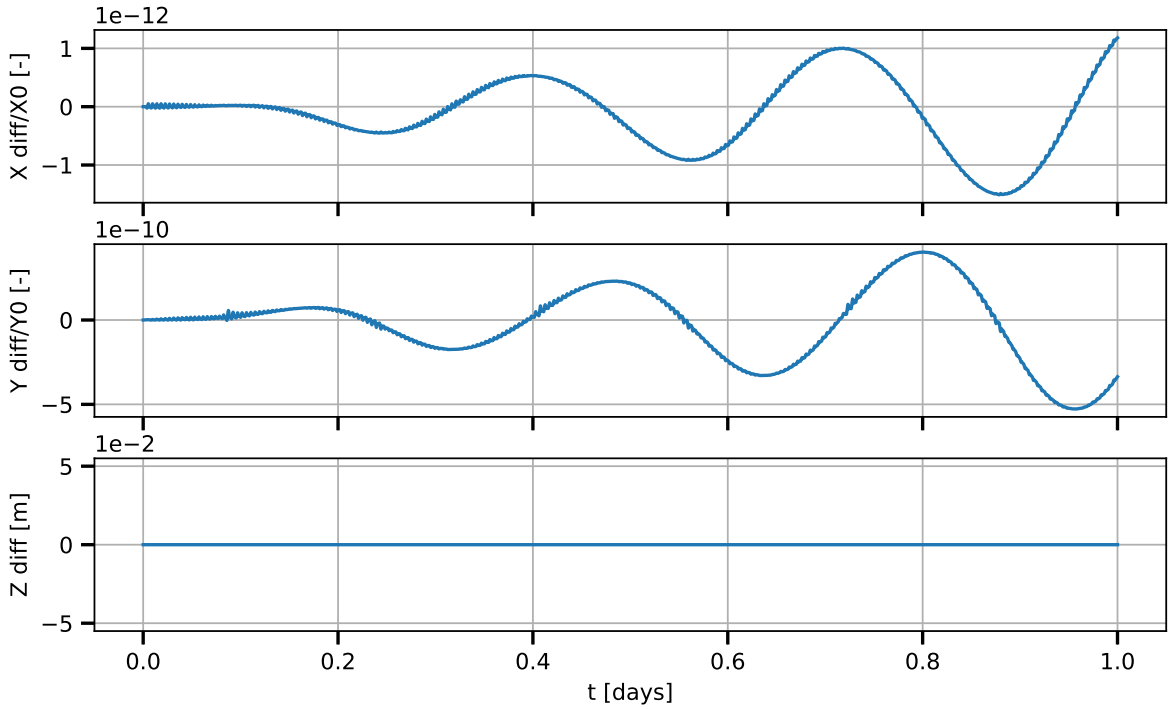

Figure C.4: Normalized position state differences between a point mass propagation performed by the newly developed Python code and the existing Tudat software.

order of 1.0×10^{-10}. Furthermore, the Z-position is for both equal to zero, which is expected as it is a 2D model. The velocity differences are displayed in Figure C.5. The same relative differences are seen and as well the velocity in the z-direction is zero.

As the validation inside the paper is performed by comparing orbital element changes it is necessary to investigated their behaviour too. In Figure C.6 the normalized semi-major axis, the eccentricity and the inclination are shown for the Python and the Tudat propagation. The correct value is added, which is of course the initial value, because the propagations only include point mass bodies. The figure shows the expected behaviour. The semi-major axis as well as the eccentricity for the coupled run are constant in the figure. No slope can be seen for both, and if a linear least-squares fit is performed a derivative of $8.2 \times 10^{-4}\,\mathrm{nm\,s^{-1}}$ and -7.0×10^{-13} /yr are retrieved for the semi-major axis and the eccentricity change respectively. This is in both cases three orders of magnitude smaller than the tidal secular change calculated in the paper. Consequently, the secular changes as seen in the paper are

[2] http://tudat.tudelft.nl/

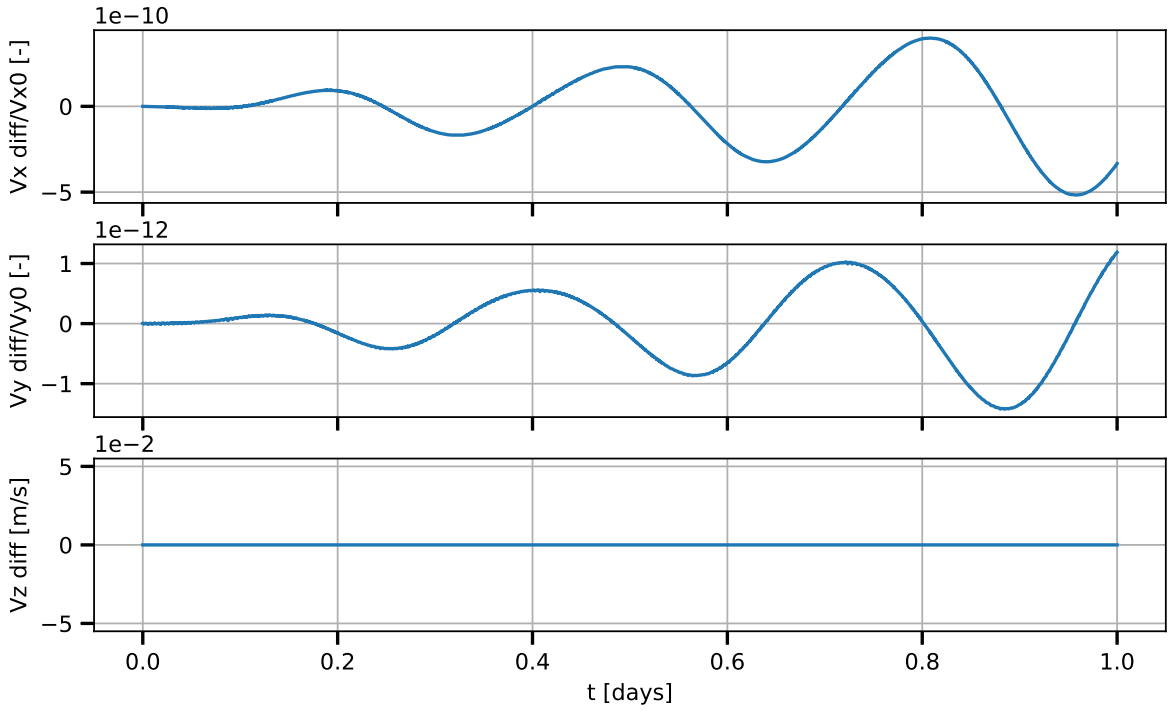

Figure C.5: Normalized velocity state differences between a point mass propagation performed by the newly developed Python code and the existing Tudat software.

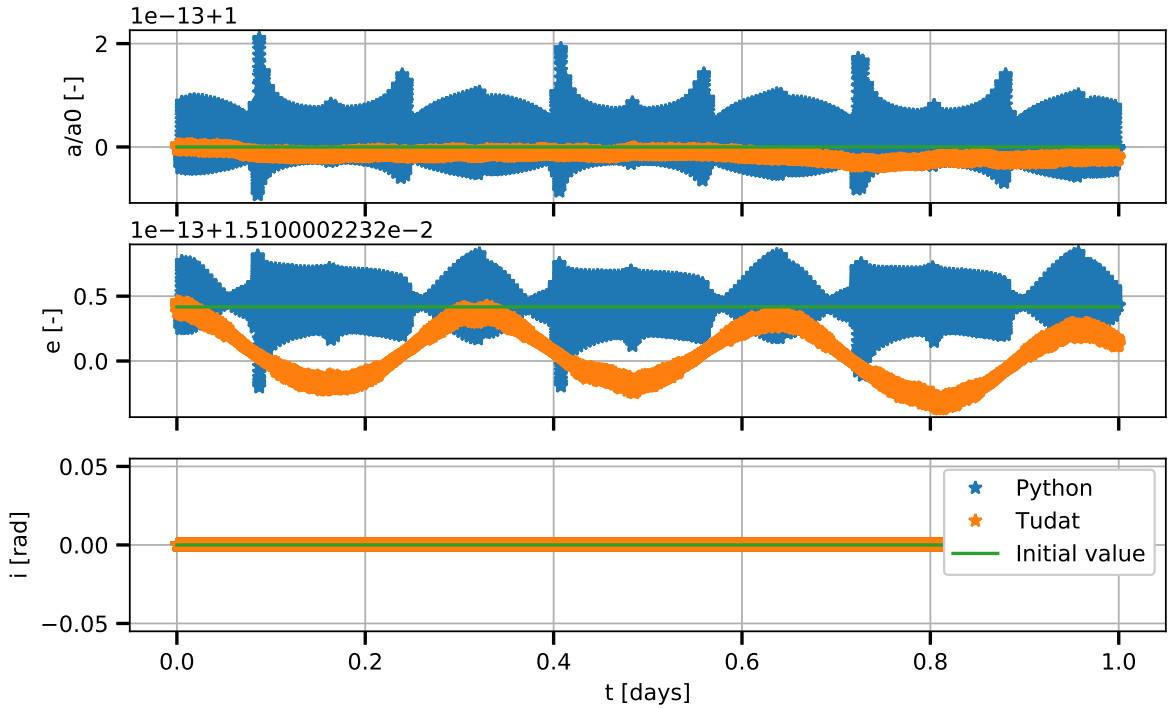

Figure C.6: Normalized orbital elements states of a point mass propagation performed by the newly developed Python code and the existing Tudat software.

not caused by the point mass propagation and similarly not by the integrator, which is now validated. The variations seen in the figure are caused by the polynomial used to retrieve the state at the required epochs. The integrator in the Python code used is as mentioned a 8th order Runge-Kutta method (DOP853[3]) with varying stepsize. Because of the varying stepsize a 7th order polynomial is fitted to retrieve the required epochs. The integrator used in the Tudat verification run is a 4th order Runge-Kutta method with fixed stepsize of 5 s. A last thing to note is that the inclination remains zero as expected as well. It is another reason to state that the problem created is in fact truly 2-dimensional.

Subsequently, the gravity model needs verification. In both the Python code as the Tudat toolbox a propagation is performed while using a second degree gravity field with static parameters for J_2, C_{22}, and S_{22}. The position differences are plotted in Figure C.7. The propagation after 1 day displays the

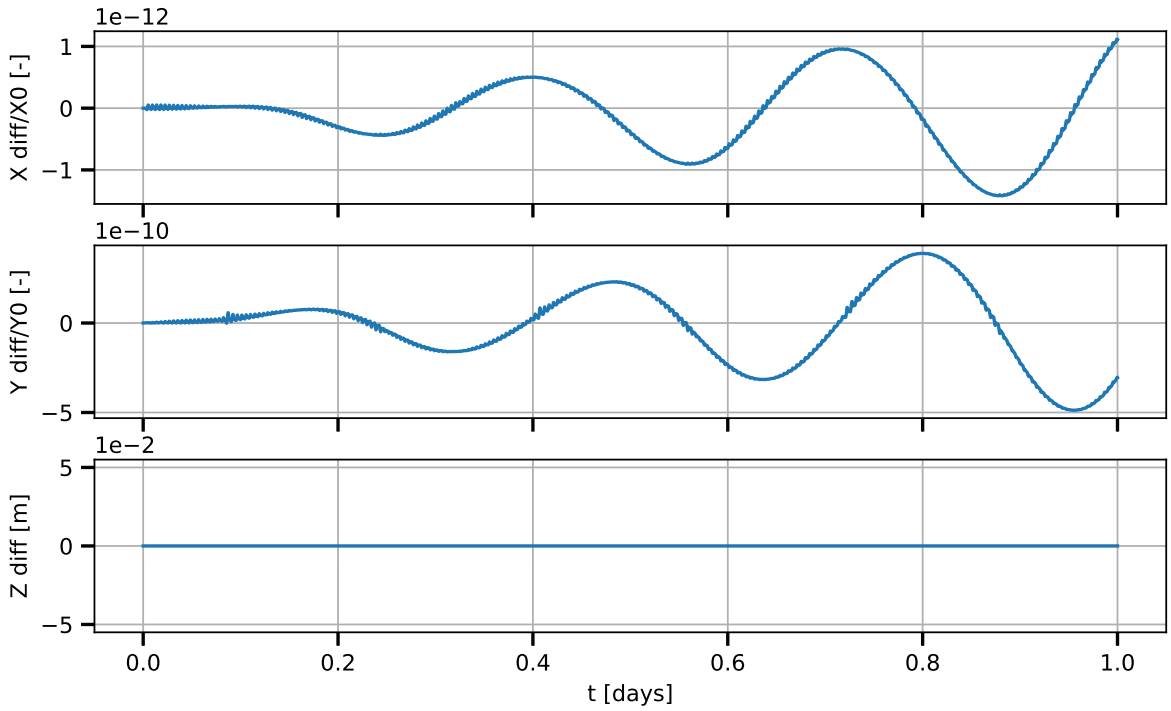

Figure C.7: Normalized position state differences between a propagation performed by the newly developed Python code and the existing Tudat software, both with a second degree gravity field for the central body.

same relative differences in the order of 1.0×10^{-10} as for the point mass run, and the gravity model is verified for the position. The velocity components are shown in Figure C.8. The velocity difference can as well be neglected. Next, the behaviour of the orbital elements is plotted in Figure C.9. This time the relative difference is plotted for the semi-major axis and the difference for the eccentricity. It shows a very minor difference of up to the order of 1.0×10^{-13}, and again the inclination remains zero. This shows that the Python code is correct. The minor error is due to the differences in integrator and its settings.

C.2. The rotational dynamical model

The rotational model is verified by comparing with a propagation performed by Tudat. This time the rotation and orientation are propagated as well as the position and velocity state. A propagation with a second degree gravity field of Phobos and a point mass Mars is performed on both tools, and the angular velocity state vector as well as the quaternion state are compared. To see the influence of the propagation of the rotation on the orbital elements evolution, also the semi-major axis, eccentricity and inclination are compared. The physical libration angle is determined by subtracting a linear fit from the

[3] https://docs.scipy.org/doc/scipy/reference/generated/scipy.integrate.DOP853.html

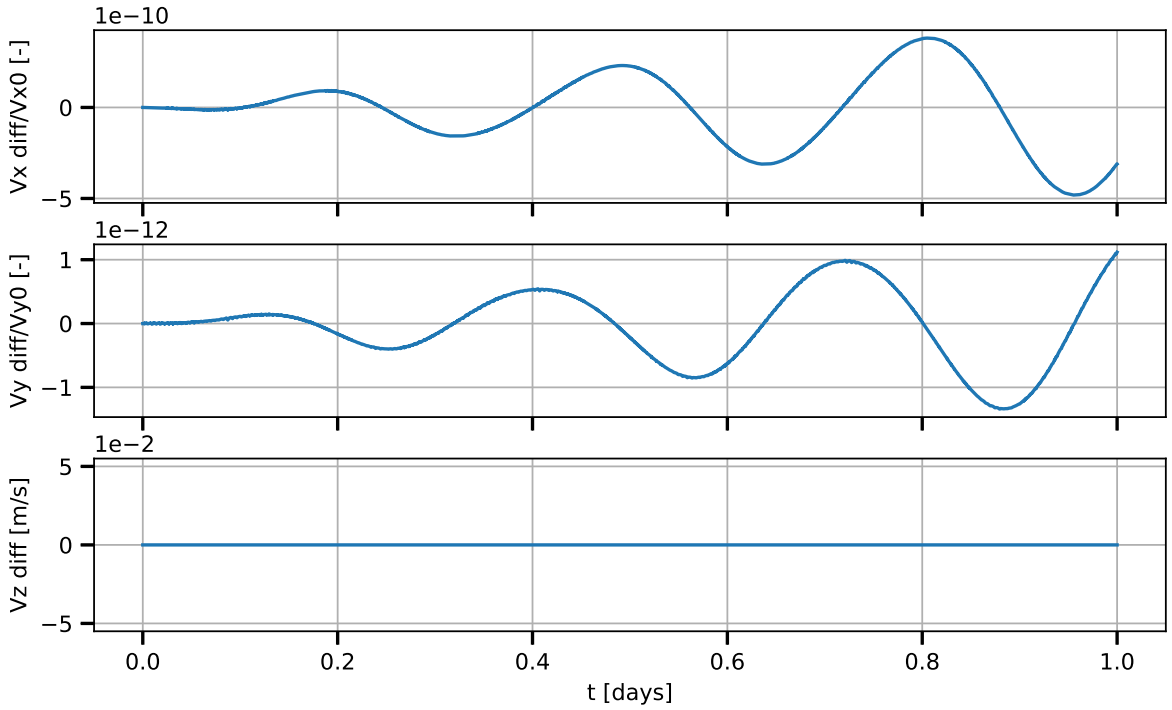

Figure C.8: Normalized velocity state differences between a propagation performed by the newly developed Python code and the existing Tudat software, both with a second degree gravity field for the central body.

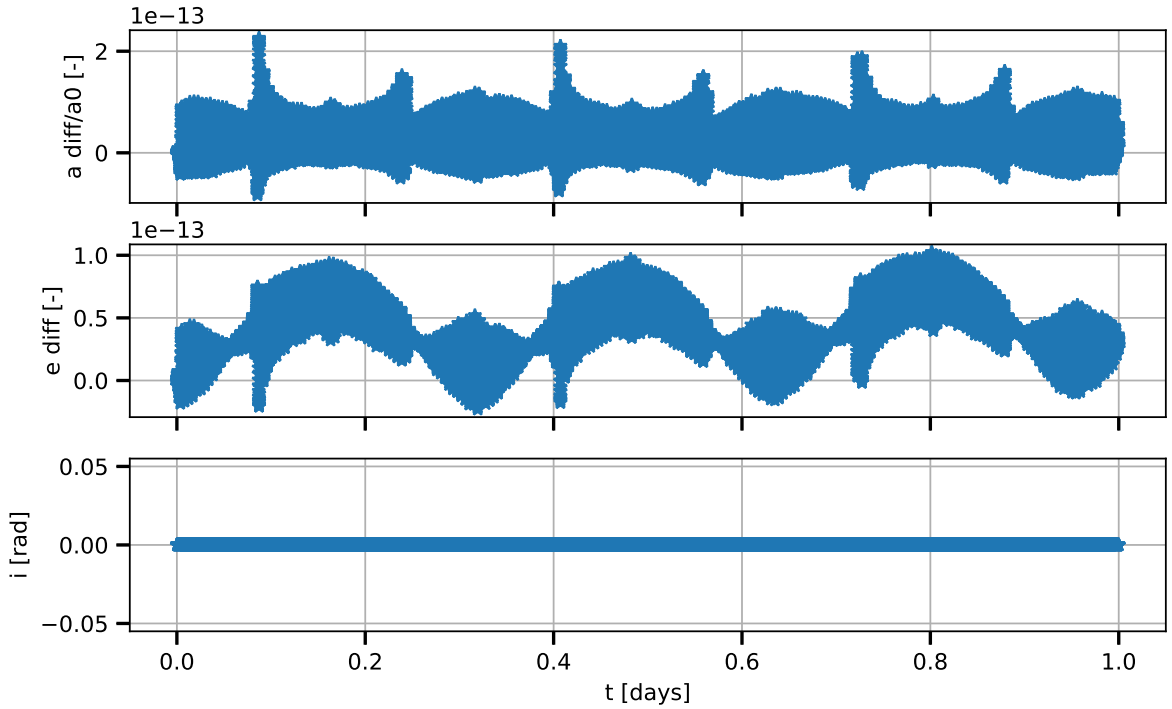

Figure C.9: Normalized orbital elements state differences between a propagation performed by the newly developed Python code and the existing Tudat software, both with a second degree gravity field for the central body.

unwrapped rotation angle. The rotation angle is defined as the angle between the inertial and the fixed rotating frame, and is obtained by retrieving the unit axis of the rotating frame. See the derivation in the paper. First, the angular velocity vector of the secondary body is shown in Figure C.10.
Because a 2D system is regarded, no rotation rate is expected in the x and y direction, as they lie in the

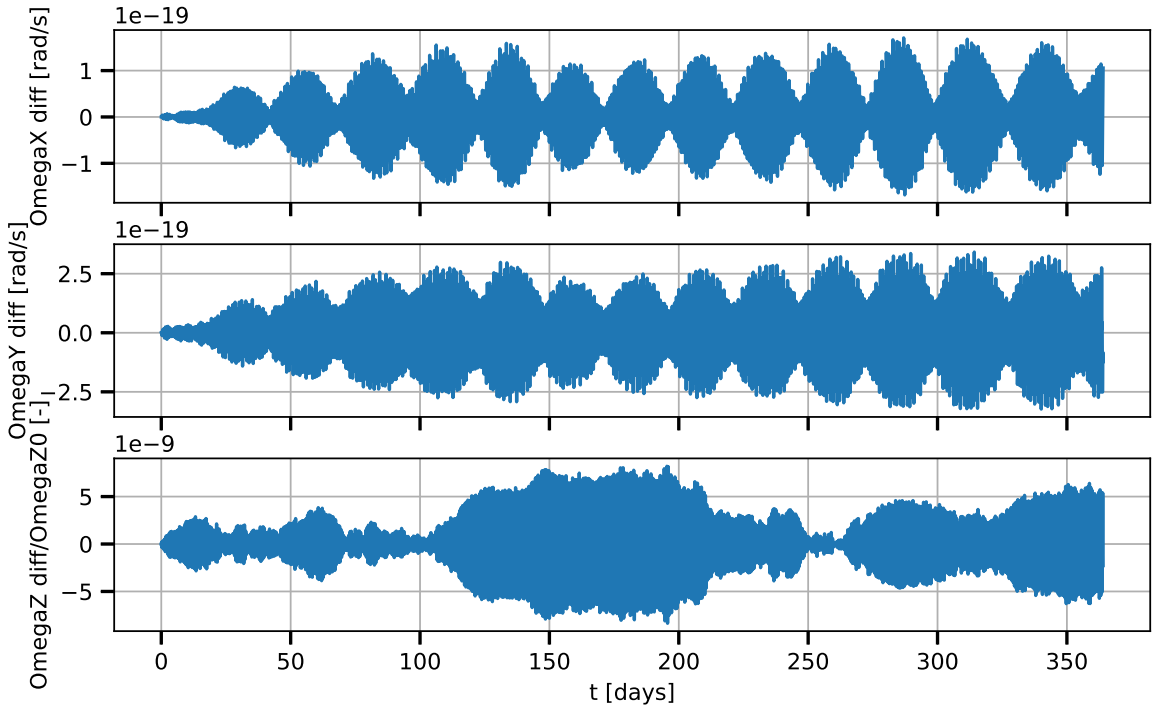

Figure C.10: Differences in the rotation vector state of the secondary body between a propagation performed by the newly developed Python code and the existing Tudat software, both with a second degree gravity field for the secondary.

orbital plane. The difference seen in these directions is completely caused by the Tudat propagation. The rotation rate in the x and y directions remains zero for the Python tool. Furthermore, the difference in the z direction is stable and does not grow above a value of 1.0×10^{-8} in relative difference. It is assumed that this error follows from the difference in integrator and not from any bug in the code.
The next thing to verify is the orientation of the system, for the propagations kept in the quaternion vector. The state differences are displayed in Figure C.11. The 2-dimensional system should lead to a zero second and third quaternion vector entry. The difference seen in the second and third plot is a direct link with the nonzero rotation rate in the x and y direction. The Tudat propagation is not entirely 2-dimensional, while the Python propagation shows the correct zero value. It must be stated that these magnitudes are not causing any differences in results, as they lie close to or below the machine error. The impact on the orbital elements is not substantial, as can be seen in Figure C.12. The relative difference of the semi-major axis remains in the order of 1.0×10^{-12} after a year of propagation, though a minor trend of -5.5×10^{-4} nm s^{-1} can be observed. This trend is at least an order of 1.0×10^{3} smaller than the observed trends in the paper. The eccentricity comparison shows a difference in the order of 1.0×10^{-13} and a small slope of -6.6×10^{-14} /yr, which is as well an order of 1.0×10^{3} smaller than the smallest trend obtained in the paper. The inclination is as expected zero.
Figure C.13 shows the physical libration angle difference divided by the maximum value it reaches in the propagation. The relative difference remains in the order of 1.0×10^{-7}, however a clear trend is seen. This is undoubtedly caused by the nonzero quaternion and rotation vector of the Tudat propagation, this difference does not influence the results in the paper in any way.

C.3. The tidal dynamical model

The larger part of the verification for the tidal part is performed in the paper. That includes the comparison with literature approximations stating the evolution of the orbital elements. What definitely still

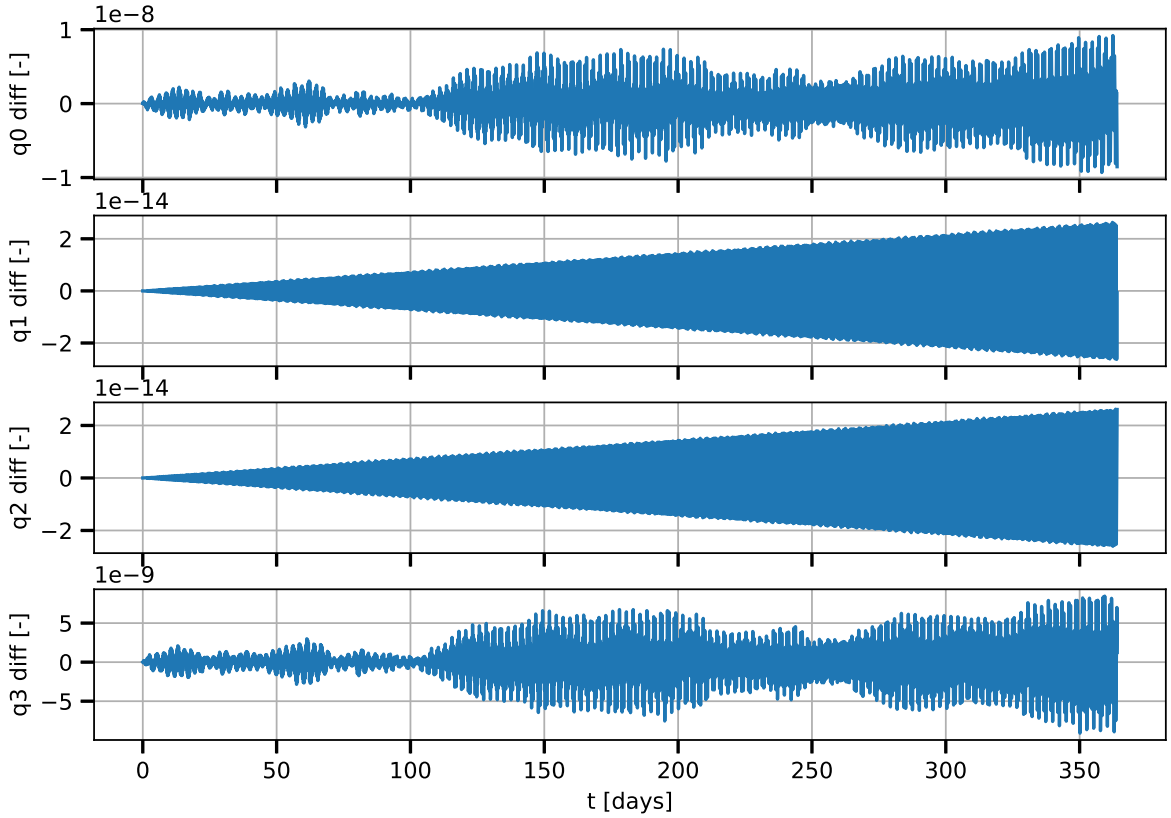

Figure C.11: Differences in the quaternion state of the secondary body between a propagation performed by the newly developed Python code and the existing Tudat software, both with a second degree gravity field for the secondary.

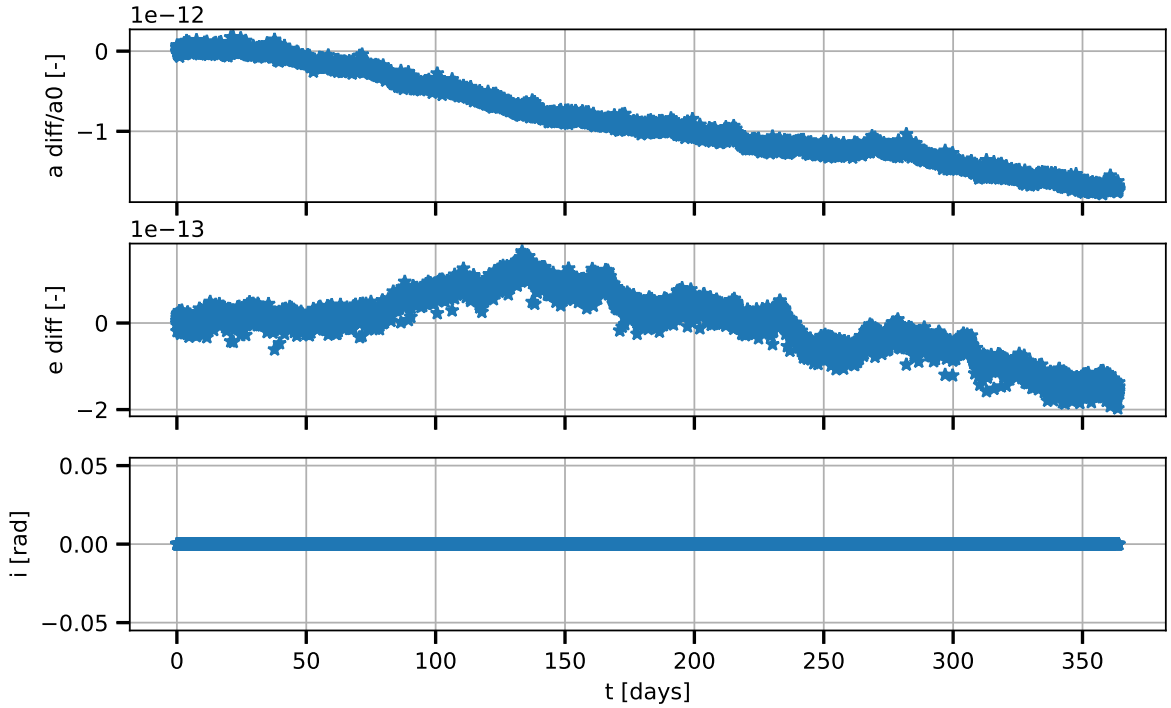

Figure C.12: Normalized orbital elements state differences between a propagation performed by the newly developed Python code and the existing Tudat software, both with a second degree gravity field for the secondary.

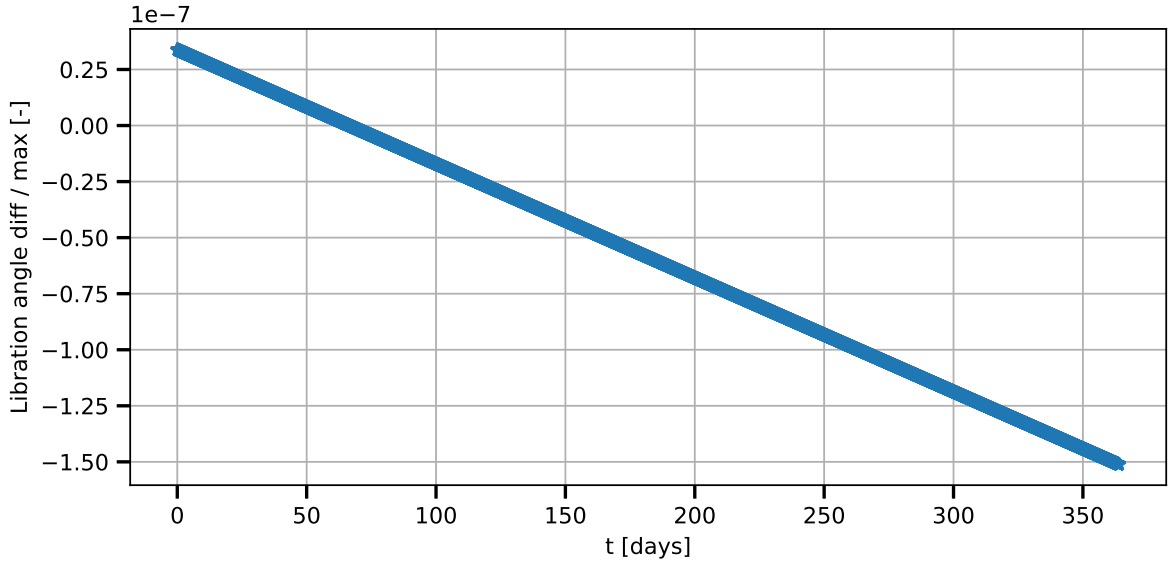

Figure C.13: The difference in the physical longitudinal libration angle of the secondary between a propagation performed by the newly developed Python code and the existing Tudat software, both with a second degree gravity field for the secondary.

can be verified is the behaviour of the direct tidal dissipation model from Lainey et al. (2007). This tidal model is included in Tudat and a run with the same initial state and constants is performed on both software tools. This includes only a point mass system with the addition of the direct tidal force on the primary as calculated by Lainey et al. (2007). The difference in the position state is plotted in Figure C.14. The difference remains small in all directions, and is similar to the differences in the comparison

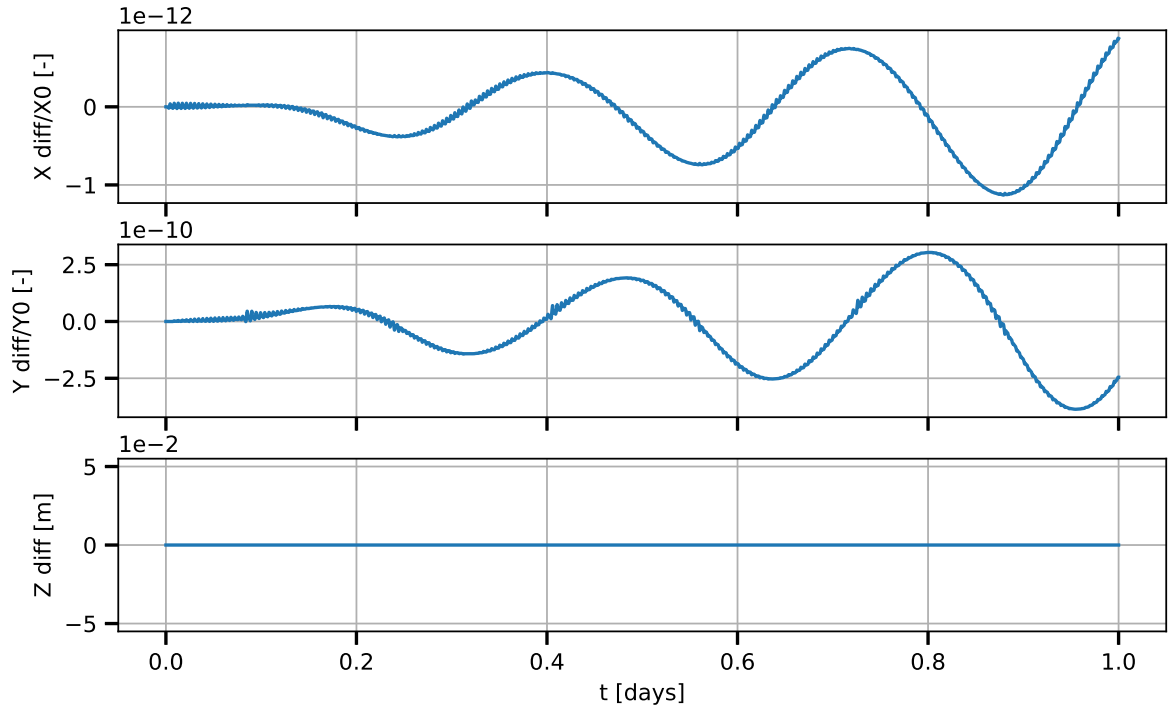

Figure C.14: Normalized position state differences between a propagation performed by the newly developed Python code and the existing Tudat software, both with a direct tidal force on the primary as given in Lainey et al. (2007).

of the gravity field and point mass propagations. The velocity state is displayed in Figure C.15.

As well for the velocity state, differences remain within the order of 1.0×10^{-10} and are verified.

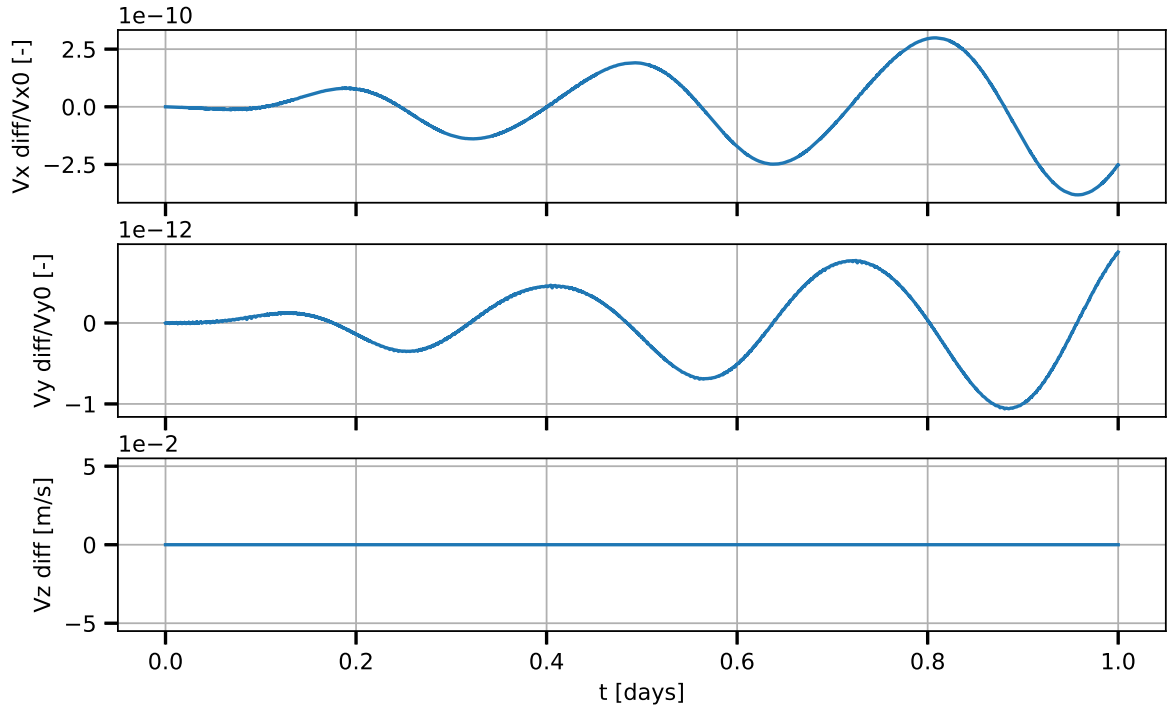

Figure C.15: Normalized velocity state differences between a propagation performed by the newly developed Python code and the existing Tudat software, both with a direct tidal force on the primary as given in Lainey et al. (2007).

The last verification is done by comparing the effect on the evolution of the orbital elements. This is shown in Figure C.16. Although a relatively large evolution is present in both propagations, namely of

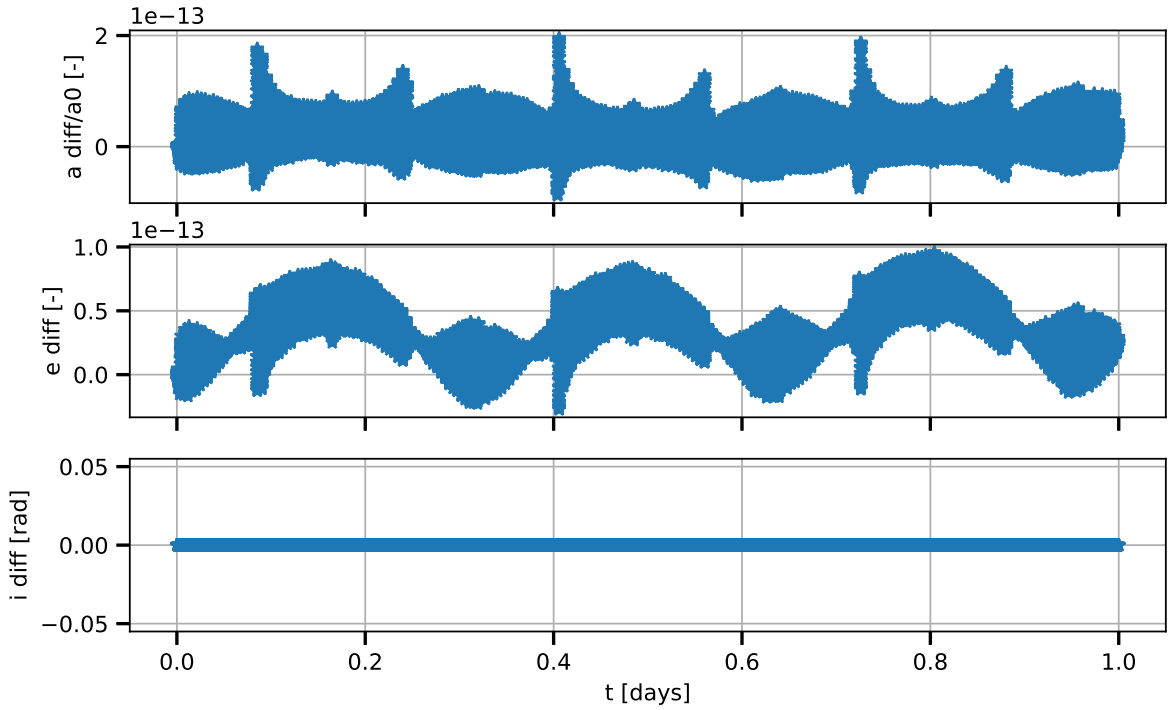

Figure C.16: Normalized orbital elements state differences between a propagation performed by the newly developed Python code and the existing Tudat software, both with a direct tidal force on the primary as given in Lainey et al. (2007).

$-1.23\,\mathrm{nm\,s^{-1}}$ and 3.61×10^{-9} /yr for the semi-major axis and eccentricity respectively, the difference in between the Python and Tudat propagations remains similar to the point mass and gravity field comparisons. The inclination is as expected equal to zero.
This verifies the results achieved by the Python code. All important state and dependent variables are similar to those obtained from a different toolbox. The differences seen do not result in significant other results. This verifies the equations of motion for the translational and rotational dynamics (Equations 37-40 in the paper), as well as the direct tidal force model (Equation 21 in the paper).

Bibliography

Joshua Ashenberg. Proposed method for modeling the gravitational interaction between finite bodies. *Journal of Guidance, Control, and Dynamics*, 28(4):768–774, 2005. ISSN 0731-5090 1533-3884. doi: 10.2514/1.9201.

N. Borderies. Mutual gravitational potential of n solid bodies. *Celestial Mechanics*, 18(3):295–307, 1978. ISSN 0008-8714. doi: 10.1007/Bf01230170.

G. Boue, A. C. M. Correia, and J. Laskar. Complete spin and orbital evolution of close-in bodies using a maxwell viscoelastic rheology. *Celestial Mechanics & Dynamical Astronomy*, 126(1-3):31–60, 2016. ISSN 0923-2958. doi: 10.1007/s10569-016-9708-x.

G. Boué. Tidal evolution of the keplerian elements. *Celestial Mechanics and Dynamical Astronomy*, 131(7), 2019. ISSN 1572-9478 0923-2958.

A. C. M. Correia. Secular evolution of a satellite by tidal effect: Application to triton. *Astrophysical Journal Letters*, 704(1):L1–L4, 2009. doi: 10.1088/0004-637x/704/1/L1.

A. C. M. Correia, G. Boue, J. Laskar, and A. Rodriguez. Deformation and tidal evolution of close-in planets and satellites using a maxwell viscoelastic rheology. *Astronomy & Astrophysics*, 571, 2014. ISSN 1432-0746. doi: ArtnA5010.1051/0004-6361/201424211.

G. H. Darwin. On the Secular Changes in the Elements of the Orbit of a Satellite Revolving about a Tidally Distorted Planet. *Philosophical Transactions of the Royal Society of London Series I*, 171: 713–891, 1880.

George Howard Darwin and James Whitbread Lee Glaisher. Xiii. on the precession of a viscous spheroid, and on the remote history of the earth. *Philosophical Transactions of the Royal Society of London*, 170:447–538, 1879. doi: 10.1098/rstl.1879.0073. URL https://royalsocietypublishing.org/doi/abs/10.1098/rstl.1879.0073.

V. Dehant, R. Park, D. Dirkx, L. Iess, G. Neumann, S. Turyshev, and T. Van Hoolst. Survey of capabilities and applications of accurate clocks: Directions for planetary science. *Space Science Reviews*, 212 (3-4):1433–1451, 2017. ISSN 0038-6308. doi: 10.1007/s11214-017-0424-y.

D. Dirkx, V. Lainey, L. I. Gurvits, and P. N. A. M. Visser. Dynamical modelling of the galilean moons for the juice mission. *Planetary and Space Science*, 134:82–95, 2016. ISSN 0032-0633. doi: 10.1016/j.pss.2016.10.011.

Dominic Dirkx, Erwin Mooij, and Bart Root. Propagation and estimation of the dynamical behaviour of gravitationally interacting rigid bodies. *Astrophysics and Space Science*, 364(2), 2019. ISSN 0004-640X 1572-946X. doi: 10.1007/s10509-019-3521-4.

M. Efroimsky. Bodily tides near spin-orbit resonances. *Celestial Mechanics & Dynamical Astronomy*, 112(3):283–330, 2012. ISSN 0923-2958. doi: 10.1007/s10569-011-9397-4.

M. Efroimsky and J. G. Williams. Tidal torques: a critical review of some techniques. *Celestial Mechanics & Dynamical Astronomy*, 104(3):257–289, 2009. ISSN 0923-2958. doi: 10.1007/s10569-009-9204-7.

Michael Efroimsky. Dissipation in a tidally perturbed body librating in longitude. *Icarus*, 306:328–354, 2018. ISSN 0019-1035. doi: https://doi.org/10.1016/j.icarus.2017.10.020. URL http://www.sciencedirect.com/science/article/pii/S0019103517303901.

Michael Efroimsky and Valeri V. Makarov. Tidal friction and tidal lagging. applicability limitations of a popular formula for the tidal torque. *The Astrophysical Journal*, 764(1), 2013. ISSN 0004-637X 1538-4357. doi: 10.1088/0004-637x/764/1/26.

E. G. Fahnestock and D. J. Scheeres. Simulation of the full two rigid body problem using polyhedral mutual potential and potential derivatives approach. *Celestial Mechanics & Dynamical Astronomy*, 96(3-4):317–339, 2006. ISSN 0923-2958. doi: 10.1007/s10569-006-9045-6.

S. Ferraz-Mello. Tidal synchronization of close-in satellites and exoplanets. a rheophysical approach. *Celestial Mechanics & Dynamical Astronomy*, 116(2):109–140, 2013. ISSN 0923-2958. doi: 10.1007/s10569-013-9482-y.

W. Folkner, James Williams, Dale Boggs, Ryan Park, and P. Kuchynka. The planetary and lunar ephemerides de430 and de431. *Interplanetary Network Progress Report*, 196, 2014.

T. Fukushima. Simple, regular, and efficient numerical integration of rotational motion. *Astronomical Journal*, 135(6):2298–2322, 2008. ISSN 0004-6256. doi: 10.1088/0004-6256/135/6/2298.

Galileo Galilei and Albert Van Helden. *Sidereus nuncius, or, The Sidereal messenger*. University of Chicago Press, Chicago, 1989. ISBN 0226279022, 0226279030. URL http://www.loc.gov/catdir/description/uchi052/88025179.html.

Antonio Genova, Sander Goossens, Frank G. Lemoine, Erwan Mazarico, Gregory A. Neumann, David E. Smith, and Maria T. Zuber. Seasonal and static gravity field of mars from mgs, mars odyssey and mro radio science. *Icarus*, 272:228–245, 2016. ISSN 0019-1035. doi: https://doi.org/10.1016/j.icarus.2016.02.050. URL http://www.sciencedirect.com/science/article/pii/S0019103516001287.

P. Goldreich and S. Soter. Q in solar system. *Icarus*, 5(4):375, 1966. ISSN 0019-1035. doi: 10.1016/0019-1035(66)90051-0.

I. Kant. *Kant's Cosmonogy: as in his Essay on the Retardation of the Rotation of the Earth, and his Natural History and Theory of the Heavens.* 1754.

W. M. Kaula. Tidal dissipation by solid friction and the resulting orbital evolution. *Reviews of Geophysics*, 2(4):661–685, 1964. ISSN 8755-1209. doi: 10.1029/RG002i004p00661.

F. Kikuchi, Q. Liu, H. Hanada, N. Kawano, K. Matsumoto, T. Iwata, S. Goossens, K. Asari, Y. Ishihara, S. Tsuruta, T. Ishikawa, H. Noda, N. Namiki, N. Petrova, Y. Harada, J. Ping, and S. Sasaki. Picosecond accuracy vlbi of the two subsatellites of selene (kaguya) using multifrequency and same beam methods. *Radio Science*, 44(2), 2009. ISSN 0048-6604. doi: 10.1029/2008RS003997. URL https://doi.org/10.1029/2008RS003997.

V. Lainey, L. Duriez, and A. Vienne. New accurate ephemerides for the galilean satellites of jupiter. *Astronomy & Astrophysics*, 420(3):1171–1183, 2004. ISSN 0004-6361 1432-0746. doi: 10.1051/0004-6361:20034565.

V. Lainey, V. Dehant, and M. Pätzold. First numerical ephemerides of the martian moons. *Astronomy & Astrophysics*, 465(3):1075–1084, 2007. ISSN 0004-6361 1432-0746. doi: 10.1051/0004-6361:20065466.

V. Lainey, J. E. Arlot, O. Karatekin, and T. Van Hoolst. Strong tidal dissipation in io and jupiter from astrometric observations. *Nature*, 459(7249):957–959, 2009. ISSN 0028-0836. doi: 10.1038/nature08108.

Valéry Lainey, Luis Gomez Casajus, Jim Fuller, Marco Zannoni, Paolo Tortora, Nicholas Cooper, Carl Murray, Dario Modenini, Ryan S Park, Vincent Robert, et al. Resonance locking in giant planets indicated by the rapid orbital expansion of titan. *Nature Astronomy*, pages 1–6, 2020.

Giacomo Lari. A semi-analytical model of the galilean satellites' dynamics. *Celestial Mechanics and Dynamical Astronomy*, 130(8), 2018. ISSN 0923-2958 1572-9478. doi: 10.1007/s10569-018-9846-4.

J. J. Lissauer. Astronomia nova. *Nature*, 462(7274):725–725, 2009. ISSN 0028-0836. doi: 10.1038/462725a.

G. J. F. Macdonald. Tidal friction. *Reviews of Geophysics*, 2(3):467–541, 1964. ISSN 8755-1209. doi: 10.1029/RG002i003p00467.

A. J. Maciejewski. Reduction, relative equilibria and potential in the two rigid bodies problem. *Celestial Mechanics & Dynamical Astronomy*, 63(1):1–28, 1995. ISSN 0923-2958. doi: 10.1007/Bf00691912.

F. Mignard. Evolution of the lunar orbit revisited .1. *Moon and the Planets*, 20(3):301–315, 1979. ISSN 0165-0807. doi: 10.1007/Bf00907581.

F. Mignard. The evolution of the lunar orbit revisited .2. *Moon and the Planets*, 23(2):185–201, 1980. ISSN 0165-0807. doi: 10.1007/Bf00899817.

Oliver Montenbruck and Eberhard Gill. *Satellite orbits : models, methods, and applications*. Springer, Berlin New York, 2000. ISBN 354067280X. URL http://www.loc.gov/catdir/enhancements/fy0812/00038815-d.html.

Isaac Newton, Andrew Motte, and John Machin. *The mathematical principles of natural philosophy*. Printed for B. Motte, London„ 1729.

J. P. Renaud and W. G. Henning. Increased tidal dissipation using advanced rheological models: Implications for io and tidally active exoplanets. *Astrophysical Journal*, 857(2), 2018. ISSN 0004-637x. doi: 10.3847/1538-4357/aab784.

S. F. Singer. Origin of moon and geophysical consequences. *Geophysical Journal of the Royal Astronomical Society*, 15(1-2):205–, 1968. ISSN 0016-8009.

Jean Souchay, Stéphane Mathis, and Tadashi Tokieda. *Tides in astronomy and astrophysics*. Lecture notes in physices,. Springer, Heidelberg ; New York, 2013. ISBN 9783642329609, 3642329608, 0075-8450.

Slava G. Turyshev, William Farr, William M. Folkner, André R. Girerd, Hamid Hemmati, Thomas W. Murphy, James G. Williams, and John J. Degnan. Advancing tests of relativistic gravity via laser ranging to phobos. *Experimental Astronomy*, 28(2):209–249, 2010. ISSN 1572-9508. doi: 10.1007/s10686-010-9199-9. URL https://doi.org/10.1007/s10686-010-9199-9.

Vishnu Viswanathan, Agnès Fienga, Mickael Gastineau, and Jacques Laskar. Inpop17a planetary ephemerides. 08 2017. doi: 10.13140/RG.2.2.24384.43521.